OFFICE OF SURFACE MINING RECLAMATION AND ENFORCEMENT (OSM)
APPLIED SCIENCE PROGRAM COOPERATIVE AGREEMENT S11AC20018 AS

Improved sulfate-reducing bioreactors for the remediation of high total dissolved solids drainage associated with coal mining and processing in the U.S.

Final Report

By Dr. Liliana Lefticariu*

3/26/2015

*Principal Investigator – Dr. Liliana Lefticariu, address: Department of Geology, Southern Illinois University, 1259 Lincoln Dr, Carbondale, IL, 62901; telephone: 618-453-7373; fax: 618-453-7393: e-mail: lefticar@siu.edu

TABLE OF CONTENTS

Improved sulfate-reducing bioreactors for the remediation of high total dissolved solids drainage associated with coal mining and processing in the U.S.

Abstract

This project purposes to investigate the geochemistry of an existing sulfate-reducing bioreactor, the Tab Simco Project, constructed near Carbondale, Illinois. The passive treatment system has been treating coal-generated acid mine drainage (AMD) with high total dissolved solids (total dissolved solids > 4,000 mg/L). The AMD occurs at a considerable number of abandoned coal mine sites in both the Illinois basin and Appalachia and is characterized by low-pH and high total dissolves solids. In addition, these particularly problematic discharges are characterized by elevated concentrations of sulfate, iron, aluminum, manganese, and other pollutants associated with coal mining. Development of reliable passive and/or semi-passive treatment technologies will allow remediation of these toxic discharges and reduce their aquatic impacts. The proposed research has evaluated the potential limiting factors to bioreactor treatment activity through a series of batch reactor incubation experiments in which the effect of simple versus complex carbon sources on AMD was assessed using *in situ* pilot-scale bioreactors. New system evaluation methods, including applications of isotope geochemistry, organic geochemistry, and microbiology, were employed to assess, monitor, and improve the efficiency of the bioreactor treatment processes.

Five 210-liter (55-gal) experimental microcosms containing various proportions of herbaceous and ligneous organic substrates and one control bioreactor containing only limestone were constructed at the Tab-Simco abandoned mine land (AML) site in Southern Illinois, USA and monitored over a period of 400 days in order to evaluate the physical, geochemical, and microbiological parameters which control the anaerobic sulfate reduction bacteria (ASRB) efficiency in removing acid mine drainage (AMD) contaminants. All bioreactors established sulfate-reducing bacteria (SRB) populations that contributed to enhanced removal of SO_4, Fe, and trace metals (i.e. Cu, Cd, Zn, Ni) by forming Fe-oxyhydroxide precipitates, adsorption, co-precipitation (e.g. Zn/Ni-Ferrites), and bio-induced sulfide mineralization. The strongest removal of dissolved constituents SO_4, Fe, Al and Mn was obtained in the predominantly herbaceous bioreactors. The extrapolation of the results to the full-scale Tab-Simco bioreactor indicated that, over the course of one year, the predominantly herbaceous bioreactors would remove ~75,600 kg (83.3 s. tons) SO_4, 21,800 kg (24 s. tons) Fe, 8,000 kg (8.8 s. tons) Al, and 77 kg (170 lb) Mn, which represents a 21.7 wt%, 41.5 wt%, 81.8 wt% and 9.4 wt% increase in SO_4, Fe, Al, and Mn, respectively, removal efficiency compared to the predominantly ligneous bioreactors. These results imply that ASRB technologies are promising in remediation of coal-generated AMD and increasing herbaceous content of bioreactors can significantly enhance contaminant sequestration. However, in order to enhance ASRB remediation capacity, future designs must optimize not only the organic carbon substrate but also include a pretreatment phase in which the bulk of dissolved Fe/Al-species are removed from the influent AMD prior to entering the bioreactor because: 1) a seasonal variation in redox gradients that could induce dissolution of the already formed redox sensitive phases also was recorded and 2) microbially-mediated sulfate reduction may be inhibited by the high surface areas of the abundant Fe/Al-oxyhydroxides, which dominate the system.

Work planned for this research by task number:

Tasks	Status	Target Date
1. Obtain the necessary field and laboratory equipment and supplies	Completed	Completed
2. Construct facilities	Completed	Completed
3. Collect field measurements and monthly samples at the existing Tab Simco bioreactor	Completed	Completed
4. Conduct laboratory tests and data compilation	Completed	Completed
5. Demonstrate improved sampling and analytical methods	Completed	Completed
6. Evaluate results from field- and bench-scale testing scale	Completed	Completed
7. Prepare and present technology transfer of preliminary results according to the technology transfer plan including an Interim Report	Completed	Completed

1. Introduction

In the late 1970's over 200,000 acres of land had been documented as being affected by coal mining activities in the state of Illinois alone (FWPCA, 2002). Coal-derived AMD occurs from weathering of both inorganic and organic material which promotes the mobilization of anions (e.g., SO_4^{2-}, Cl^-, F^-) and metals (Fe, Al, Cd, Sr, Ni, Cu, Co, Mn, Zn, As) both into the ground and surface waters (Gammons et al., 2010; Freitas et al., 2011). Most notably the oxidation of pyrite (FeS_2), the most common sulfide mineral frequently associated with coal and waste rocks, causes the mobilization of Fe(II) and SO_4^{2-} in high concentrations (Nieto et al., 2013; Doulati Ardejani et al., 2010).

Sulfide oxidation is typically the main concern in AMD remediation plans since it can result in pH decreases and subsequent release of addition trace metals. The following general reaction describes pyrite oxidation (Neculita et al., 2007):

$$FeS_2(s) + 3.5O_2(aq) + H_2O(l) \rightarrow Fe^{2+} + 2H^+(aq) + 2SO_4^{2-}(aq)$$

Further oxidation of the ferrous iron involves consumption of dissolved oxygen and protons in solution producing the ferric ion (Wang et al., 2013a):

$$4Fe^{2+} + O_2(aq) + 4H^+ \rightarrow 4Fe^{3+} + 2H_2O(l)$$

Although ferrous ion oxidation kinetics in acidic environments similar to AMD have been reported as negligible through abiotic mechanisms, microorganisms such as *Acidothiobacillus ferrooxydans* are exceptionally capable of catalyzing ferrous iron oxidation (Wang et al., 2013a). Consequently free ferric species in solution participate in multiple reactions such as hydrolysis,

mineral phase formations/transformations while even acting as a powerful oxidant for additional sulfide dissolution as follows:

Hydrolysis (Daoud and Karamanev, 2006):

$$Fe^{3+} + 2H_2O \rightarrow Fe(OH)_3 + 3H^+$$

Jarosite Formation (Daoud and Karamanev, 2006):

$$K^+ + 3Fe^{3+} + 6H_2O + 2HSO_4^{2-} \rightarrow KFe_3(SO_4)_2(OH)_6 + 8H^+$$

Pyrite Oxidation (Hubbard et al., 2009; Nordstrom et al., 2000):

$$FeS_2(s) + 14Fe^{3+} + 8H_2O \rightarrow 15Fe^{2+} + 2SO_4^{2-} + 16H^+$$

Each of these reactions causes an increase in proton concentration resulting in further leaching of metal contaminants. In terms of acid mine drainage, overall acid generation due to sulfide oxidation is mainly represented by the following equation (Bigham and Nordstrom, 2000a):

$$4FeS_2(s) + 15O_2 + 14H_2O \rightarrow 4Fe(OH)_3 + 8SO_4^{2-} + 16H^+$$

Because pyrite is an omnipresent mineral in rocks associated with coal-bearing strata and, in some cases,found in relatively large quantities. the weathering of pyrite under aerobic conditions can be the source of acidic waters loaded with metals for prolonged periods of time (Nieto et al., 2013). Depending on specific physical and chemical conditions (e.g. pH, Eh, temperature of the waters, and saturation indices (SI) of associated minerals), the dissolved metals can remain in solution over long distances, traveling far from the original source of contamination (Olías et al., 2006; Olías et al., 2004).

AMD remediation requires prolonged alkalinity production and successive mineral precipitation. To achieve this, treatment options can incorporate abiotic mineralization, biologic mineralization or both into an “active” or “passive” type system. Anaerobic sulfate reducing bioreactors (**ASRB**) can function as passive systems in which the influent drainage is continuously treated with no operational supervision. Usually these reactors consist of a top compost layer underlain by limestone aggregate. In essence the compost layer provides substrate to influence the consumption of dissolved oxygen via microbial degradation processes while the limestone aggregate maintains alkalinity (McCauley et al., 2009; Neculita et al., 2007; Behum et al., 2011).

This promising technology often succeeds in providing short-term, low-cost systems for treatment of acid mine discharges. Still long-term treatment efficiency (>10a) is not readily accomplished and costly maintenance is required to keep these systems working effectively (Zagury et al., 2007). Therefore, ancillary data on the technological limitations are essential in future designs of long-term and effective ASRB treatment systems.

Previous work has identified contaminant retention time, exhaustion of organic substrates, precipitate-induced reduction of reactive surface area, and degeneration of system permeability as possible limits to long-lived ASRB performance (Blowes et al., 2009; Lindsay et al., 2011; Neculita et al., 2008; Zagury et al., 2007). In the present study, bioreactor organic substrate composition was tested in the field to define whether available organic material was the key factor controlling effective and longstanding remediation of coal-derived acid mine drainage.

1.2 Site description and AMD remediation history

Tab-Simco is an abandoned coal mine comprised of a 12 ha U-shaped hill that rises 37 meters above the surrounding lowland and is located approximately 6 km SE of Carbondale, Illinois (Behum et al., 2011; Fig. 1).

Figure 1: Photograph of acidic iron oxide (ochre) sediment deposited in a floodplain at the Tab-Simco AML site in southern Illinois. View is taken in a north-easterly direction with the location of the main AMD seep being upstream to the left.

Approximately 12 ha (29.7 ac) of the Murphysboro coal seam [~2 m (6.6 ft.) thick] and 3 ha (7.4 ac) of the overlying the Pennsylvanian-age Mt. Rorah coal seam (0-1.5 m thick) were room-and-pillar mined. The seams are separated by 3-8 m (9.8–26.3 ft.) of shale and the Mt. Rorah coal seam is capped by up to 10 m (32.8 ft.) of fractured sandstone. Even with annual dry and wet seasons the floodplain adjacent to the Tab-Simco site experienced a relatively consistent base flow of ~150 m^3/day (150,000 L/day or 39,600 GPD) from acid mine drainage derived from five seeps with a pH ranging between 2.3 to 2.9 (Smith, 2002).

In 2007, the Illinois Department of Natural Resources (IDNR) constructed a passive-type treatment system that on average treated 1.35L/s (21.4 gpm) of acid mine drainage produced from the Tab-Simco abandoned coal mine (Behum et al., 2010; Behum, 2011; Behum, 2012; and Lewis, 2008). Among other contaminants detected within the AMD, the Tab-Simco site had notably high concentrations of dissolved iron (900 mg/L), aluminum (200 mg/l), manganese (40 mg/l), sulfate (5,000 mg/l) and a pH and total acidity of 2.7 and 1,816 (mg/l CCE), respectively

(Behum et al., 2011). In order to passively sequester such high sulfate and metal loads a remediation system involving an anaerobic sulfate reducing bioreactor using a mixture of woodchips, straw, and yard waste as organic substrate was constructed in 2007 (Fig. 2). During the first two years metal removal was efficient recording a reduction of 75.6% Fe, 99.6% Al, 97.1% Ni, and 93.4% Zn (Behum et al., 2010). As the system matured during the first five years of operation both metal and sulfate removal began to decline. The current study, therefore, focuses on how using an alternate organic substrate to improve the efficiency and longevity of the **ASRB** remediation technology.

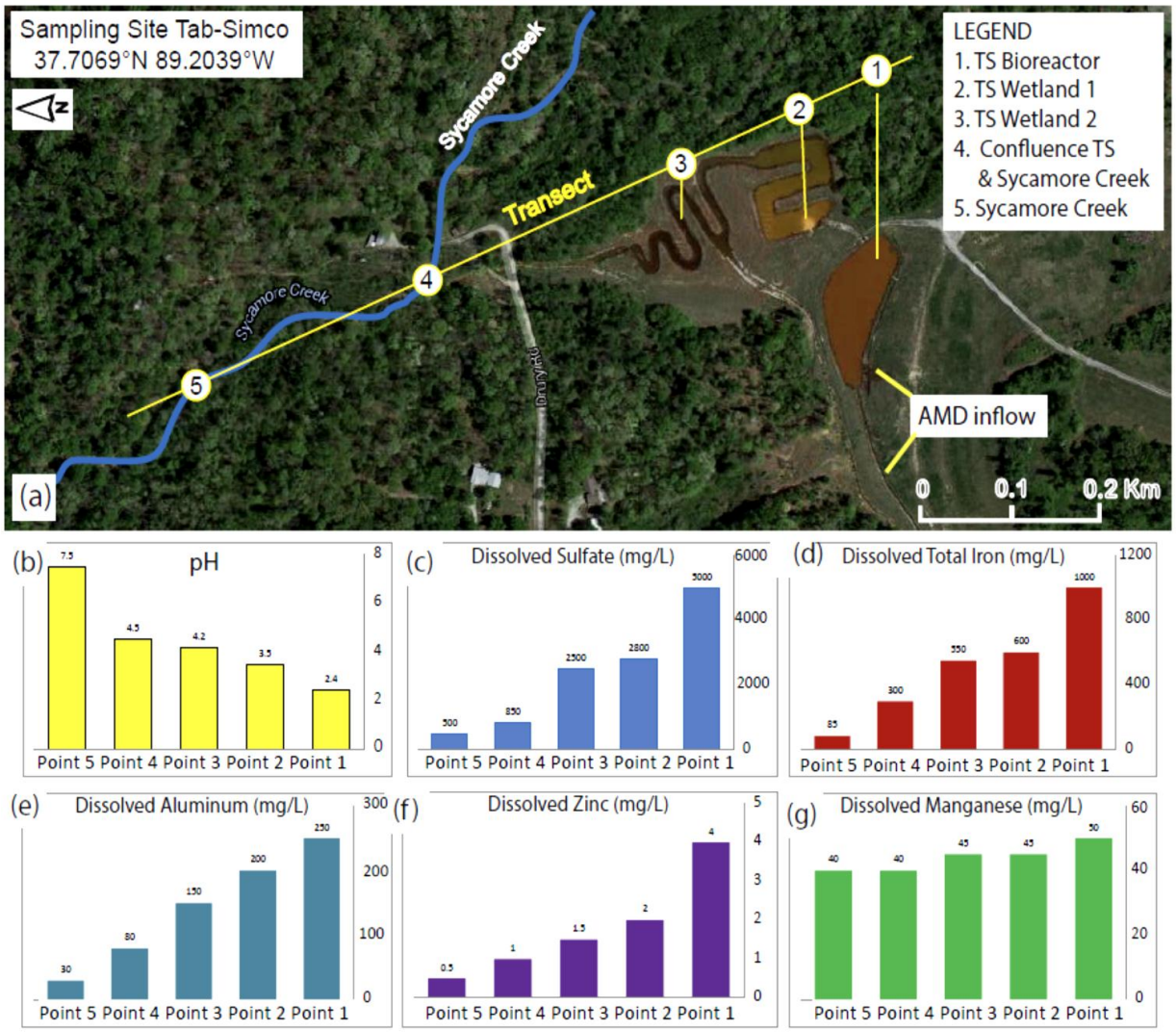

Figure 2: (a) Aerial view of the Tab Simco bioremediation field site in Southern Illinois following failure due to short-circuiting. In this project, surface effluent and sediments were sampled for microbial, mineralogical and geochemical characterization along a transect at different sampling points. (b) – (g) Geochemical characteristics of surface effluent at the five sampling sites (geochemical data acquired in August, 2013).

2. Materials and methods

2.1 Reactor Construction

Six 210-liter (55-gallon) polyethylene barrels served as the model passive treatment reactors and held the six different treatment media mixtures selected for this experiment. The top of each barrel was cut open to allow AMD to passively flow into the reactor, simulating a shallow acid impoundment analogous to the full-scale bioreactor at Tab-Simco. Three syringe extraction ports were located at different depths of the reactor, along with an effluent discharge port, were installed by drilling 1¼''-diameter holes into the sides of the barrels and inserting 1¼'' polypropylene bulkhead fittings to hold the ports in place.

Bulkhead fittings had outer threaded diameters (OD) of 1¼'' which were mounted snugly into the drilled holes with the exterior of the reactor pressed up against a thick rubber gasket fitted onto the bulkhead screw. On the interior of the reactor a 1¼''-inner diameter (ID) coupling was wrenched tightly onto the bulkhead fitting creating a bulge in the exterior rubber gasket inducing an impermeable seal. Bulkhead fittings contained ½''(ID)-threaded female reducing connectors in which Teflon wrapped ½'' threaded male connectors with ½'' non-threaded female openings were screwed in place to house the sampling ports (syringe extraction, effluent).

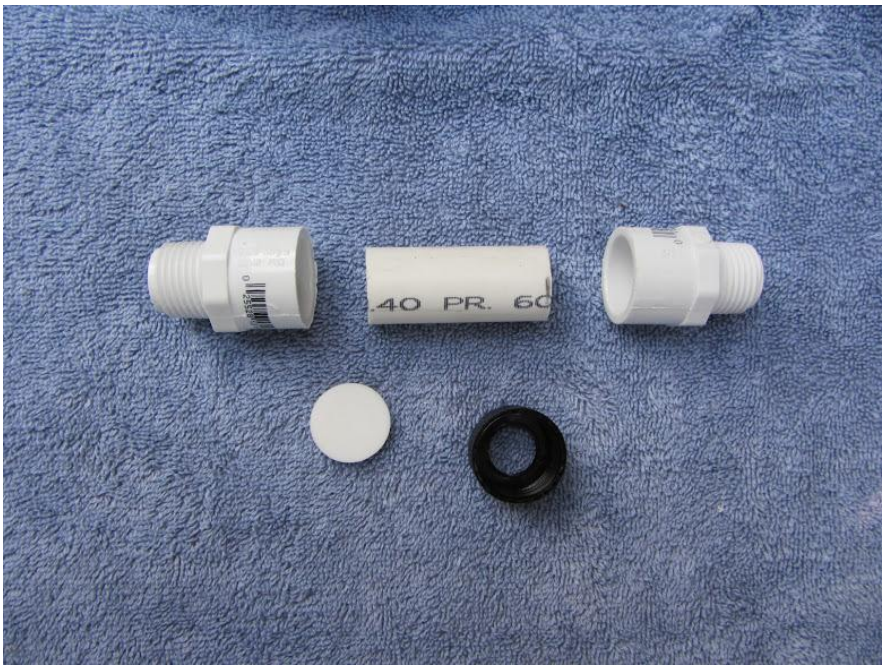

Figure 3: Components of extraction port for each reactor showing (1) two hybrid treaded/non-threaded PVC-connectors (top left/right), (2) one four-inch length of ½''-(OD) PVC-piping (top middle) and (3) one ½''-(OD) silicone septum (bottom left). Silicon septum were placed on one end of the PVC-piping and inserted into the non-threaded side of one connector to allow syringe extraction.

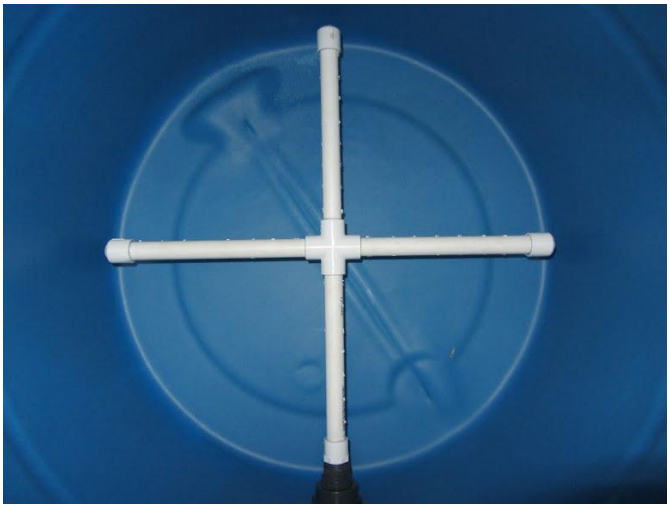

Figure 4: View downward into an assembled reactor displaying perforated "+"-shaped effluent drainage design to allow a spatially equivalent collection of fluid to exit the reactor.

Extraction ports were constructed by cutting 4'' lengths of ½"-(OD) PVC piping (Sch. 40) and placing ½''-(OD) silicone septa between one end of the PVC piping while sealing it into a non-treaded ½''-(ID) connector with Weld-On® PVC cement (Figure 3). These extraction ports were then fastened to the top three ½''-(ID) non-threaded female connectors on each reactor again with Weld-On® PVC cement. As for the effluent ports, perforated "+"-shaped ½''-PVC piping was fastened to the interior of lower bulkhead fitting to evenly distribute the treated AMD as it exits the reactor (Figure 4). Finally, ½'' ball-valves were sealed with Weld-On® PVC cement to the effluent piping allowing a flow-rate of ~5mL/min. to be maintained.

2.2 Weir-System Construction

A weir system was built within the Tab-Simco AMD collection ditch downstream from the main seep to impound the influent AMD and to continuously measure flow. The impoundment increased the hydrologic head and allowed gravity fed drainage into each separate reactor for the duration of the experiment (Figure 5). To create this weir a 6''-wide trench was first excavated in the channel-way roughly one foot in depth and perpendicular to the drainage flow-path. Nominal inch thick ply-wood was then fitted into the trench to create a temporary "dam" structure with a "V"-notched weir incised at the top to create o flow monitoring point. Three six-foot long, steel fence T-posts were hammered into the ground along the weir on the downstream side to provide additional integrity to the structure.

Quikrete® concrete mix was then poured in the trench on both sides of the plywood to cement and seal the weir base. To transport the impounded AMD into each reactor a 2 ¼'' hole was drilled into the plywood where a 2 ¼''-(OD) bulkhead fitting with 1''-(ID) thread was then fastened. A foot length of 1''-(OD) PVC piping was perforated, dry-connected to the interior of the bulkhead fitting (i.e. impoundment side) and dry-capped to prevent frequent clogging by large particulate. On the down-stream side, ten foot long 1''-(OD) PVC piping was dry-connected to a 1''-(ID) non-treaded female/threaded male hybrid connector and fastened to the exterior bulkhead fitting. Four of the ten foot long 1''-(OD) PVC piping were dry-connected downstream by 1''-(ID) dual non-threaded female fittings and held in place six foot fence post

driven into the ground. As the piping extended further from the weir structure slight decreases in topographic elevation allowed a gain in PVC height while sustaining influent flow.

To provide the final increase in PVC height needed to gravitationally feed the reactors a 1''to ½''-(ID) dual non-threaded female reducing elbow connector was added to decrease flow-path volume and increase flow-rate upwards. This allowed one foot of vertical elevation to be added with ½''-(OD) PVC piping giving the necessary height to continuously feed each reactor. For ease of cleaning in the case of clogging, all PVC piping used in the weir system was dry-fitted to allow it to be quickly disassembled, cleaned and re-assembled.

Figure 5: Photograph of weir constructed along with installed PVC to channel AMD into the test cells. A continuously-recording flow sensor is installed in the adjacent PVC stilling well.

2.3 Reactor Installation

Three wooden pallets were placed in the channel-way near the end of the influent PVC piping previously mentioned. Two reactors were place side-by-side on each pallet while ½''-(OD) PVC piping was extended out between each reactor set per pallet. Once the piping reached a set of reactors, non-threaded cross-fittings we added to transport AMD influent to each barrel with the flow metered by ½''-(ID) ball valves. The main PVC line then continued downstream to feed the other sets of reactors (Figure 7). The downstream end main line was seal-capped to create hydrologic back-pressure, ensuring a continual flow to all six reactors.

2.4 Reactor Composition

Predetermined mixtures of herbaceous (hemicellulose) and ligneous (woody) organic substrates with a total uncompressed volume of 125L (4.4 ft^3) were added to each of the five biologic reactors. A 25 liter (0.88 ft^3) layer of limestone was added to the bottom of each reactor to produce alkalinity while maintaining permeability.

Reactor one was designed as a control containing only 25L (0.88 ft^3) limestone as its total solid volume, acting as an open limestone pond-type system. Therefore, the remaining

185 liters (40.7 gal) of Reactor One was a pool of impounded AMD influent. Sediment sizes of limestone used ranged from cobbles (64-130mm), pebbles (2-64mm) and sand (0.0625-2mm) and were added in equal proportions within the total limestone volume.

Figure 6: Photograph of reactors actively receiving AMD influent at the Tab-Simco AML site. A main PVC pipeline extends over the three pairs of reactors in which cross fittings allow AMD to be distributed in each reactor.

Figure 7: Master student Evan R. Walters collecting samples in the field.

The following organic substrates representing materials available in the region were used in the remaining five reactors: leaf compost (LC), grass clippings (GC), spent brewing grain (SBG), maple wood chips (MWC) and maple sawdust (MSD). To test the longevity of ASRB's based on substrate composition, the organic material was classified as containing herbacious

(i.e. LC, GC and SBG) or ligneous (i.e. MWC and MSD) as its dominant composition and added to each biologic reactor in various proportions (Table 1). Within each biologic reactor, 4 gallons of livestock manure and 7.8 L (2-gal.) of whey powder were mixed into the organic material to inoculate sulfate reducing bacteria and provide an immediate source of low molecular weight organic compounds. At the top of the bioreactors, the remaining 54 liters (11.9 gal) were open to the surrounding atmosphere and provided space for the AMD to pool.

Table 1: Distribution of Organic Substances, Limestone and SRB Inoculum within Each Test Reactor

Substrate	Reactor 1 Limestone	Reactor 2 (10:90)	Reactor 3 (30:70)	Reactor 4 (50:50)	Reactor 5 (70:30)	Reactor 6 (90:10)
LC %(v/v)	0	4%	12%	20%	28%	36%
SBG %(v/v)	0	2%	6%	10%	14%	18%
GC %(v/v)	0	4%	12%	20%	28%	36%
Total Herbaceous	**0**	**10%**	**30%**	**50%**	**70%**	**90%**
MWC %(v/v)	0	45%	35%	25%	15%	5%
MSD %(v/v)	0	45%	35%	25%	15%	5%
Total Ligneous	**0**	**90%**	**70%**	**50%**	**30%**	**10%**
LS (Liter)	25	25	25	25	25	25
LM (Liter)	0	4	4	4	4	4
SWP (Liter)	0	2	2	2	2	2

Table 1: Leaf Compost (LC), Spent Brewing Grain (SBG), Grass Clippings (GC), Maple Wood Chips (MWC), Maple Sawdust (MSD), Limestone (LS), Livestock Manure (LM), Sweet Whey Powder (SWP)

2.6 Field Measurements

Field measurements (pH, ORP, conductivity, temperature, D.O.) were performed at the AMD influent, acid pond of each reactor and effluent port of each reactor using a Hanna® multi-parameter probe. Free proton concentrations (i.e. pH) of samples were documented specifically with a Hanna HI769828-1 field probe (pH/ORP) calibrated to Orion (1.68, 4.01, 7.00) buffer solutions using guidelines described in that factory provided calibration manual (Hanna, 2012). Electric conductivity was measured using Hanna HI769828-3 stainless steel EC probe calibrated at a single point with 5,000 µS/cm standard solution (Hanna Instruments® (HI9828-25)). Solution oxidation reduction potential (ORP) was analyzed using factory calibrated Hanna HI769828-1 Ag/AgCl field probe at one custom point.

Ranges for oxidation reduction potential fall between ±2,000mV (2 V) with ±1.0mV accuracy and resolution of 0.1mV (Hanna, 2012). As per manufacturer's requirement ORP values were checked against pH prior to all sampling events and maintenance using reducing/oxidizing pretreatment solutions (HI 7091L and HI7092L) was performed when necessary (Hanna, 2012). Dissolved oxygen (DO) was determined with a Hanna HI769828-2 field

probe calibrated to on site atmospheric oxygen as 100% DO under manufacturer's requirements (Hanna, 2012).

The membrane and electrolyte filling solution (HI 76409A/P & HI7042S) for the DO sensor was changed prior to each sampling event to ensure rapid response time and increased accuracy (Hanna, 2012). Temperature was also measured with the fore-mentioned field probe throughout the entirety of the experiments. AMD influent and effluent rates were quantified using a 10mL volumetric flask and timed on a stop watch.

2.7 Sample Collection

Samples were collected for dissolved species analyses from the AMD influent and effluent port of each reactor in 250mL polyethylene bottles with care to minimize exposure to atmospheric conditions (Myers, 2006). Three graduated sampling ports with silicone septa for syringe extraction of aqueous samples were placed on each reactor for microbial community analyses at increasing depth from the acid pond.

All samples collected on site were stored near field temperatures until alkalinity measurements were performed to prevent temperature induced partitioning of gaseous species into the aqueous phase (Rounds, 2012). Within 30 minutes of collection, samples arrived at the Southern Illinois University Carbondale geochemistry laboratory where further chemical analyses were carried out.

2.8 Laboratory Analyses

All laboratory equipment (i.e. glassware, sampling bottles, etc.) used during analytical processing was soaked in distilled water immediately after use until a thorough washing could be performed (Groat, 2004). Washing involved scrubbing equipment for ten seconds with test tube brush, rinsing with steady stream of distilled water for ten seconds followed by three flushing's with distilled water and an additional ten second rinse with distilled water. If visible scale had formed on laboratory equipment an overnight soak in 5% nitric acid (ACS certified) solution along with the previously outlined washing procedure was performed. In severe cases in which 5% nitric soak would not remove scale, a saturated solution of RoVer® rust remover (i.e. $NaHSO_3$ and $Na_2S_2O_4$) was prepared and samples were soaked overnight followed by the washing procedure. Upon arrival to the laboratory samples were immediately filtered with 0.45 µm cellulose acetate filter papers (Millpore® HAW) to ensure future analyses would represent dissolved constituents only.

2.8.1 Alkalinity

Once filtered, total alkalinity was performed using a Hach® digital titration test kit (Model AL-DT) to an end-point (pH=4.5) measured with the Hanna® multi-parameter probe previously described (Method 10244, 2011). Briefly, 25mL of sample was measured in a volumetric flask (class A) and transferred to a 100mL class A volumetric flask (VF). To wash out any residual sample, two 25mL portions of distilled water were added to the original 25mL volumetric flask (VF), swirled momentarily and then added to the 100mL VF containing sample. Next the 100mL VF was filled to the 100mL mark with distilled water; inverted ten times to mix and then added to a 250mL plastic beaker. Using the calibrated pH probe, while stirring, 0.16N sulfuric acid was added drop-wise with a digital titrator (Item #1690001) until sample pH reached 4.5 units at

which the digit reading was recorded. Once end-point was reached, total alkalinity as meq/L of $CaCO_3$ was calculated according to the method guidelines. Immediately after alkalinity measurements filtered samples were refrigerated at ~8°C to slow down any reaction kinetics.

2.8.2 Dissolved Sulfide and Ferrous

Dissolved sulfide and ferrous iron measurements were carried out on filtered samples within five hours of original raw sample collection to avoid oxidation of these species. Dissolved sulfide and ferrous iron were measured using a UV-VIS spectrophotometer (Hach® DR 3900) via USEPA methylene blue and 1-10 phenanthroline methods, respectively (USEPA, 2013). In short, samples were diluted for each measurement with distilled water separately to fall within the concentration range for optimal certainty. Typical dilution factors ranged between 1 to 20 and 50 to 300 for sulfide and ferrous iron, respectively. Once optimal dilution concentrations were achieved reagents were added to each sample according to outlined procedures and color was allowed to develop for the allotted time within each sample. After reaction periods expired and the spectrophotometer was zeroed with a blank, samples were transferred to quartz cuvettes (Item # 2495402), placed in the spectra holding cell and concentration was measured relative to sample absorbance at the pre-programed wavelength.

2.8.3 Anions (Sulfate, Chloride, Fluoride)

Filtered samples were subsequently analyzed for dissolved anionic species (SO_4^{2-}, Cl^-, F^-) by means of ion chromatography (Dionex® ICS 2000) using an IonPac® AS18 anion-exchange column. Stock standard solutions were prepared by separately weighing ACS-certified sodium chloride (NaCl), anhydrous sodium sulfate (Na_2SO_4) and sodium fluoride (NaF) with a Mettler® AE100 balances. Crystalline standards were then transferred to a 100mL VF (class A) and dissolved in MilliQ® (18MΩ) ultra-pure water. Serial dilutions of stock solutions were subsequently performed by pipetting sample into a class A volumetric flask with a 200 µL or 5 mL Finnpipette® depending on the dilution factor required and flask used. Volumetric flasks were then filled using MilliQ® (18 MΩ) ultra-pure water until the bottom of the meniscus reached the volumetric line. Standards were then inverted 10 times to mix, poured in Dionex® AS-DV sampling vials (P/N 068947) and prepared following manufacturer's requirements (Thermo Scientific, 2012). Serial dilutions of standards were prepared to develop a four point calibration curve (zero representing baseline drift) that fell in the optimal concentration range obtainable for an IonPac® AS18 anion-exchange column.

Due to the high mole ration of sulfate and iron, hydrated complexes (i.e. hexa-coordinated aquo complexes) undoubtedly form between these species and therefore made it difficult to obtain sulfate values due to peak broadening on the chromatogram. To prevent the complex-induced thickening of the sulfate ion-exchange bands, samples were pretreated with 0.1M NaOH to remove dissolved iron species. Sodium hydroxide addition had an ancillary effect of precipitating dissolved sulfide from bioreactor samples which prevents any oxidative formation of sulfate species. Dilutions caused by sodium hydroxide additions were accounted for and factored in to the final dilution required to place species concentrations within the calibration curve. To confirm the accuracy of this technique gravimetric analysis via $BaSO_4$ precipitation (Method 375.3; USEPA) was performed on the same samples and compared to the values obtained through ion chromatography (Figure 8). Overall the gravimetric results were on

average 14% higher than that of the IC results and which is consistent with the USEPA method. USEPA method 375.3, suggests that samples with high silica and organic content cause interferences resulting in overestimation of sulfate concentrations. Furthermore geochemical modeling of each samples charge-balance identifies the sulfate concentration is slightly over-estimated by gravimetric results and underestimated by IC results. Therefore, it was determined that averaging results obtained through both techniques would provide most accurate sulfate values.

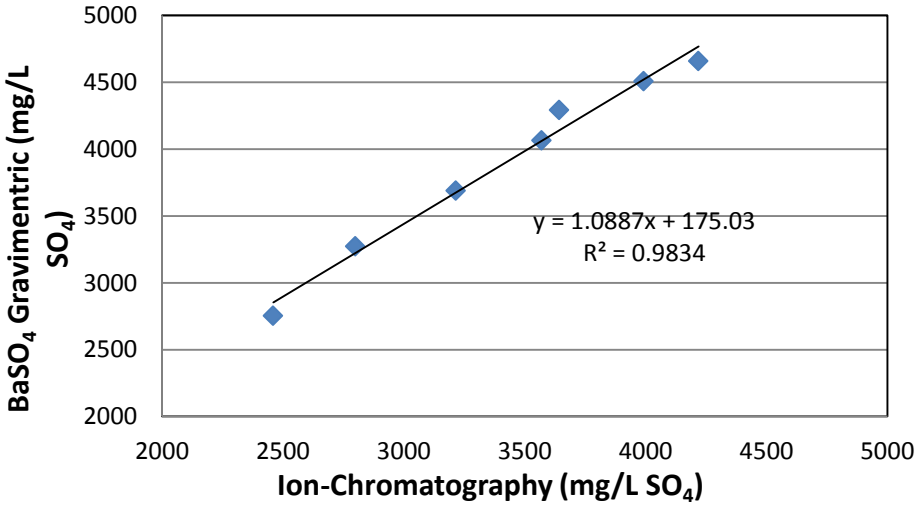

Figure 8: Linear regression of sulfate values measured via gravimetric analysis and ion-chromatography. Plot indicates that a 14% increase in sulfate values from IC to gravimetric is persistent (R^2 = 0.98) throughout a wide range of sulfate values indicating consistent overestimation.

2.8.4 Phosphate

Phosphate was measured using the vanadomolybdophosphoric acid colorimetric method (APHA, 2005). Briefly, ammonium metavanadate ($(NH_4)VO_3$) was prepared from vanadium pentoxide (V_2O_5) by placing 2 g of sodium carbonate (Na_2CO_3) under reflux in 15 mL of distilled water until completely dissolved. Next, while maintaining a warm solution, 3.5 g of vanadium pentoxide was added in small portions converting it into soluble sodium vanadate and exsolving carbon dioxide. After reaction subsided (i.e. solution went from yellow to clear), 2.0 g of ammonium chloride was dissolved in 7.5 mL of distilled water and poured slowly into the hot sodium vanadate solution.

Solution was allowed to cool to room temperature and then placed in an ice bath to enhance the formation of white ammonium metavanadate crystals ($(NH_4)VO_3$). Crystals were then vacuum filtered, washed with excessive amounts of distilled water, scraped onto a clean watch glass and placed in an oven to dry at 100°C. Once dried, 1.25 g of ammonium metavanadate crystals were dissolved in 300 mL of distilled water that was brought to a boil under reflux conditions. Next, the ammonium metavanadate solution was cooled to room temperature and 330 mL of concentrated HCl (ACS certified) was added. A separate solution containing 25 g of ammonium molybdate $(NH_4)_6Mo_7O_{24}{\cdot}4H_2O$ was dissolved in 300mL distilled water and added to the ammonium metavanadate solution after the heat produced from the

HCl addition had subsided. Finally, the 930mL of reagent was brought 1L by adding distilled water in a 1L (class A) volumetric flask. A stock phosphate standard solution was prepared by dissolving ACS-certified sodium phosphate tribasic dodecahydrate ($Na_3PO_4 \cdot 12H_2O$) crystals in MilliQ® (18MΩ) ultra-pure water. Serial dilution of the stock phosphate solution was performed to create a five-point calibration curve which was personally programmed on a UV-Vis spectrophotometer (Hach DR 3900). In short, the program was set in the visible spectrum at a wavelength of 400nm and calibrated to phosphate standards of (1.0, 5.0, 10.0, 15.0 and 20.0) mg/L-PO_4. Color development of both standards and samples was achieved by adding 35mL of sample to a 50mL (class A) volumetric flask followed by a 10mL addition of the vanadomolybdophosphoric acid reagent and filling the rest of the VF with distilled water. Blank samples were prepared by replacing the 35mL of sample with distilled water. Color was allowed to develop for 15 minutes and the phosphate concentration was measured relative to its absorbance at 400nm using a UV-Vis spectrophotometer (Hach DR 3900).

2.8.5 Cation Analyses

To preserve dissolved cations, immediately after samples were filtered a 100mL fraction of the filtrate was measured volumetrically and acidified to a 5% nitric acid (ACS certified) solution. Metal analyses (Fe, Mn, Cu, Sr, Cd, Ni, Zn, Ca, Mg, K) were perform via atomic absorption spectrophotometry (Z-2000 Tandem AA) using teledyne plasma-pure® stock aqueous metal standards. Each stock metal standard contained 1,000ppm metal cation solvated in a 5% nitric acid solution. In short, standards were prepared by pipetting each stock metal standard to a 1 L (class A) volumetric flask using a 200 µL or 5 mL Finnpipette® depending on final concentration required. Once addition of all metal standards was completed, MilliQ® (18MΩ) ultra-pure water containing 5% nitric acid (ACS certified) was added until sample meniscus reached the 1L mark. Depending on the optimal linear response of each metal cation up to five points of calibration (minimum of three) were created using separately prepared mixed-metal standard solutions following the fore-mentioned guidelines. MilliQ® (18MΩ) ultra-pure water containing 5% nitric acid (ACS certified) was tested against MilliQ®(18MΩ) water without nitric acid and no difference in background absorbance was detected under all cathode lamps used for metal measurements. Therefore nitric acid addition to samples did not account for increased absorbance of any metal and thus only a 5% dilution factor was accounted for in the results. Furthermore MilliQ®(18 MΩ) ultra-pure water without nitric acid was used as a blank within the calibration curve primarily to prevent corrosive wear on the instrument from the continued aspiration of a 5% nitric acid solution (Hitachi, 2004).

2.8.6 Sulfur Isotope Analysis

After samples were filtered to 0.45 µm, a 50 mL fraction of filtrate was measured in a 50 mL VF (class A). Next the sample was transferred to a 100 mL beaker, acidified to a pH of roughly 2.0 units (if needed), covered with a watch glass and placed on a hot plate. Samples were warmed to 80°C and barium sulfate precipitation was performed through drop-wise addition of saturated barium chloride ($BaCl_2$) solution (Method 375.3; USEPA). Once no visible precipitate was forming after the addition of $BaCl_2$, an excess of 1 mL $BaCl_2$ solution was added to ensure complete precipitation and solution was kept at 80°C for another hour. To promote crystal growth samples were left on hot plate overnight at 45°C. Finally, barium sulfate ($BaSO_4$) crystals

were separated from supernatant, dried in the oven at 100°C and sent to the mass spectrometry facility at Indiana University Bloomington for sulfur isotope analysis. A Finnigan MAT 252 mass spectrometer equipped with an elemental analyzer was used to determine sulfur isotopic compositions of the $BaSO_4$ precipitates mentioned previously using methods outline by Lefticariu (Lefticariu et al., 2006).

2.8.7 Aluminum Measurements: Aluminum concentrations were measured on a Hach DR3900 spectrophotometer using the acidified sample (5% nitric) which was also prepared for AAS analyses. Since dilution factors up to 300 were required to fall within the Aluminon method (Hach, 2013) range (0.008 – 0.800 mg/L) it was unnecessary to raise that sample pH > 3.5 as recommended by the manufacturer. In brief, after samples were diluted to fall within the calibration range, one packet of ascorbic acid (C/N 1457799) was dissolved completely in 50mL of sample. Next one AluVer 3 (C/N 1429099) reagent packet was added to the sample and inverted for one minute as the sample developed a red-orange color. A blank was prepared by transferring a 10 mL fraction of the colored sample to a quartz cuvette along with one Bleaching 3 (C/N 1429449) reagent package and swirled vigorously for 30 seconds. Finally both sample and blank were allowed to react for 15 minutes followed by zeroing the instrument with the blank and measuring the absorbance of the sample. Since fluoride ions interfere at all concentration levels, aluminum concentrations were corrected for this interference as outlined in the manufacturer's method (Hach, 2013).

2.8.9 Microbial Measurements: In collaboration with SIUC Department of Microbiology, pyrosequencing of bacterial communities was performed at sampling ports and effluent portals of each reactor a week after the experiment began and after 12 months of operation (Pugh, 2013). Duplicate DNA extractions where taken from both water and solids from each reactor. Solid DNA extraction was carried out using a FastDNA SPIN® Kit for Soil under manufacturer's protocol (Biomedicals, 2013). 16S rRNA gene pyrosequencing was performed on the resultant DNAs at Molecular Research (Shallowater, Texas). Evaluation of samples were generated using Tag-encoded FLX amplicon pyrosequencing (bTEFAP) ran on a 70675 GS PicoTiter Plate using the Genome Sequencer FLX System (Roche), under methods described by Shange (Shange et al., 2012). To effectively model bacterial communities present, sequences will be sorted by operational taxonomic units (OTUs) at 3% sequence similarity. To complement the pyrosequencing results, fluorescent in situ hybridization (FISH) will be carried out on samples extracted every three months to define the microbial diversity within each reactor at a Class and Domain level. Standard protocol outlined in Amann et al. was carried out to properly identify microbial communities using the FISH technique (Amann and Fuchs, 2008).

3. Results

3.1 System Parameters

3.1.1 Temperature

Southern Illinois is described as a region of temperate climate that experiences extreme temperature fluctuations both annually and daily. During the experiment all reactors had been exposed to temperatures below -13°C (8°F) and above 35°C (96°F). Water temperatures

measured in the field closely resembled the average daily recorded ambient air temperatures of the local area (Figure 9). Within any given sampling point the average standard deviation in temperature between each reactor was ±0.54°C which was slightly greater than the instruments tolerance level of ±0.15°C.

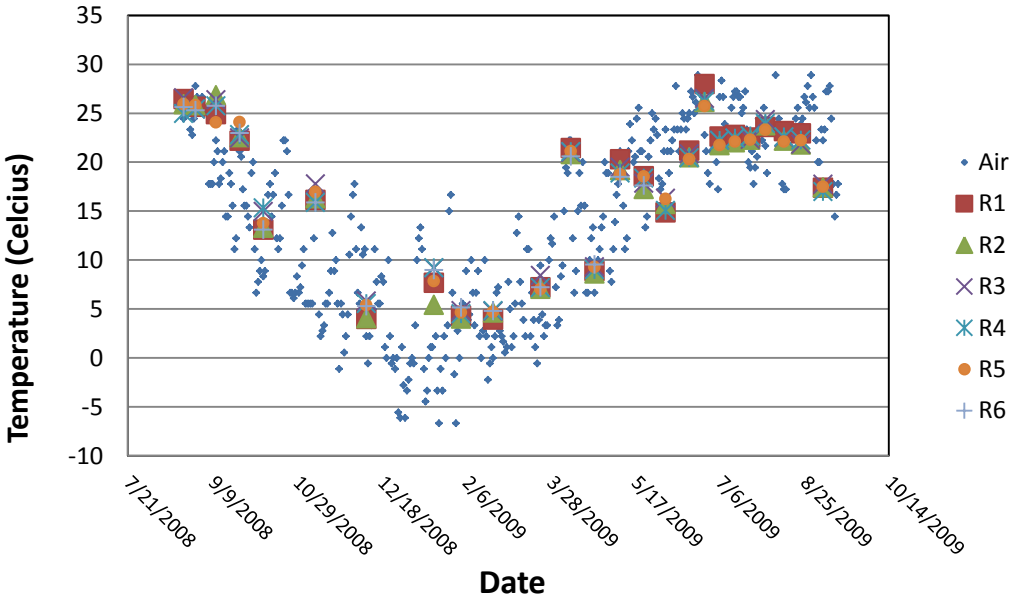

Figure 9: Comparison of ambient air temperatures and effluent temperatures recorded for each reactor during the duration of these experiments at Tab Simco site.

3.1.2 pH Values

Free proton concentrations were recorded in influent AMD, acid impoundments and effluent ports within each reactor. Influent pH values were relatively consistent throughout the experiment with an overall average and standard deviation of 2.80 ± 0.15. Interestingly, the average pH values recorded in the acid pond of reactor 1 (Limestone only) was 2.62 ± 0.25, which was 0.18 units less than that of the influent AMD (Figure 10). Average effluent pH values for the control reactor (R1) were also significantly stable and had been documented as 3.34 ± 0.40, which was 0.54 units higher than the average influent AMD values (Figure 11). As for the biologic reactors, an increase in effluent pH was seen in all reactors from August to early December 2012. In the following four months (January 2013-April 2013) the dominantly ligneous (woody) reactors (R2, R3) displayed substantial decreases in effluent pH values relative to R4, R5 and R6. As the experiment continued, all reactors began to exhibit gradual decreases in pH with a recent plateau around 4.0.

Overall, ligneous reactors (R2, R3) displayed a median effluent pH of 4.77 ± 0.65 while the herbaceous reactors (R5, R6) had an average pH of 5.11 ± 0.77. As for reactor 4 (50:50, herbaceous: ligneous), the median effluent pH value fell in between and was measured as 4.98 ± 0.8. Measurements of the acid impoundment (AI) of the biologic reactors displayed two peaks in pH values, one ~3 weeks after the experiment began and another ~14 weeks after commencement. The first of the two peaks were measured in all bioreactors while the second peak was most apparent in R3, R4 and R5. Recent measurements within the bioreactors show a transition in pH values that is similar to values exhibited in the acid impoundment of reactor 1.

This transition began eight months after the experiment commenced and display a pronounced decline in pH recorded within all bioreactors AI measurements. On average the pH values within all the biologic reactors since March 2013 was 2.56 ± 0.3 while influent pH was 2.76 ± 0.14 during this time. This change marks an average pH decrease of 0.20 units from influent AMD to each of the biologic reactors.

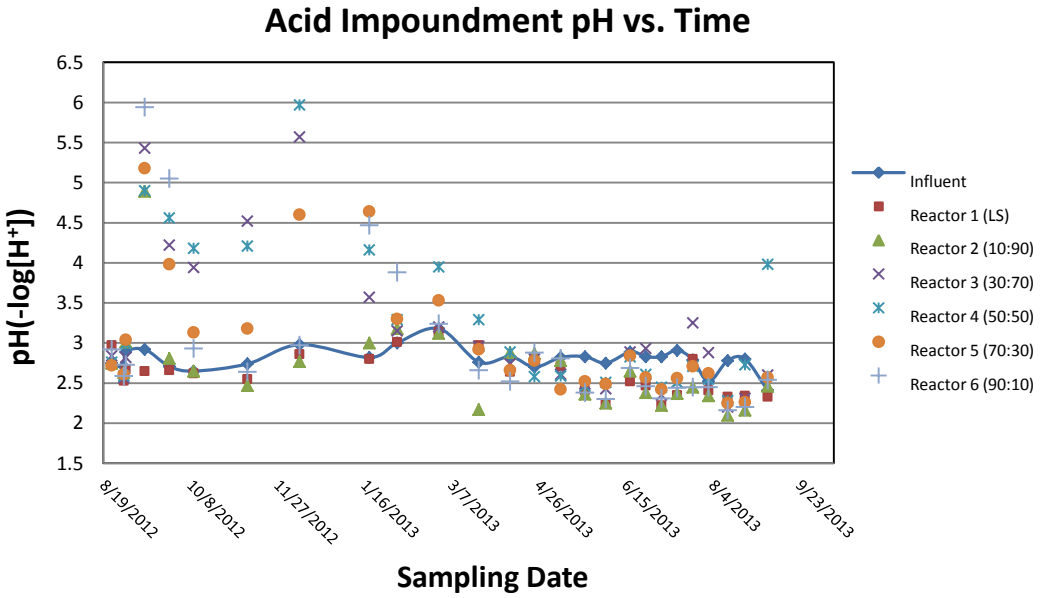

Figure 10: Free proton concentrations (pH) recorded at the AMD influent and acid impoundment of each reactor (R1-R6) during the course of the experiment.

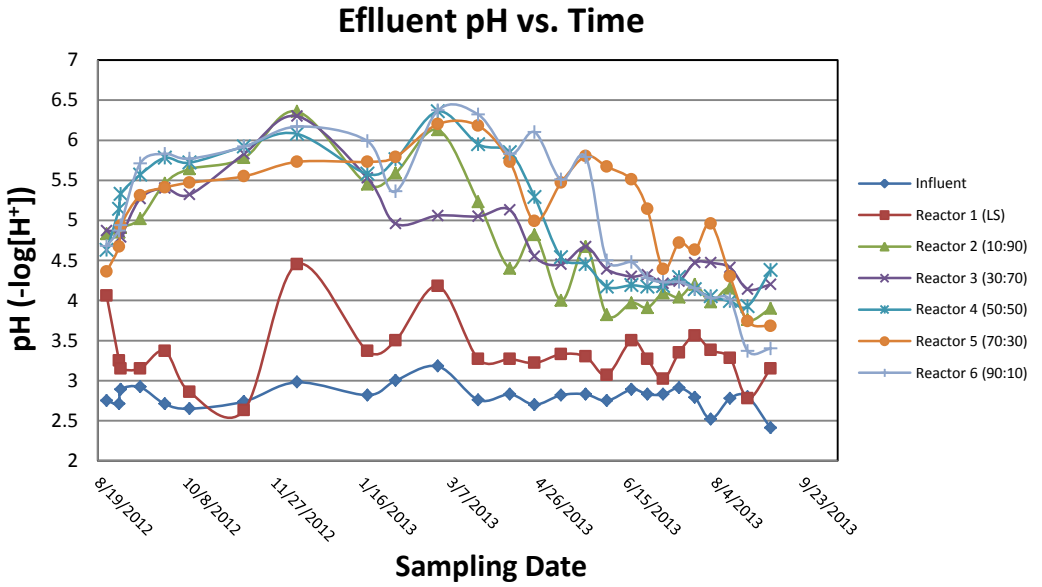

Figure 11: Free proton concentrations (pH) recorded at the AMD influent and effluent of each reactor (R1-R6) during the course of the experiment.

3.1.3 Alkalinity

Total alkalinity was measured in effluent samples that had display pH values greater than 4.5 during field measurement. As a consequence, influent AMD and the effluent of reactor 1 (LS) had never reached pH values over 4.5 and thus were documented as each displaying no titratable alkalinity (Figure 12 & 13).

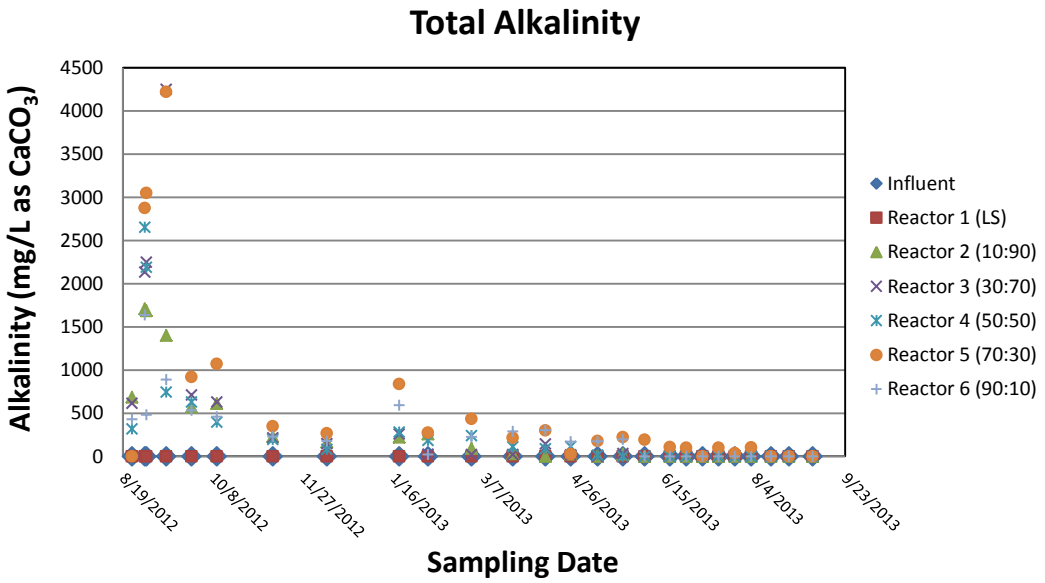

Figure 12: Total alkalinity (mg/L as $CaCO_3$) measured in the effluent of each reactor (R1-R6) during the course of this experiment.

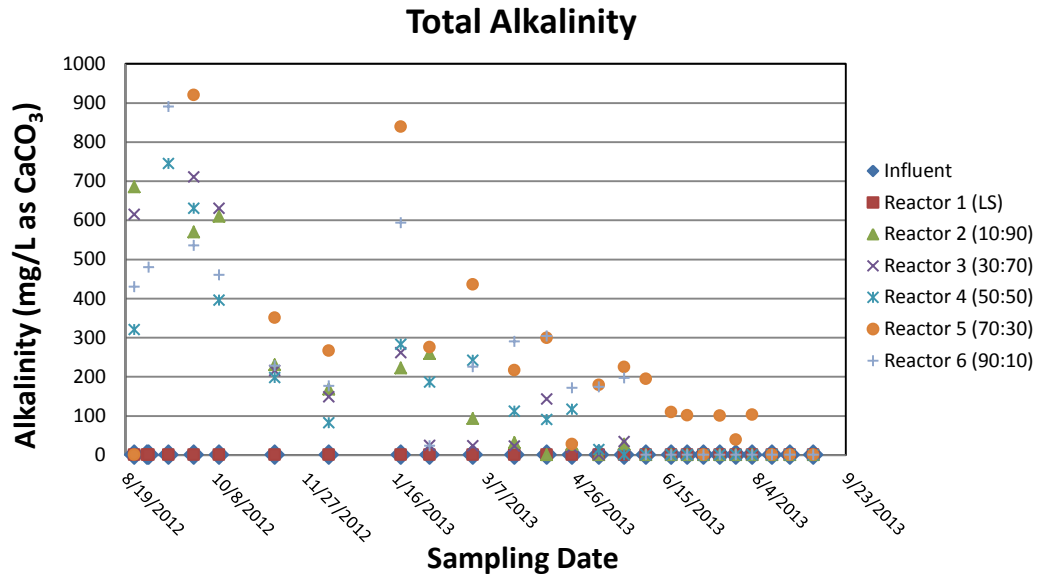

Figure 13: Expended view of total alkalinity (mg/L as CaCO3) measured in the effluent of each reactor (R1-R6) during the course of this experiment. Notice that influent AMD and reactor 1 (limestone only) did not record pH > 4.5 and thus contained no titratable alkalinity.

Within the biologic reactors, a large increase in alkalinity was most pronounced in R3, R4 and R5 with reactors 3 and 4 reaching alkalinity as high as 4,200 mg/L as $CaCO_3$ during the second week. Continued measurements identified that high levels of alkalinity could not be maintained and all reactors had decreased to values below 500 mg/L as $CaCO_3$ by November 2012. From November 2012 to May 2013, notable differences between alkalinity was expressed between each bioreactor as ligneous (R2, R3), 50/50 (R4) and herbaceous (R5, R6) had average alkalinity values of 97, 132 and 275 mg/L as $CaCO_3$, respectively. Furthermore, total alkalinity was only measured in R5 (70:30) after May 2013.

3.1.4 Oxidation-Reduction Potential (ORP)

With respect to the biologic reactors, ORP measurements taken from the effluent port of the limestone control reactor (R1) remained similar to the AMD influent throughout the duration of the experiment (Figure 14). During the initial six months (August, 2012-early February, 2013) the average ORP values measured in the AMD and R1 effluent were 128 and 69mV, respectively. The following months (Late February 2012-September 2013) had recorded average ORP values of 370 mV for the AMD while R1 effluent averaged 300mV. A steady decline in ORP within each bioreactor was measured in the first month of the experiment reaching values below -100 mV, which subsequently leveled off near -139 mV until early December. As the temperatures remained cold the ORP values measured in the bioreactors began to increase near the AMD influent and R1 values averaging -42 mV. In the final months (Late February 2013- September 2013), a decline in ORP values had been recorded reaching values below -100 mV since May 2013. Deviation between ORP values measured between was on average ±19 mV throughout the entire experiment which is greater than the instrument tolerance of ±1 mV.

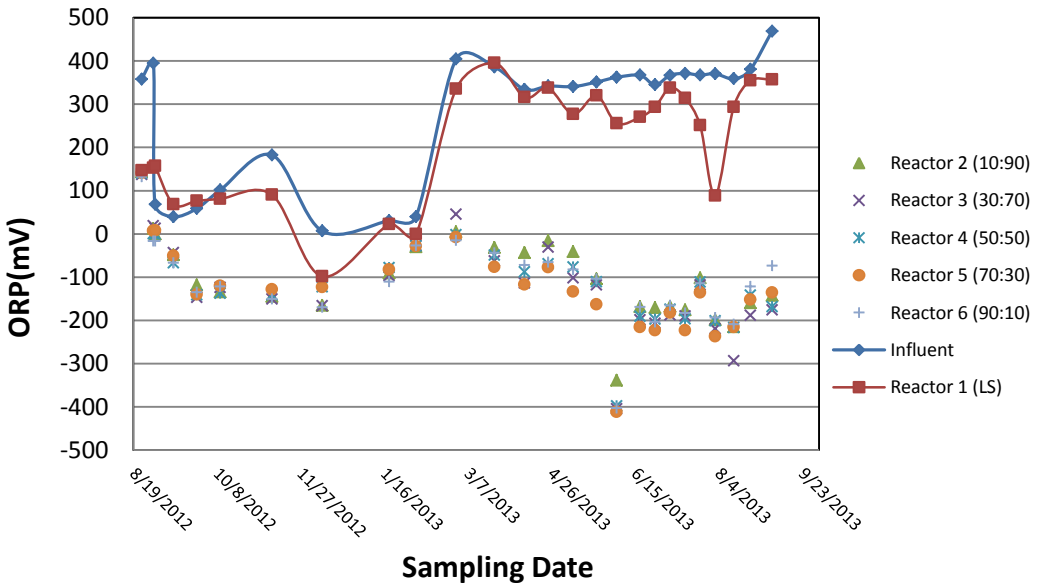

Figure 14: Redox potential of AMD influent and effluents of each reactor throughout the experiment. Redox values were recorded as ORP in millivolts (mV) as described in the instrument methodology.

3.1.5 Dissolved Oxygen

Due to large fluctuations in influent AMD dissolved oxygen (DO) values through time; these values were used as a baseline for comparison of DO measurements made for each reactor. Therefore, Figures 15 & 16 outline the changes in dissolved oxygen (ΔDO) from influent to the simulated acid impoundments (AMD overlying the treatment media within the barrels) and then simulated acid impoundments to effluent, respectively. The following equations were used to derive values obtained for each figure:

$$DO_{(Acid\ Impoundment)} - DO_{(Influent)} = \Delta DO_{(In \rightarrow Al)} \quad \text{(Figure 15)}$$

$$DO_{(Effluent)} - DO_{(Acid\ Impoundment)} = \Delta DO_{(Al \rightarrow Eff)} \quad \text{(Figure 16)}$$

Where $DO_{(Influent)}$, $DO_{(Acid\ Impoundment)}$ and $DO_{(Effluent)}$ represents the absolute dissolved oxygen values in ppm measured at the AMD influent, the reactor's acid impoundment and the reactor's effluent, respectively. Thus, positive ΔDO values represent net increases in DO concentration and negative ΔDO values coincide with net consumption of DO as AMD influent travels to the acid impoundments and then though the treatment media to exit the effluent ports of each reactor. Overall R1 through R6 displayed the same values in $\Delta DO_{(In \rightarrow Al)}$ and $\Delta DO_{(Al \rightarrow Eff)}$ values throughout the entire experiment. During the first two months (August-October 2012) there was an average decrease in DO ($\Delta DO_{(In \rightarrow Al)}$ = -2.71 ppm) measurements from the influent to the acid impoundment of each reactor. The following five months (November 2012-March 2013) displayed an average increase in DO ($\Delta DO_{(In \rightarrow Al)}$ = +3.77ppm) from the influent to the acid impoundments on top of each reactor.

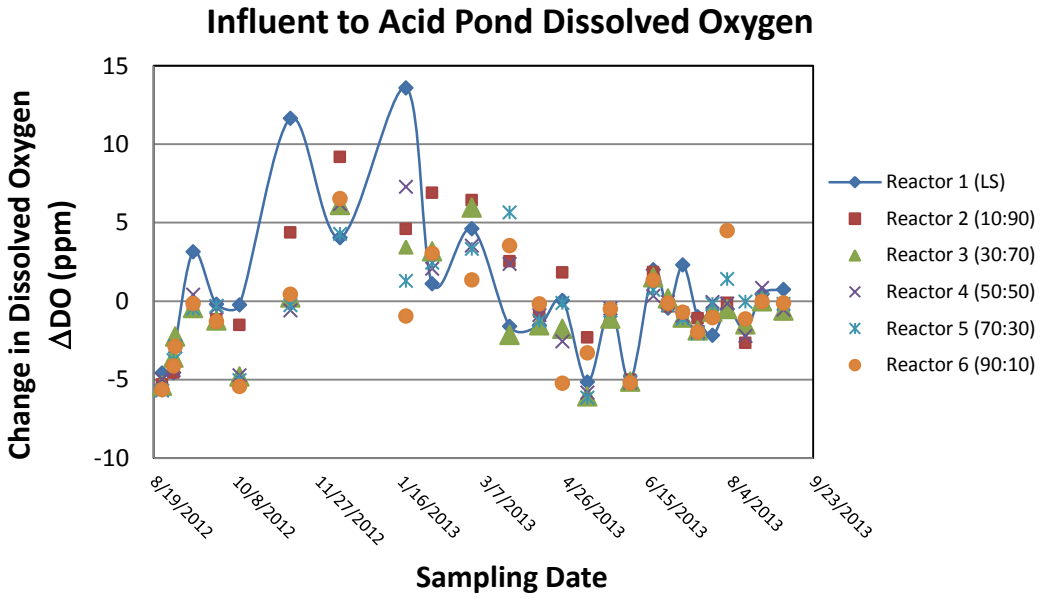

Figure 15: Changes in dissolved oxygen measurements (DO) from influent AMD to the acid impoundments of each reactor (R1-R6). Positive ΔDO correspond to a net increase in DO from influent while negative ΔDO indicates a net decrease.

As for the final months of the experiment (May 2013 – early September 2013) an overall decrease of DO ($\Delta DO_{(In \rightarrow Al)}$ = -1.11ppm) was once again measured. In contrast, during the first

two months (August – October 2012) a slight increase in DO ($\Delta DO_{(AI \rightarrow Eff)}$ = +0.24ppm) was measured on average from the acid impoundments to the effluent ports of each reactor. A striking decrease in DO ($\Delta DO_{(AI \rightarrow Eff)}$ = -7.63ppm) was recorded in the following five months (November 2012-March 2013). Finally, an overall increase in DO ($\Delta DO_{(AI \rightarrow Eff)}$ = +0.87ppm) was measured from the acid impoundment to the effluent port of each reactor in the last experimental months (May 2013 – early September 2013).

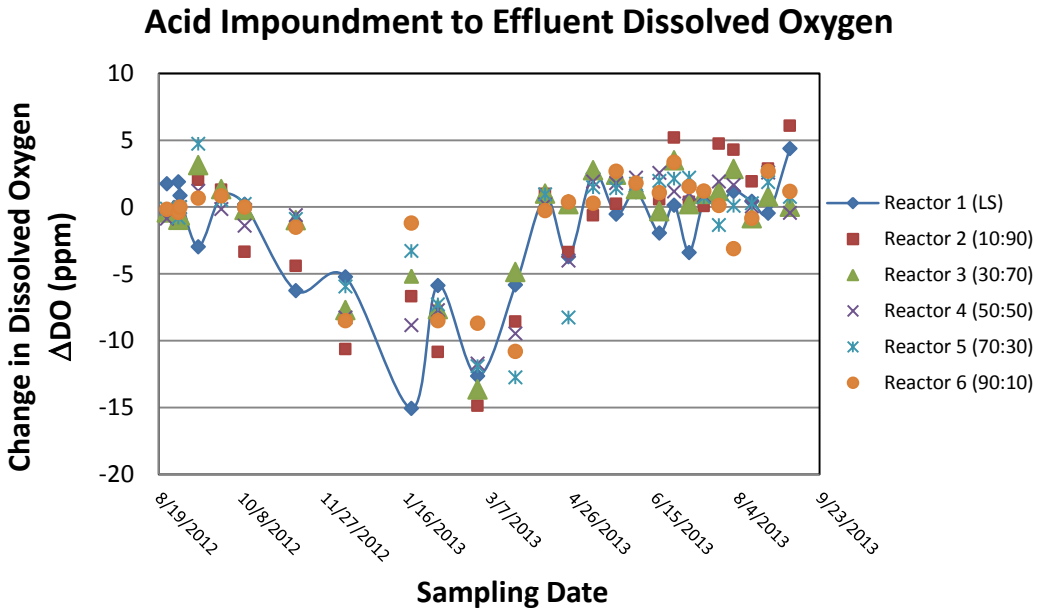

Figure 16: Changes in dissolved oxygen (DO) measurements from the acid impoundment to the respective effluent port of each reactor (R1-R6) as the experiment progressed. Positive ΔDO correspond to a net increase in DO from acid impoundments while negative ΔDO indicates a net decrease.

3.2. Major Anions and Metals

3.2.1 Sulfate

After the initial 24 hours of the experiment percent sulfate removal rates ranged from 27.3 to 55.5% removal with R2 and R1 recording highest removal percentages of 55.5 and 48.9%, respectively. A drop in sulfate removal percent was recorded in all reactors (R1-R6) the following week with an average removal of ~20% (Figure 17). As percent sulfate removal values leveled off near 36±6% in the limestone control (R1), the biologic reactors substantially increased removal percentages and averaged 55±2% removal up to early December 2012.

A decline in removal percentages were recorded January- early February with average removal percentages of 5±0.2% and 19±9% within reactor 1(LS) and the bioreactors, respectively. Subsequent samples collected in the limestone reactor (R1) from late February to early September had shown sulfate removal percentages had average values near 14±7%. Although not as pronounced as removal percentages observed in the earl sampling dates, the bioreactors display a significant increase in sulfate removal from late February when compared to R1(LS). Since late February, average sulfate removal rates in ligneous reactors (R2, R3), 50/50 reactor (R4) and herbaceous reactors (R5, R6) were 21±6%, 19±8% and 28±7%, respectively.

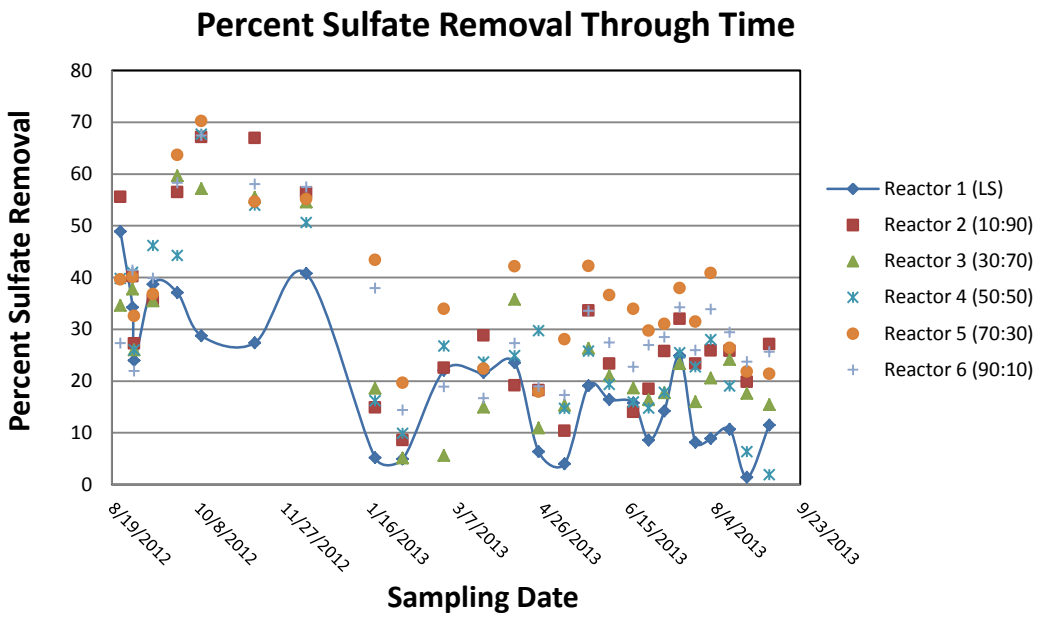

Figure 17: Percent sulfate removal from AMD influent to the effluent port of each reactor (R1-R6) throughout the experiment.

2.2 Sulfide

Dissolved sulfide (S^{2-}) concentrations measured from the influent AMD and reactor 1 (LS) effluent during each sampling event displayed that negligible sulfate reducing processes were occurring within the samples (Figure 18).

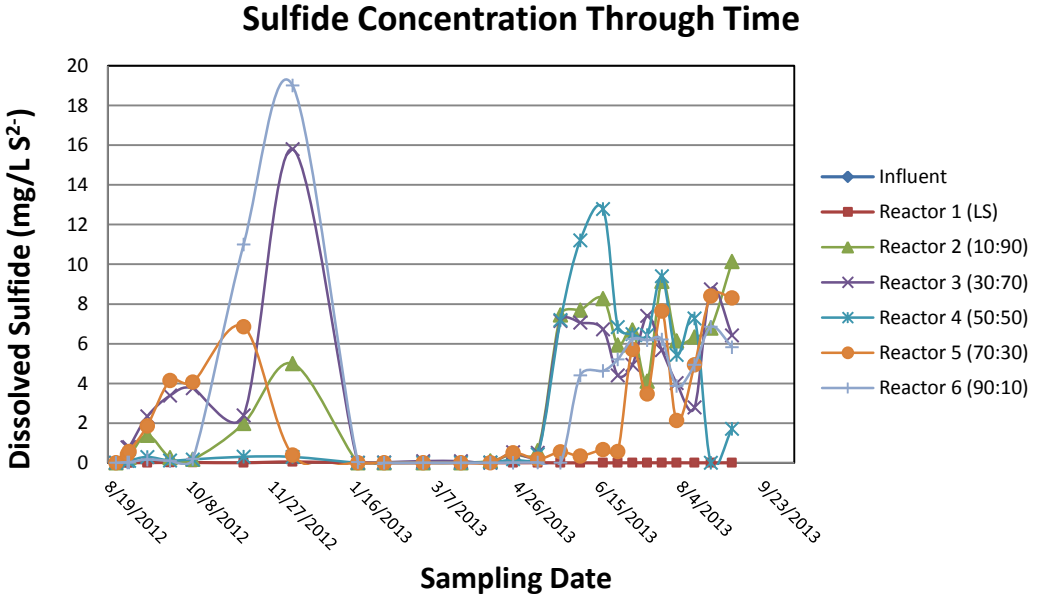

Figure 18: Dissolved sulfide (S^{2-} mg/L) concentrations measured in AMD influent and reactor effluent samples throughout the course of the experiment.

Concentration sensitivity for this method is listed as 5µg/L S^{2-} and of the fifty-two total samples analyzed between the influent AMD and reactor 1 effluent only 5 samples measured sulfide in significant amounts. Of these five samples four were from reactor 1. Overall, average sulfide values determined throughout the experiment for the influent and reactor 1(LS) were documented as 3 and 6 µg/L S^{2-}, respectively. In the biologic reactors sulfide concentrations increased tremendously from August 2012 to December 2012 reaching values as high as 19 mg/L S^{2-} in reactor 6 and averaging a 2.2 mg/L S^{2-} during the early period. An abrupt decline in dissolved sulfide concentrations with in all biologic reactors followed, with an average value of 18 µg/L S^{2-} measured between January 2013 and early April 2013. Then another peak in sulfide concentrations was recorded in the biologic reactors, together averaging 4.9 mg/L S^{2-} from late April 2013 to September 2013.

3.2.3 Iron

Influent AMD dissolved iron concentrations were documented as being relatively consistent with the average iron concentration of 908±123 mg/L total dissolved Fe (Fe_T) recorded over the duration of the experiment. Figure 19 displays the percent iron removal in each reactor with respect to the incoming AMD influent iron values. All reactors display large variations in removal percentages through the entire experiment along with little distinction between the limestone control (R1) and the biologic reactors (R2-R6). Percent iron removal from August 2012 – December 2012 averaged 68±3% within all six reactors.

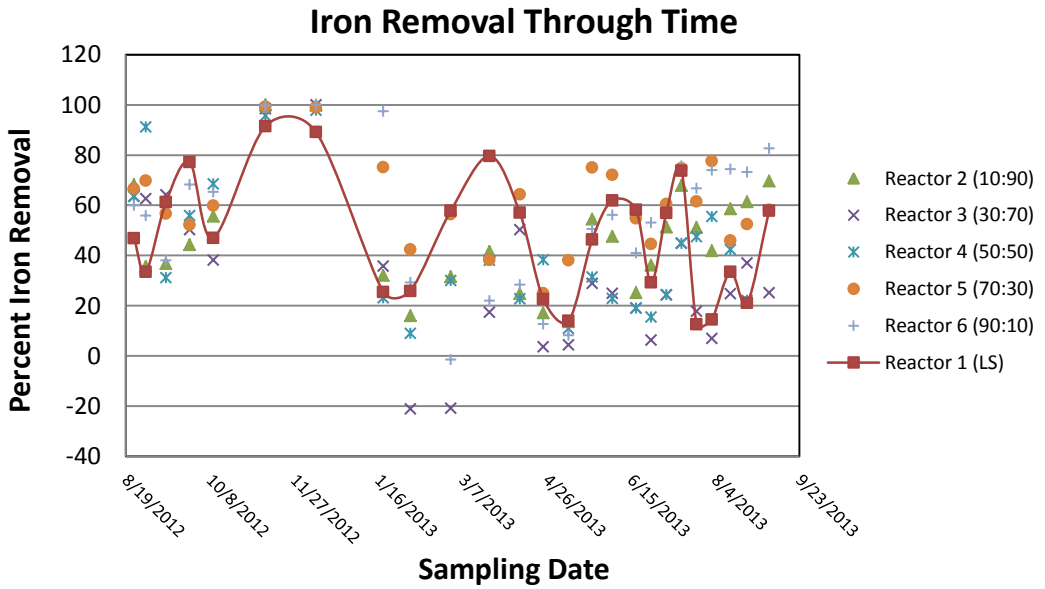

Figure 19: Percent iron removal from AMD influent to reactor effluent (R1-R6) as the experiment progressed with time.

A dramatic decrease in removal percentage was observed in reactors 1-4 as removal percentages dropped near 30%. A net increase in iron was then detected in reactor 3 and 6 during the month of February 2013. From March 2013 to September 2013 removal percentages were highly variable in all reactors and an overall removal of 41±13% was determined for all

reactors during this time. Computing average removal percentages throughout the entire experiment and grouping reactors by composition it was determined that limestone only (R1), ligneous (R2, R3), 50/50 (R4) and herbaceous reactors (R5, R6) achieved removal percentages of 45%, 38%, 40% and 55%, accordingly.

3.2.4 Aluminum

Dissolved aluminum concentrations measured in the influent AMD averaged 198 ± 26mg/L Al^{3+} throughout the course of the entire experiment. As for the limestone reactor (R1) effluent, the aluminum concentrations averaged 122 ± 39mg/L Al^{3+} which corresponded to an average removal of 37% from the influent AMD. Reactor 1 recorded its lowest aluminum concentration during December 10, 2012 with values reaching 12.3mg/L Al^{3+} (Figure 20). Much lower aluminum concentrations were recorded in the samples taken from the simulated bioreactor effluent.

Specifically, throughout the entire experiment average concentrations of 31.7, 32.0 and 17.5 mg/L Al^{3+} were measured in the ligneous (R2, R3), 50/50 mix (R4) and herbaceous (R5, R6) reactors, respectively. Overall the bioreactors (R2-R6) displayed an immediate drop in aluminum concentrations during the first week, a trend which for the most part continued for roughly eight months.

During late April 2013, effluent samples taken from the ligneous reactors (R2,R3) began to increase in aluminum concentrations once again but did not reach values higher than those measured in reactor 1 (LS). Increases in aluminum concentrations were subsequently exhibited during the following months in reactor 4(50:50) and then reactor 6 (90:10). Finally reactor 5 (70:30) displayed a significant increase during mid-august 2013 yet was not as pronounced as the other reactors.

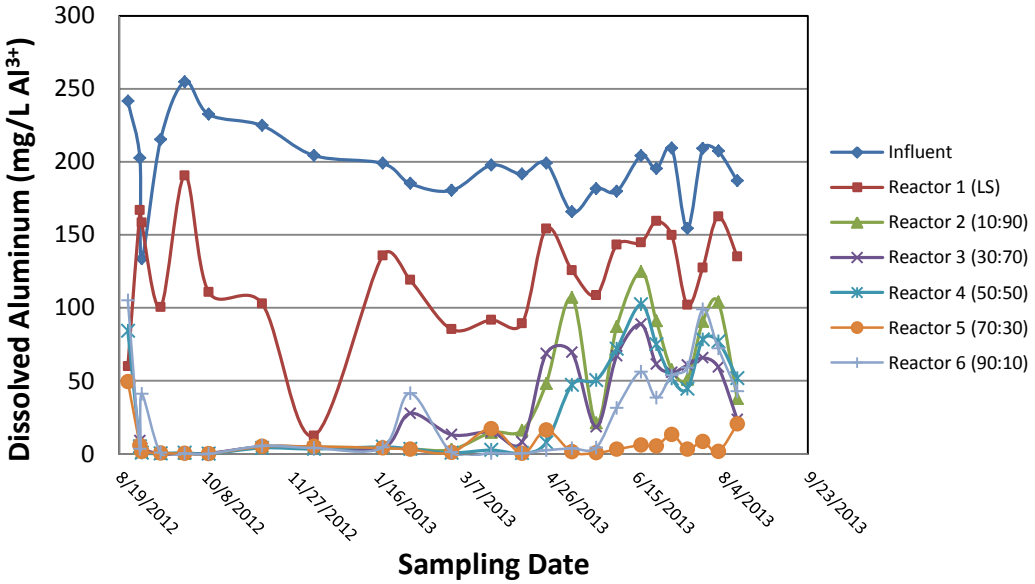

Figure 20: Plot showing the dissolved aluminum concentrations (mg/L Al^{3+}) in samples taken from the AMD influent and reactor effluent ports (R1-R2) during the course of the experiment.

3.2.5 Manganese

Manganese concentrations measured at the influent AMD port ranged from 35-52 mg/L Mn^{2+} with an average concentration and standard deviation of 43±4mg/L Mn^{2+}. Initial manganese removal percentages in the limestone reactor (R1) were negligible and showed similar concentrations to the influent manganese from August 2012 – October 2012 (Figure 21). As for the biologic reactors, a net increase in manganese relative to the influent drainage was detected during the initial week. Then manganese increases within the bioreactors quickly subsided and manganese removal ranging from 9-32% was observed in late September 2012-early October 2012.

During the following two months (November 2012 – December 2012), manganese removal became significant in the limestone reactor reaching 16% average manganese removal between the two months. This removal coincides with the high iron removal (i.e. 90%) also observed in the limestone reactor during these months. Still, manganese removal was even greater in the bioreactors during these months (November 2012 – December 2012) with up 59% removal and an average removal of 33%. As the reactors began to experience prolonged periods of cold temperatures another release of manganese was documented through January 2013 – February 2013.

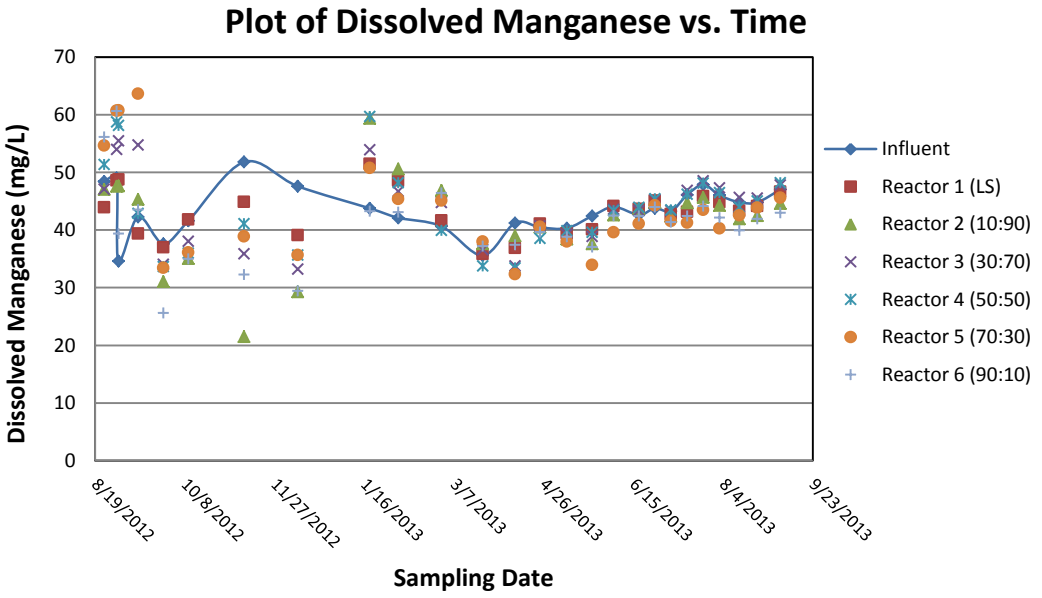

Figure 21 Plot of dissolved manganese (mg/L Mn^{2+}) measured within the AMD influent and reactor (R1-R6) effluents over the course of the experiment.

During these months an average release of 12%, 19%, 16% and 8% manganese was documented in the limestone reactor (R1), ligneous reactors (R2, R3), 50/50 reactor (R4) and herbaceous reactors (R5, R6), respectively. As manganese measurements continued from March 2013 to September 2013 minimal removal percentages were recorded in all reactors. However, the herbaceous reactors (R5, R6) showed the greatest Mn^{2+} retention, together averaging 6% removal through the final six months.

3.2.6 Calcium

Influent drainage flowing into each reactor contained on average 144±37mg/L of dissolved calcium that was observed throughout the duration of the experiment. Effluent drainage of the limestone reactor averaged 275±96mg/L Ca^{2+} with the maximum concentration of 531mg/L measured the first twenty-four hours after it actively received AMD.

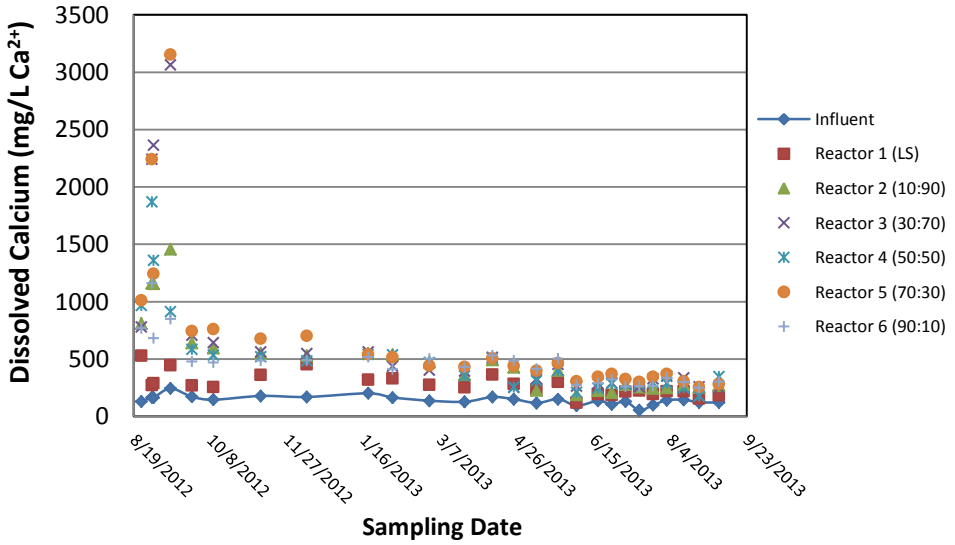

Figure 22 Calcium concentrations measured in samples taken from the AMD influent and effluent port of each reactor (R1-R6) as the experiment progressed.

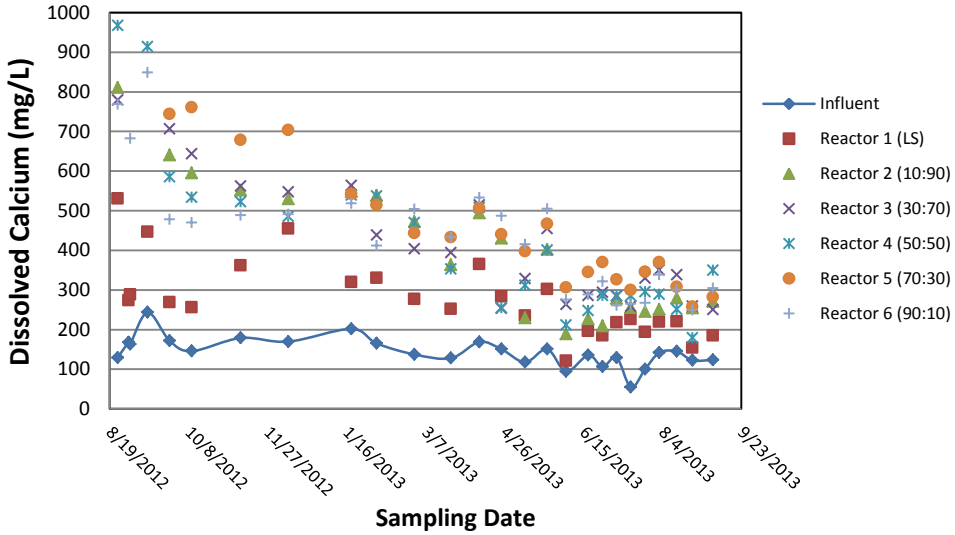

Figure 23 Expanded view of calcium concentrations measured in samples taken from the AMD influent and effluent port of each reactor (R1-R6) as the experiment progressed.

As for the bioreactors, trends were similar to alkalinity measurements as initial calcium concentrations increased tremendously within the first two weeks reaching values up to 3,153 mg/L Ca^{2+} (Figure 22). Such pronounced increases in calcium were short-lived as all bioreactors dropped below 800 mg/L Ca^{2+} after one month (Figure 23).

Relative to the limestone reactor (R1), the biologic reactors exhibited calcium concentrations substantially greater throughout the entire experiment. Still a steady decline in Ca^{2+} values were observed in all bioreactors (R2-R6) as a function of increasing time and have all dropped below 400mg/L Ca^{2+}. Additionally, although extremely high calcium were not observed within the limestone reactor (R1) there had been a consistent increase in Ca^{2+} for the duration of the experiment.

3.2.7 Magnesium

Magnesium values measured in the influent AMD were highly consistent over the 377 day experiment with values averaging near 210±16 mg/L Mg^{2+}. Reactor 1 (LS) magnesium concentration values were similar to those of influent, averaging 238±20mg/L Mg^{2+} for the duration of the experiment (Figure 24). However, on sporadic occasions noticeable increases in magnesium were documented in the effluent of reactor 1 (LS).

Within the effluent of the biologic reactors high magnesium concentrations were determined during the initial two weeks of operation reaching values up to 461mg/L Mg^{2+}. In contrast to trends in calcium concentrations, after the initial two weeks magnesium values in the bioreactor effluents (R2-R6) were observed as being similar to that of the limestone effluent (R1). From 9/26/2012 to 9/5/2013 magnesium concentrations averaged 237±19, 236±27, 233±22, 230±27, 237±27 and 231±27 for R1, R2, R3, R4, R5, and R6, respectively. Therefore, from late September 2012 to early September 2013 on average all reactors (R1-R6) increased magnesium concentrations of the influent AMD by roughly 26mg/L Mg^{2+}.

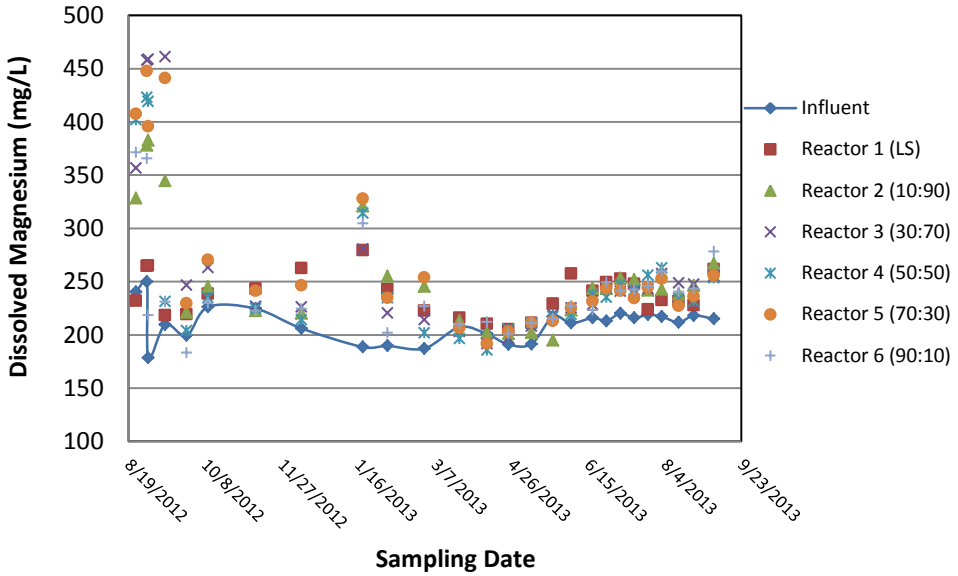

Figure 24 Magnesium concentrations (mg/L Mg^{2+}) measured in the AMD influent and effluent samples of each reactor (R1-R6) during each sampling event.

3.2.8 Chloride

Concentrations of chloride in the influent AMD drainage were relatively consistent with values averaging 14 mg/L Cl^- during the course of the experiment.

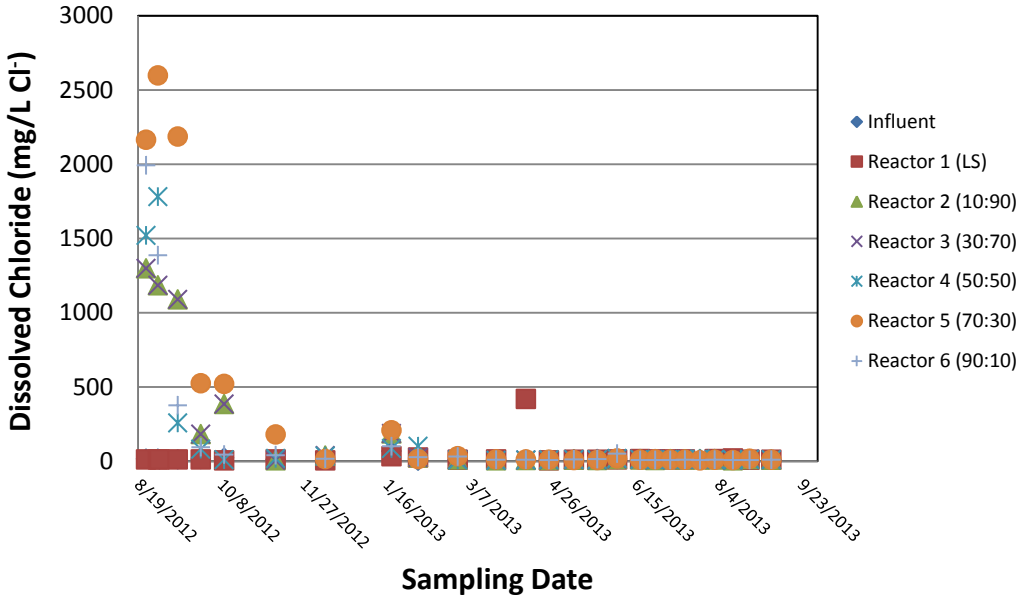

Figure 25 Measured chloride concentrations (mg/L Cl^-) of the AMD influent and the effluent of each reactor (R1-R6) for each sampling event.

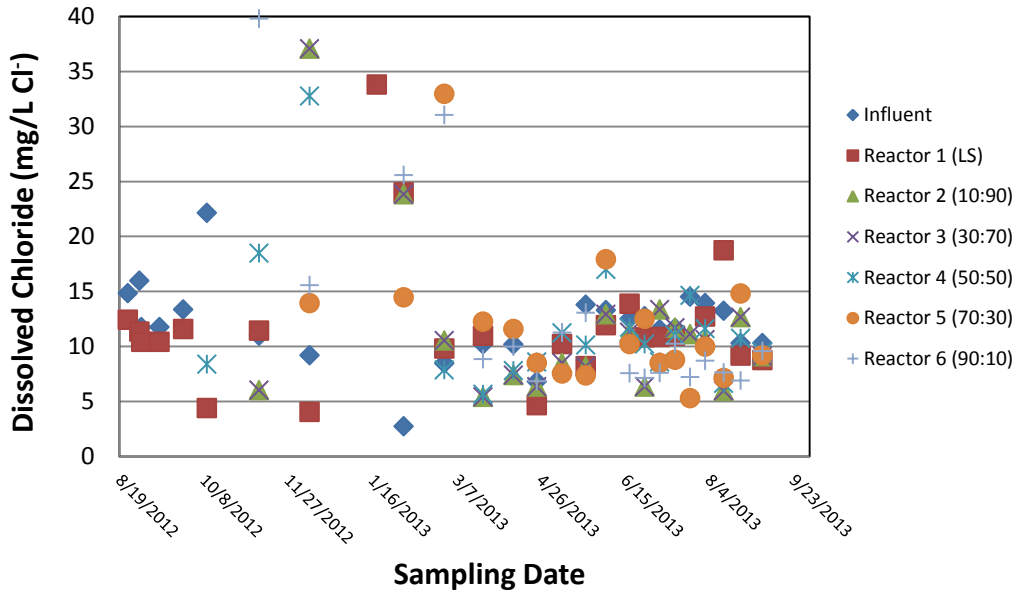

Figure 26 Expanded view of the measured chloride concentrations (mg/L Cl^-) of the AMD influent and effluent of each reactor (R1-R6) for each sampling event.

Aside from a few spikes in chloride concentrations, the limestone reactor exhibited similar values with respect to the AMD influent (Figure 25). Still, due to the high concentrations of these documented peaks in chloride the limestone only reactor (R1) average 37mg/L chloride over the course of the experiment. Chloride concentrations within the bioreactors (R2-R6) can be separated in three events high concentration, medium concentrations and concentrations near influent AMD.

During the first two months average chloride concentrations ranged from 730-1675 mg/L Cl^- with maximum values over 2500 mg/L Cl^-. Subsequent declines in chloride values occurred during the following four months (November 2012- February 2012) and average concentrations ranged between 42-90 mg/L Cl^-. Lastly, during the final six months of the experiment chloride values measured in the samples taken for the effluent of each bioreactor (R2-R6) fell below the average AMD influent values with average concentrations ranging from 9.4-11.5mg/L Cl^- (Figure 26).

3.2.9 Fluoride

Influent fluoride concentrations over the course of this experiment were documented as having large relative fluctuations with average values and standard deviation of 13 ± 7mg/L F^-. As for the effluent samples taken from limestone reactor significant removal was documented from the influent AMD in which values averaged 9 ± 4mg/L F^- throughout the entire experiment.

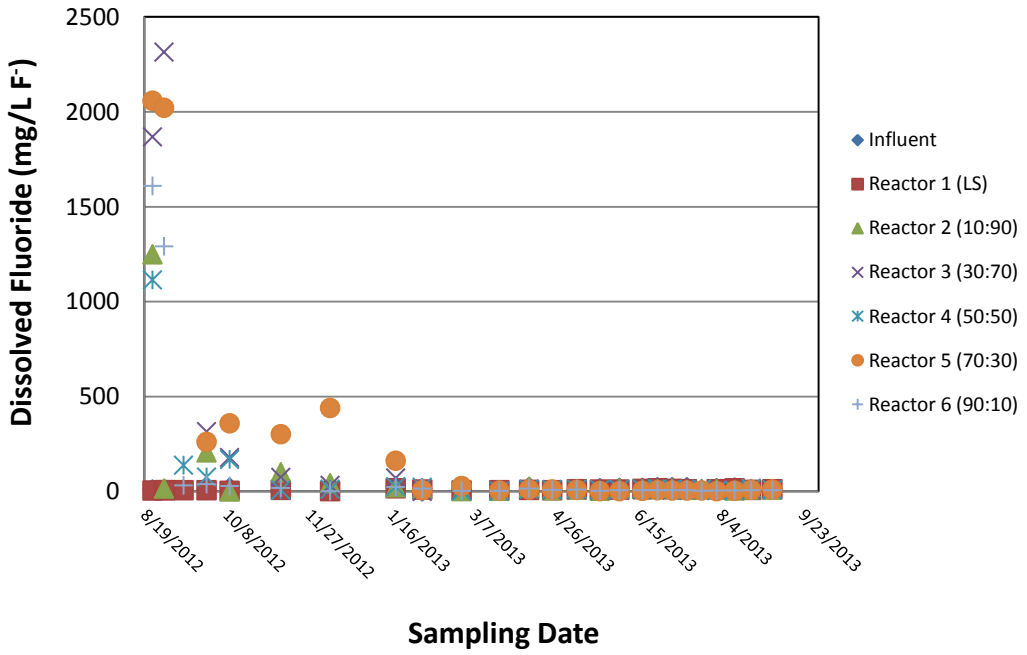

Figure 27: Fluoride values measured in samples taken from influent AMD and effluent ports of all reactors (R1-R6) during the course of this experiment.

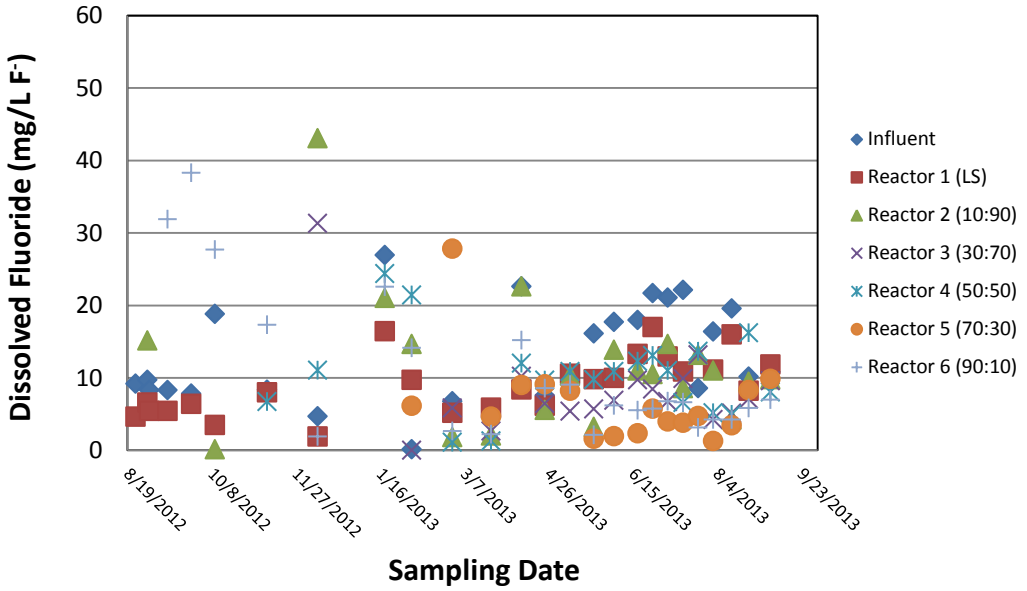

Figure 28: Expanded View of Fluoride values measured in samples taken from influent AMD and effluent ports of all reactors (R1-R6) during the course of this experiment.

In the case of the bioreactors (R2-R6) spikes in fluoride concentrations had also showed a transition from high, medium and low as was documented for chloride values (Figure 27). Within the first two months of operation average fluoride concentrations recorded in the effluent samples taken from the bioreactors (R2-R6) ranged between 367-1,175 mg/L F. During the next four months (November 2012 – February 2013) average fluoride values dropped substantially with in each bioreactor (R2-R6) effluent, ranging from 12 to 187 mg/L F^-. Throughout the final six months (March 2013 - early September 2013), effluent fluoride concentrations of the bioreactors (R2-R6) had dropped below average AMD influent values ranging from 5-10 mg/L F^- (Figure 28).

3. 3. Trace Metals

3.3.1 Nickel

Nickel measurements performed throughout the experiment identified average influent concentrations of 2.05±0.57 mg/L Ni^{2+} with a significant fluctuation (28% relative standard deviation) observed for concentrations of this trace metal. Removal of nickel in the limestone reactor (R1) was extremely negligible and in multiple cases a rise in concentration was observed (Figure 29). Of the samples collected for Reactor 1 an average of 2.16±0.66 mg/L $Ni^{2+}$was measured which corresponds to an overall 7.3% increase from the influent drainage. In contrast, the biologic reactors (R2-R6) displayed successful removal of nickel throughout the experiment reaching values below detection (LOD = 10 ppb) in many instances. Initially nickel concentrations slowly declined reaching an average of 1.23 mg/L Ni^{2+} within the bioreactors (R2-R6) by the end of the second week. Next, large decreases of nickel concentration were observed accounting for an average of 96.2% removal within the bioreactors from 9/26/2012 to 12/10/2012. Although remaining effective in nickel removal the degree of removal began to slowly decline in the final seven months. However, overall the removal percent during these

months remained extremely high relative to the limestone control reactor averaging 81.2% between the biologic reactors.

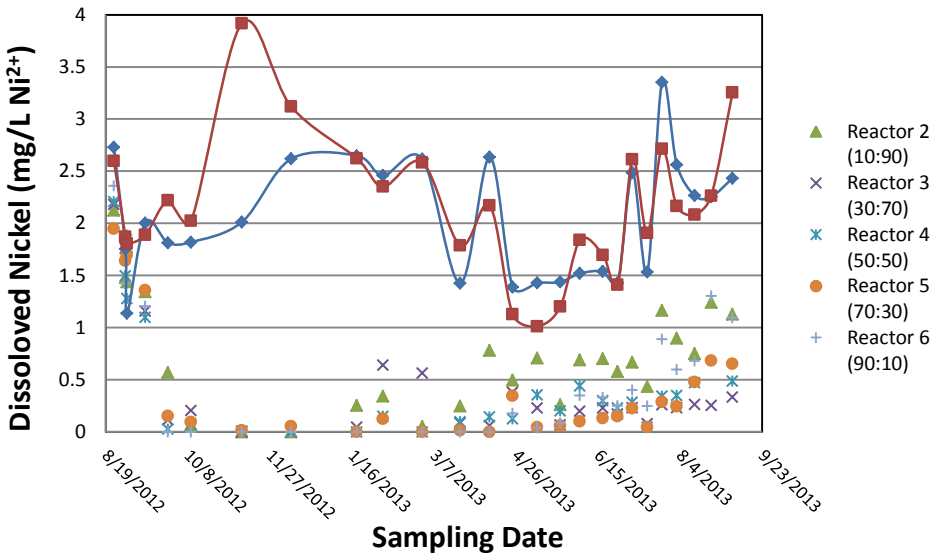

Figure 29 Dissolved nickel concentrations (mg/L Ni^{2+}) measured in the AMD influent and effluent of each reactor (R1-R6) for each sampling event.

3.3.2 Zinc

Influent AMD zinc values averaged 3.35±0.34 mg/L during the experiment and had less variability (RSD = 10%) when compared to nickel concentrations.

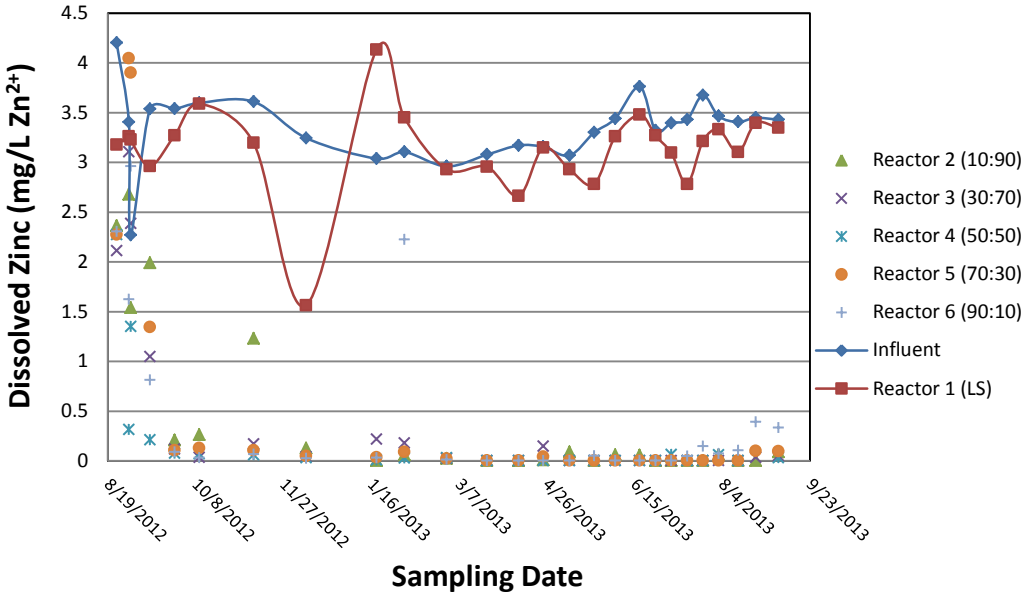

Figure 30 Measured zinc concentrations (mg/L Zn^{2+}) within the influent AMD and reactor effluents (R1-R6) over the course of the experiment.

A slight decrease in zinc was found in the majority of effluent samples analyzed from Reactor 1 which corresponded to a 5.4% average zinc removal overall. In Figure 30, a dramatic removal of 52% zinc was documented in Reactor 1 December 2012 followed by a 36% and 11% increase in zinc concentrations on January and February 2013, respectively. Biologic reactors (R2-R6) were found do exceptionally well in terms of zinc attenuation. During the first two weeks removal percentages varied immensely between the bioreactors as output concentrations ranged from 0.2-4.2 mg/L Zn^{2+}. After a month of actively receiving AMD the biologic reactors (R2-R6) had all reached effluent zinc concentrations well below 0.5 mg/L Zn^{2+} (Figure 31). Apart from two samples taken from R2 (11/10/12) and R6 (2/4/13), zinc concentrations within all bioreactors remained near or below detection limit (LOD = 5 ppb) for the majority of the experiment.

3.3.3 Cadmium

Aside from a large spike on 9/26/12, cadmium concentrations in the influent AMD remained relatively stable for the duration of the project and averaging 19.5±6 µg/L Cd^{2+} (Figure 31). Reactor 1 (LS) effluent Cd was removed at varying degrees of success with no appreciable net release of cadmium as observed for both nickel and zinc. Overall an average of 14.3±3 µg/L Cd was documented from the effluent of R1 (LS) corresponding to an average of 27% cadmium removal. As for the bioreactors (R2-R6), cadmium levels had reach values below the detection limit (LOD = 3 µg/L) a month after the experiment began. Additionally cadmium concentrations remained below 5 µg/L with most samples containing no detectable cadmium for the throughout the rest of the experiment.

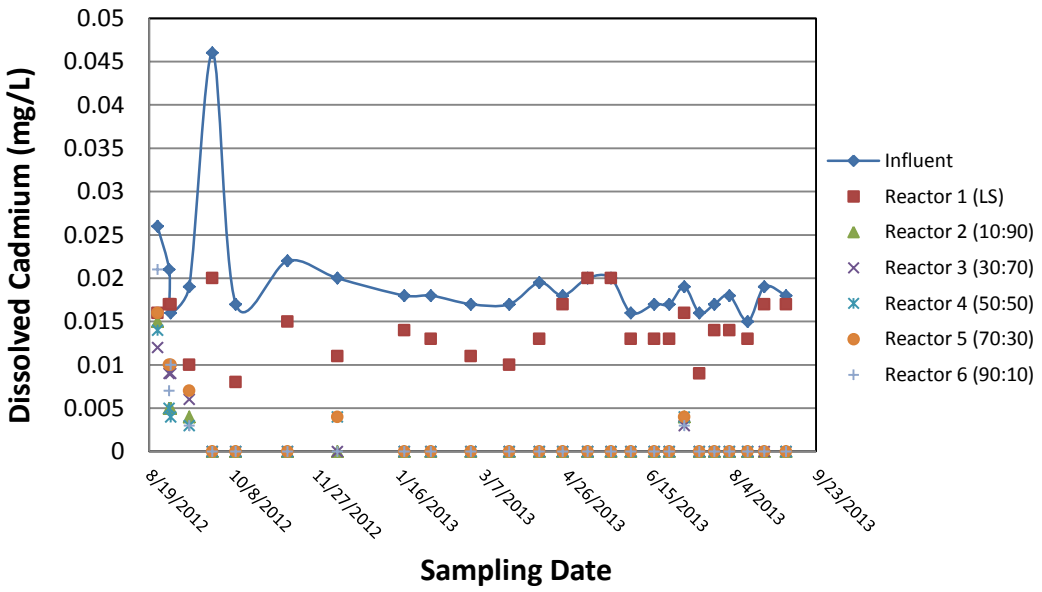

Figure 31: Influent AMD and reactor effluent (R1-R6) cadmium concentrations (mg/L Cd^{2+}) determined for each sampling event.

3.3.4 Copper

Dissolved copper concentrations in the AMD influent displayed large relative fluctuations with an average value and standard deviation of 0.037 ± 0.015mg/L Cu^{2+} overall.

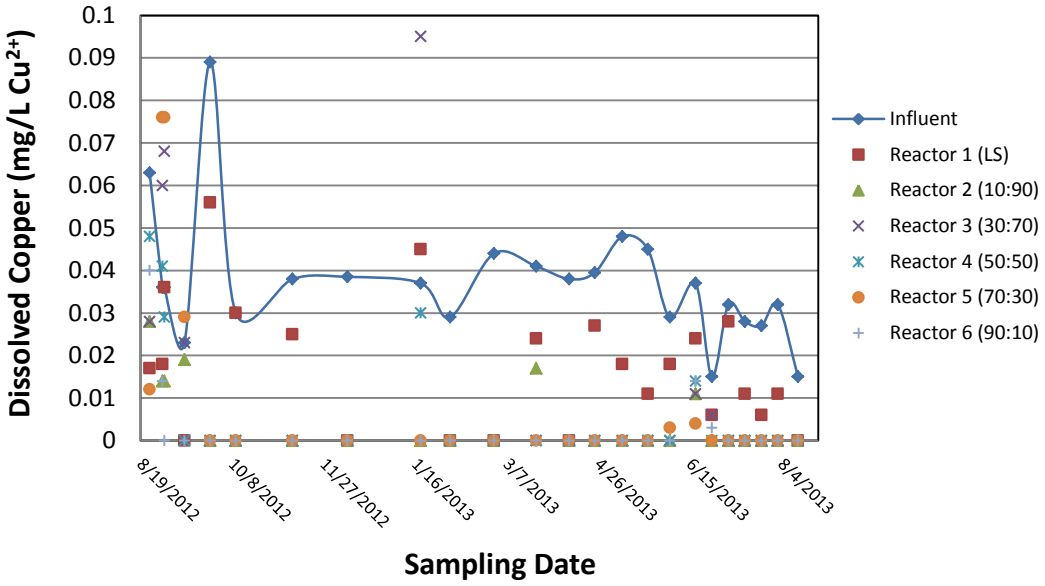

Figure 32: Measured copper values (mg/L Cu^{2+}) within the AMD influent and effluents of all reactors (R1-R6) over the course of the experiment.

Significant removal of copper was exhibited in the limestone only reactor (R1) as an average of 0.017mg/L Cu^{2+} was recorded in the effluent which corresponded to 53.8% removal. In the biologic reactors (R2-R6) copper values dropped below detection (LOD = 3 µg/L) within the first month of operation. This trend continued for all biologic reactors (R2-R6) for the majority of the experiment (Figure 32). However, two large spikes in copper values during were recorded in January 2013 reaching values of 0.095 and 0.030 mg/L Cu^{2+} within Reactor 3 (30:70) and Reactor 4 (50:50), respectively. Still high copper removal percentages were characteristic of the bioreactors (R2-R6) with average removal percentages ranging from 67-92% throughout.

3.3.5 Strontium

Dissolved strontium concentrations in the influent drainage were mostly below detection limit (LOD = 10 mg/L) yet on occasions reached levels near 0.1 mg/L Sr^{2+}. On the other hand strontium increases in all reactor effluent with, for example, values increasing by two orders of magnitude in early effluent samples taken from R3 and R5 recording 13.5 and 11.1 mg/L Sr^{2+}, respectively (Figure 33). Strontium concentrations fell below 4 mg/L after a month of operation and continued to slowly decline throughout the experiment. Reactor 1 (LS) effluent displayed relatively low amounts of dissolved strontium when compared to the biologic reactors yet was still significantly higher than influent levels (Figure 35). Throughout the entire experiment average strontium outputs was recorded as 0.5 mg/L Sr^{2+} in the limestone only reactor (R1), 1.5 mg/L for the ligneous reactors (R2, R3), 1.2 mg/L in 50/50 reactor (R4) and 1.4 mg/L strontium in the herbaceous reactors (R5, R6).

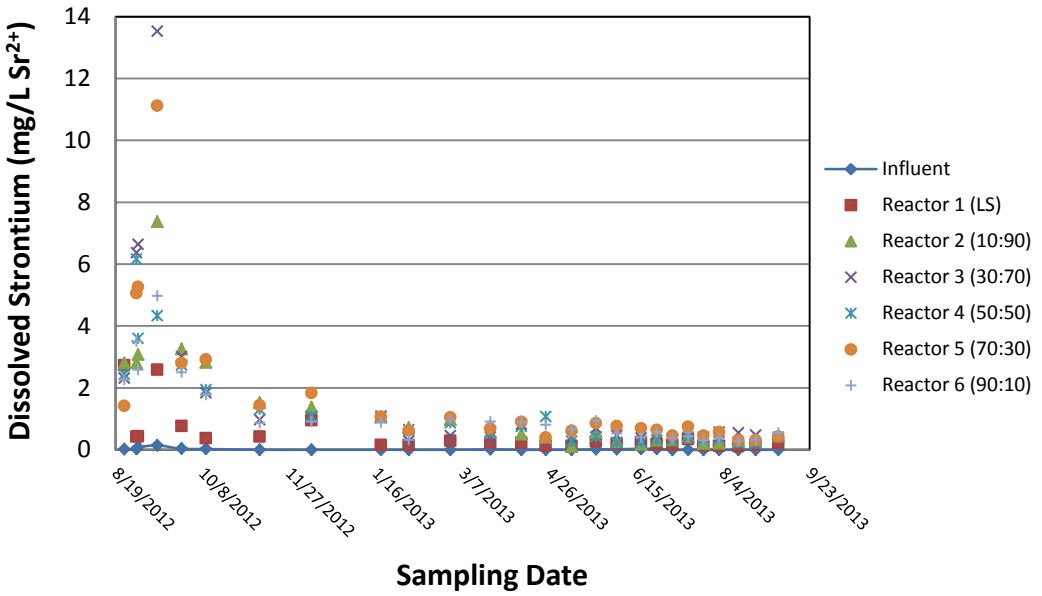

Figure 33: Strontium concentrations (mg/L Sr^{2+}mg/L) detected in AMD influent and reactor effluents (R1-R6) at each sampling event.

3.3.6 Potassium

Influent AMD potassium concentrations remained relatively consistent throughout the course of the experiment and averaged 7.4 ± 1.6mg/L K^{+} overall.

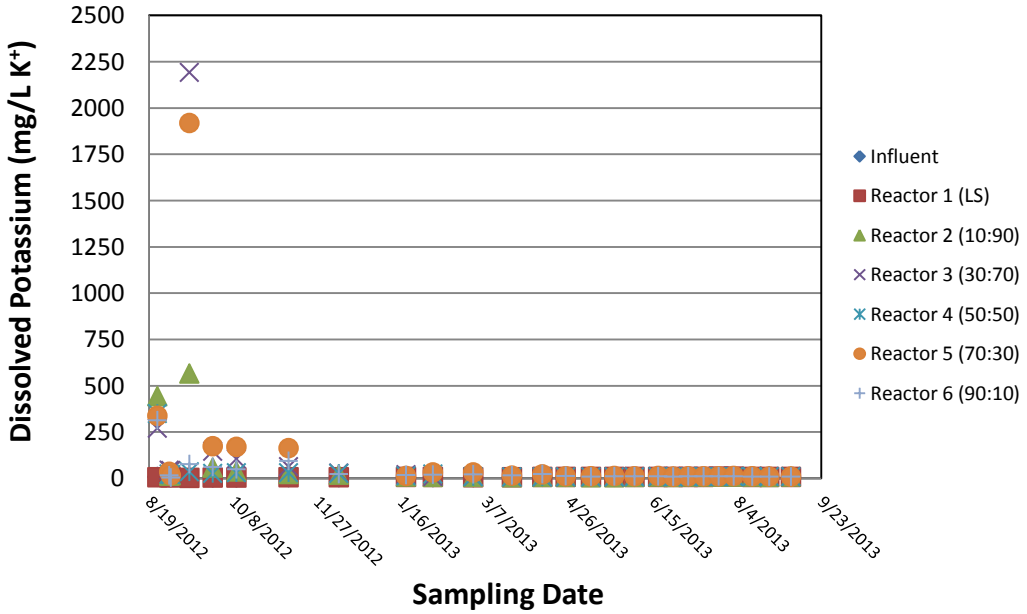

Figure 34: Measured potassium of influent AMD and each reactor effluent (R1-R6) throughout the entire experiment.

A minor removal of potassium was documented in the effluent of the limestone only (R1) reactor averaging 7.2 ± 1.5 mg/L K^+ throughout. Again the bioreactors (R2-R6) displayed distinct transitions in potassium measurements in which values went from high to medium and low concentrations during the experiment.

Potassium content was high throughout the initial two months as the average values recoded from all bioreactor effluents ranged from 81-442 mg/L K^+ (Figure 34). Over the following four months (November 2012- February 2013) potassium concentrations declined in all five bioreactor (R2-R6) effluent drainages as average values ranged between 8.5-12.3 mg/L K^+. Still, during the final month's bioreactor (R2-R6) potassium concentrations remained above the recorded influent values indicating a net release of potassium continued throughout the majority of the experiment.

3.3.7 Sodium

Dissolved sodium concentrations measured in the influent drainage maintained an average of 35 mg/L Na^+ throughout the experiment. Effluent measurements for Reactor 1 (LS) exhibited a subtle decline in sodium concentrations during active treatment as the calculated average was 32 mg/L Na^+ for this test cell.

Again the bioreactors (R2-R6) displayed an evolution from high to medium and low sodium concentrations as time progressed. Initially within the bioreactors (R2-R6), average measurements ranged from 41-137 mg/L Na^+ until October 2012 (Figure 35). Then during the next four months (November 2012-February 2013) average values decreased within the bioreactor effluents with concentrations ranging from 32-55 mg/L Na^+. All bioreactor sodium values then dropped near the AMD influent concentrations and averaged 32 mg/L Na^+ in the final six months (Figure 38).

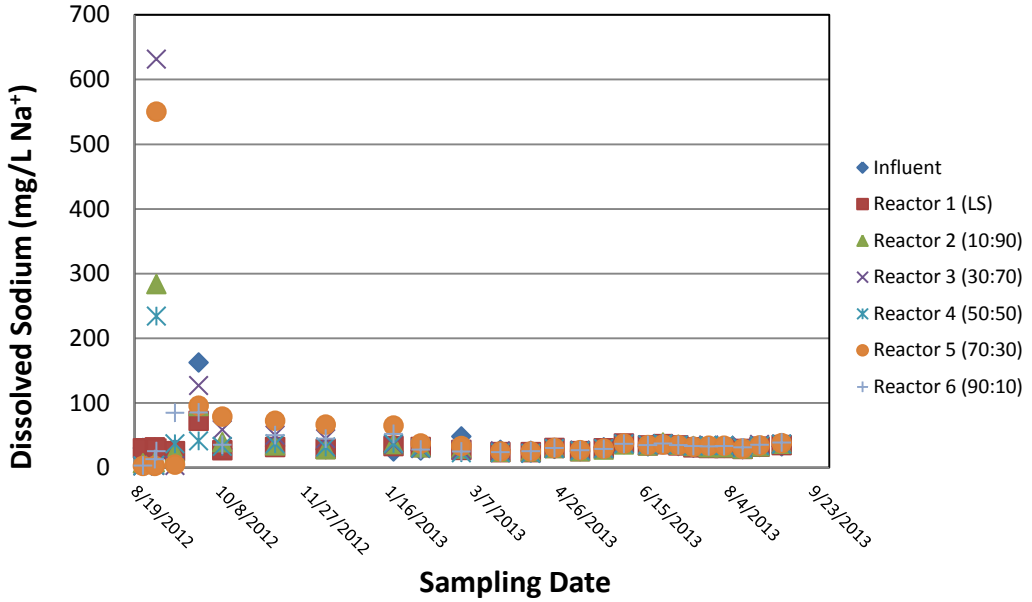

Figure 35: Measured sodium values (mg/L Na^+) in the AMD influent and effluent samples of each reactor (R1-R6) during the course of the experiment.

4. Discussion

During the duration of these experiments, each reactor actively received AMD at an average rate of ~5 mL/min directly from the main seep at the Tab-Simco AML site. Throughout the experiment the influent AMD was consistently composed of acidic waters with pH values between 2.3 and 3.1 and with high concentrations (mg/L) of dissolved constituents: 900 Fe_T, 200 Al, 40 Mn and 5,000 SO_4^{2-} along with significant amounts of trace elements (Figures 30-33). Although daily precipitation events as much as 6.73 cm (2.65'') in the area caused diel physicochemical fluctuations (i.e. contaminant plumes, AMD dilution) in species concentrations they were short-lived and of minor significance when compared to the long-term geochemical trends. Local temperatures ranged from -13 to +35°C (8 to 96°F) and were linked to playing a substantial role in controlling the efficacy of the sulfate reduction within bioreactor test cells because microbial sulfate reduction rates are much lower at lower temperature.

4.1 Temperature Effects on ASBR Technology

Reactor outflow temperatures recorded in the field closely resembled that of the average local air temperatures (Figure 9) and dramatically disrupted biologic activity during the winter season. As mentioned earlier the partitioning of gaseous oxygen into the aqueous phase was documented as displaying a cyclical trend within the acid impoundment of all reactors (Figure 15). Specifically, the influent AMD to each reactor acid impoundment (AI) initial depletion of dissolved oxygen (DO) transgressed to increases in DO and then displayed a rebound to DO depletion with time.

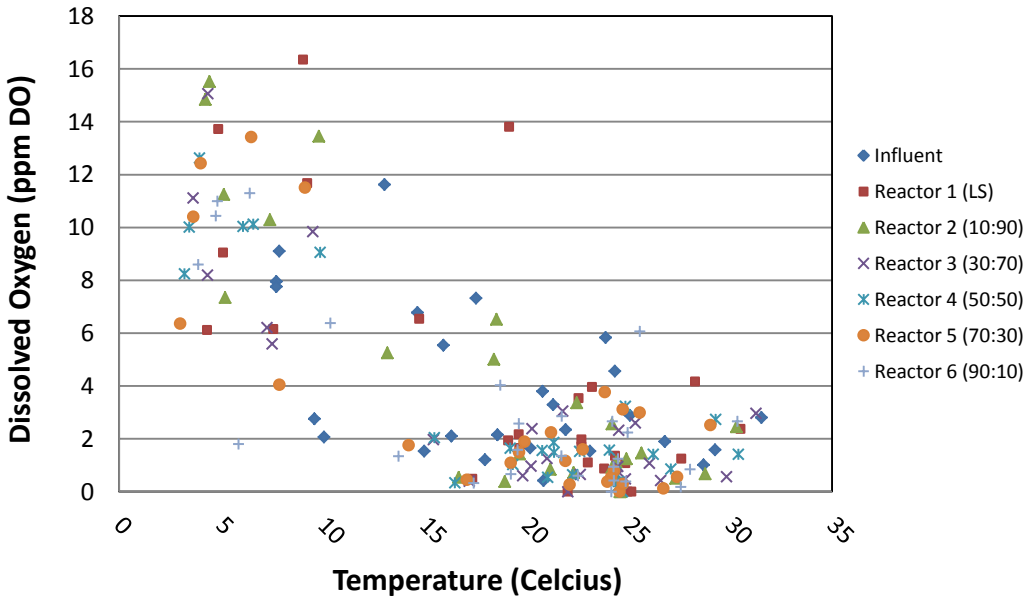

Figure 36: Plot displaying dissolved oxygen concentrations (ppm DO) versus the recorded field temperatures of the Influent AMD and the acid impoundments of each reactor.

Comparing the acid impoundment (AI) dissolved oxygen values to the measured temperature shows a negative correlation between the two parameters (Figure 36). Temperature has been long since known to play a large role in the solvation of gases such as $O_2(g)$ and an increase in dissolved oxygen with temperature decrease is expected (Manahan,

2010). Figure 36 also suggest there is little difference to dissolved oxygen values between the AMD influent, limestone reactor (R1) and biologic reactors (R2). Still as previously discussed, measurable decreases from influent DO in the AI's of all reactors persisted during the warmer biologically active months.

Therefore, acidophilic iron oxidizing *proteobacteria* such as *A. ferrooxidans* which comprised the majority of microbial communities found at the uppermost portion of each reactor may facilitate in using $O_{2(aq)}$ to induce the formation of iron oxides (Pugh, 2013; Wang et al., 2013b). Additionally superoxide and peroxyl radical generation by the photolysis of dissolved oxygen induced by solar radiation may also enhance oxygen consumption in the AI layer during warm temperature months (Garg et al., 2013).

Anoxic environments are associated with cultivating active sulfate-reducing bacteria populations and, therefore, are a key ingredient in the performance of bioreactor technology (Johnson and Hallberg, 2005). Although during initial week of the experiment bioreactor dissolved oxygen measurements taken from the effluent all registered near zero ppm DO, the environment did not maintain anoxia through the rest of the experiment. As the AMD passed though the cells simulated acid impoundment through the biologic media and hence to the effluent ports, a net consumption DO concentrations was observed (Figure 16). This observation paralleled a decrease in air temperature and also corresponded to an increase in dissolve iron, manganese, copper, nickel and zinc. The net consumption of oxygen from the acid impoundment to the effluent ports implies that oxidative processes had shifted deeper into all reactors during cold temperature months. As a result, processes such as oxidative-dissolution and decreases in precipitation kinetics would produce disturbances in these reactors influencing destabilization of both mineral phases and adsorbed species (Edwards et al., 2000). As documented by the high concentrations of sulfide and reducing ORP measurements, conditions were suitable to induce the formation of sulfide phases during the early months of operation. Such phases may have been subject to oxidative dissolution as outlined in the following equation (Neculita et al., 2007):

$$FeS_2(s) + 3.5O_2(aq) + H_2O(l) \rightarrow Fe^{2+} + 2H+(aq) + 2SO_4^{2-}(aq)$$

This would explain the net consumption of oxygen during this time and the notable increase in dissolved metals especially manganese and iron as they form relatively unstable phases (i.e. MnS (pK_{sp}=10.5-13.5), FeS (pK_{sp}=18.1), NiS (pK_{sp}=19.4-26.6), ZnS (pK_{sp}=24.7), CuS (pK_{sp}=36.1-48.5;Harris, 2010). Still, another mechanism must be included as the limestone reactor exhibited a similar decrease in dissolved oxygen yet not as pronounced of an increase in iron concentration as the bioreactors. During the colder months the same mechanism of iron oxidation occurring in the warm months would still occur yet with slower kinetics and thus would take place at a greater depth within the reactor. As previously mentioned the oxidation of ferrous iron into ferric iron and would induced a net consumption of dissolve oxygen from the acid impoundment to the effluent port via the following equation (Wang et al., 2013b):

$$4Fe^{2+} + O_2(aq) + 4H^+ \rightarrow 4Fe^{3+} + 2H_2O$$

Excessive release of protons via ferrous oxidation and the subsequent slow precipitation of additional oxide phases would cause a displacement of adsorbed cations (magnesium, zinc) on the oxo-bridges of previously formed iron oxyhydroxides through proton exchange (Kim et al., 2008; Lee et al., 2002). This would explain the release of zinc, manganese and copper in the limestone reactor (R1) during the colder months. Still in the biologic reactors (R2-R6), oxidative-

dissolution would remain the dominant causation for the decreases in metal attenuation as protons produced during ferrous oxidation would be less available for cation exchange on oxide surfaces due to the circum-neutral pH observed in these reactors during the colder months (hydrogen ions generated by ferrous oxidation are buffered by available alkalinity).

4.2 Effect of Changes in Redox Conditions on Bioreactor Efficiency

As shown earlier, dynamic changes in the redox environments within the bioreactors test cells (R2-R6) were measured throughout the course of this experiment, in contrast to the effluent ORP measurements of the limestone reactor followed trends similar to AMD influent. Aside from the low-temperature months, all bioreactor effluents exhibited a large reduction in ORP values throughout the experiment. To further describe the transitions in oxidation-reduction potential, changes in ORP values were calculated using measured ORP values from influent to acid impoundments and acid impoundments to effluent ports as a function of time (Figure 37 & 38). Thus positive ΔORP (mV) represents an oxidative transition while a negative ΔORP (mV) represents a reducing transition.

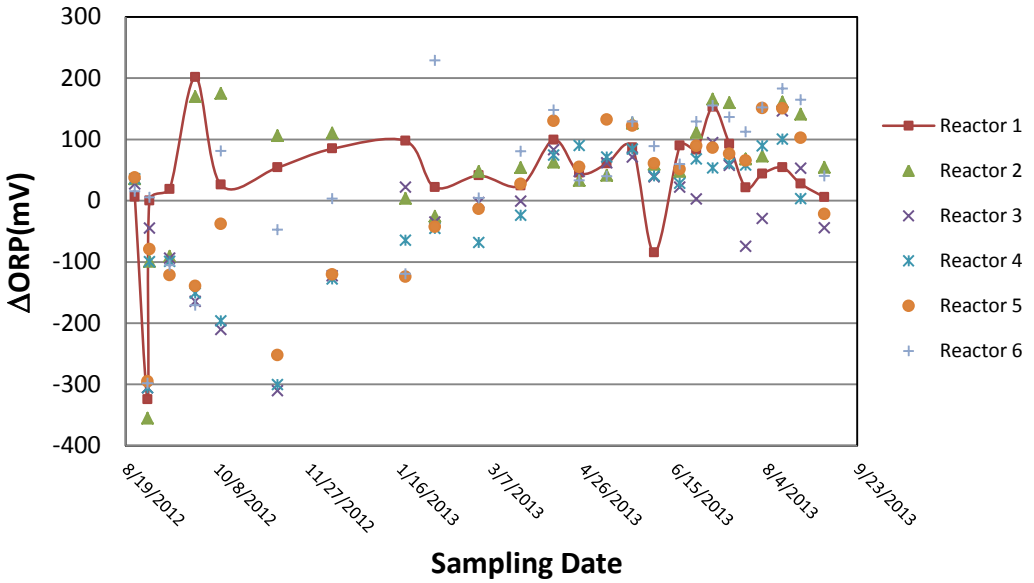

Figure 37: Calculated changes in ORP values (ΔORP) from the influent drainage to the acid impoundments of each reactor (R1-R6) during each sampling event.

Figure 37 displays an oxidative transition ΔORP > 0 in the acid impoundment of the limestone reactor (R1) throughout the majority of the experiment. Since the formation of iron oxyhydroxides (FeOOH) should be the prevalent reaction occurring within Reactor 1 this is suspected to be the main cause for increases in ORP values. Similar redox changes were shown to have direct correlation to oxidation of ferrous iron in mixed cultures of *A. ferrooxidans* (Wang et al., 2013b). Changes in ORP values from influent AMD to the simulated acid impoundment for each bioreactor test cells (R2-R6) represents a transition from reducing to moderately oxidizing as a function of time (Figure 37). This trend mimics the evolution of pH in the acid impoundments of the bioreactors (Figure 10) as they went from net pH increases to

net decreases as the experiment progressed. Substantial decreases in pH and increases in ORP values observed in the transition from the influent drainage to the simulated acid impoundment of each bioreactor suggest that the biologic populations in upper portion of these reactors became dominated by acidophilic iron-oxidizing bacteria during the late stages of the experiment. As it turns out, a comparison of the microbial communities sequenced in the upper portions of the bioreactors showed a strong increase in chemolithotrophs between August 2012 to May 2013 (Pugh, 2013).

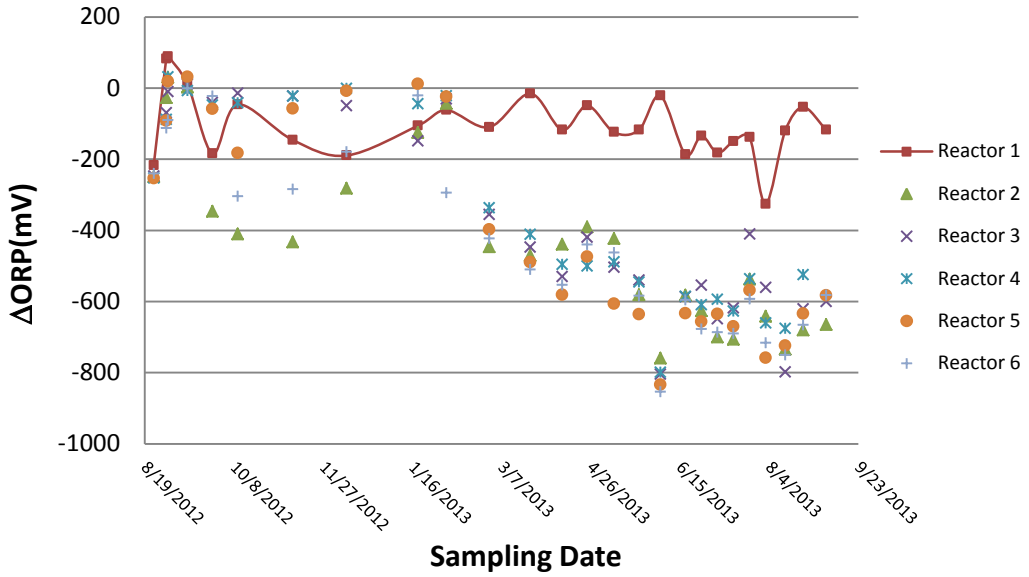

Figure 38: Calculated changes in ORP values (ΔORP) from the AI→Effluent of each reactor (R1-R6) during the experiment.

Although the effluent of the limestone reactor's (R-1) acid impoundment exhibited ORP positive ORP, averaging 211mV, a change to a reducing environment was recorded in the R-1 effluent throughout most of the the experiment (Figure 38). When the ferric iron underwent hydrolysis at the uppermost portion of the reactor the ratio of ferric to ferrous iron decreased creating a corresponding decrease in ORP (Hiroyoshi et al., 2001). Early on bioreactors displayed a change to reducing ORP conditions where the magnitude of ORP reduction was greater whenever the overlying acid impoundment was more oxidizing. During cold months the change to a more reducing environment decreased significantly at both the AI and Effluent in all bioreactors, coinciding with the suggested oxidative dissolution conditions. From late February 2013 to August 2013, a large change in ORP values developed within the biologic reactors (R2-R6) between the overlying simulated acid impoundment and effluent discharge at the bottom of the treatment media reaching a negative ORP (ΔORP's > 800mV). Such large reducing transitions commonly correspond to degradation of organic material introduced by highly active microbial communities while also providing an aqueous medium in which sulfate-reducing bacteria are facilitating SO_4^{2-} reduction (Neculita et al., 2008; Christensen et al., 1996; Muyzer and Stams, 2008; Behum et al., 2012). Isolated bacteria from sulfate-reducing

enrichments yielded populations more closely related to the *Desulfovibrio* genus suggesting that these communities were responsible for the sulfate reduction exhibited within each bioreactor (Pugh, 2013). However, reducing environments were not maintained throughout the low temperature months and thus the possibility of change back to an oxidative conditions were likely to re-occur at considerable depths within each bioreactor test cell as cold seasonal conditions persisted.

4.3 Biologic and Abiological Effects on pH Values

Measured pH values in the limestone reactor (R1) effluent displayed an average increase of 0.54 units from the influent AMD and remained net acidic throughout the experiment. Nevertheless, an overall average increase of 131 mg/L dissolved calcium from the AMD influent was produced within the limestone reactor suggesting that mineral precipitate formation on the limestone surfaces in R1 had not completely disrupted $CaCO_{3(s)}$ dissolution. In contrast to the limestone Reactor (R1) all bioreactors displayed a considerably higher release of calcium throughout the course of the experiment. Since all reactors (R1-R6) contained the same volumes of limestone the additional substrate included in biologic reactors generated more surface area for precipitate formation. Therefore, armoring of limestone by precipitates occurred rapidly within the limestone only reactor (R1) while the limestone within the bioreactors had slowly developed armoring and was able to continue relatively higher rates of calcite dissolution.

Substantial increase in pH within the biologic reactors (R2-R6) has been suggested to be induced by microbial reduction of strong sulfuric acid (pKa -3.0) into a relatively weak hydrogen sulfide (pKa ~ 7) via the following equation (Johnson and Hallberg, 2005):

$$SO_4^{2-}{}_{(aq)} + 2CH_2O + 2H^+{}_{(aq)} \rightarrow H_2S_{(aq)} + 2H_2CO_{3(aq)}$$

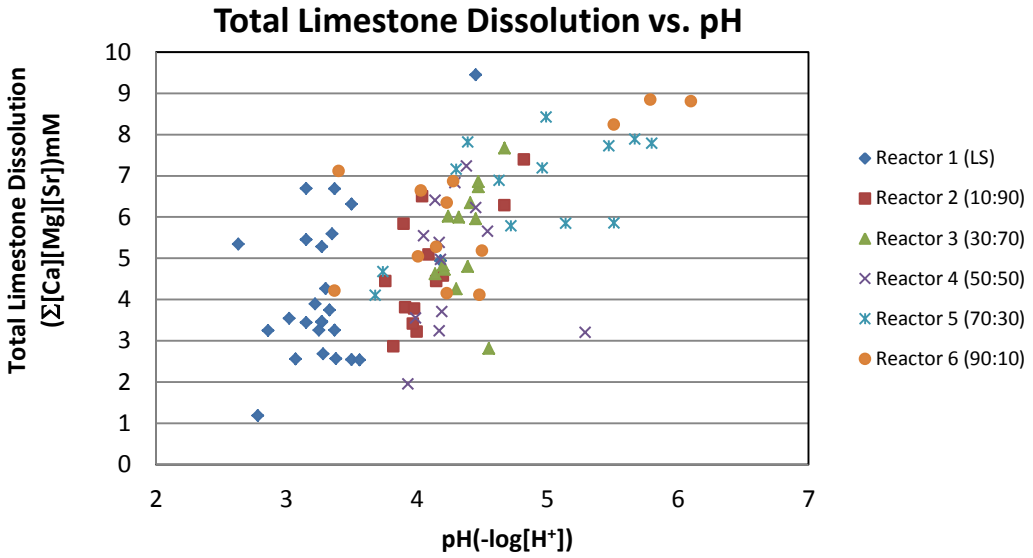

Figure 39 Plot of the summation of net increases in calcium, magnesium and strontium concentrations from influent AMD within each reactor compared to the measured pH. All bioreactor samples (R2-R6) contained high levels of dissolved sulfide while the limestone only reactor (R1) had no detectable sulfide.

To constrain whether hydrogen sulfide production within the bioreactors played a significant role in increasing effluent pH values, the net increase in dissolved calcium, strontium and magnesium were used as a proxy for total limestone dissolution at any given sampling event (Figure 39). Also, bioreactor (R2-R6) total limestone dissolution (TLD) values during later sampling events (i.e. 4/24/13 – 9/5/13) were compared to all TLD values of reactor 1 since 1) concentration of these constituents fell within a comparable range and 2) bioreactor samples all contained high dissolved sulfide concentrations during this time. The biologic reactors exhibit higher pH values during months of high sulfide concentrations when the total limestone dissolution values were comparable with reactor 1. This would be expected as hydrogen sulfide is a weaker acid relative to sulfuric and therefore the free proton concentration would decrease as sulfate is reduced to sulfide. Results from this experiment suggest that calcite dissolution plays a key role in promoting alkalinity and raising pH yet sulfide formation can also have a positive impact on neutralizing acidic solutions. To achieve metal removal hydrogen sulfide must be fully deprotonated.

4.4. pH-Dependent Aluminum Removal

Aluminum can be described as a redox insensitive element that exhibits mobility in solutions of extreme pH regardless of ORP conditions (Bigham and Nordstrom, 2000b). Figure 40 plots dissolved aluminum concentrations versus pH measurements analyzed from AMD influent and reactors 1-6. Minor increases in pH resulted in significant decreases of aluminum concentrations as pH = 4.0 corresponded to over 50% Al removal from influent AMD. Additional neutralization caused nearly 100% aluminum removal in the majority of samples as pH rose above 5.0 units. As mentioned earlier the mobility of aluminum is not particularly persuaded by changes in redox conditions and is demonstrated by the strong correlation with pH exhibited throughout the samples.

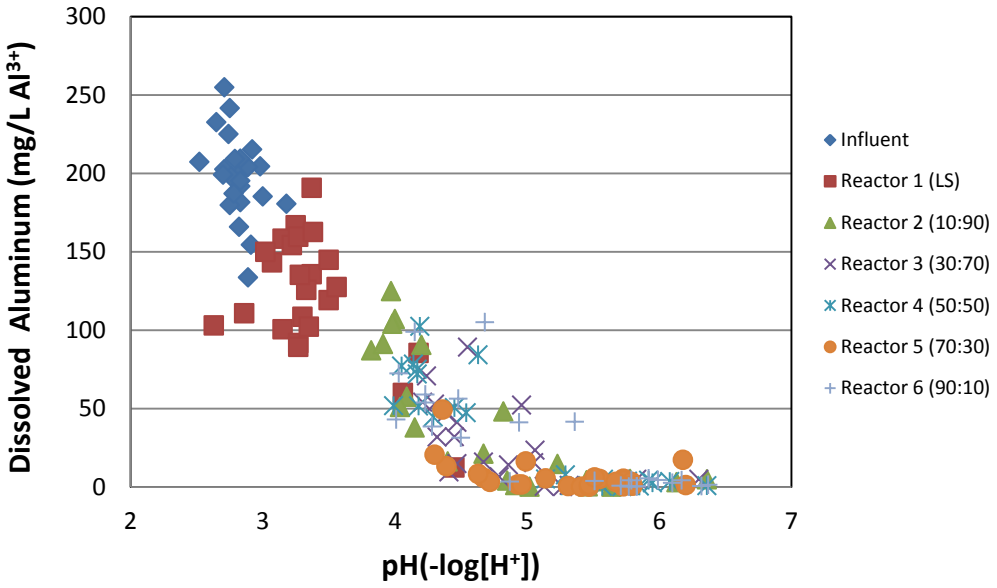

Figure 40: Plot of the dissolved aluminum concentration (mg/L Al^{3+}) against the corresponding pH measured during each sampling event.

4.5 Mechanisms for Sulfate Removal in Bioreactors

Bioreactor sulfate removal can be achieved via surface absorption, sulfate mineral co-precipitation and microbial-mediated reduction followed by sulfide precipitation (Guo and Blowes, 2009; Bigham and Nordstrom, 2000a; Rose and Ghazi, 1997). Thus to understand sulfate cycling within the reactors it is practical to first determine the major sulfate species that existed throughout the course of the experiment. Sulfuric acid (H_2SO_4) is a relatively strong diprotic acid and remains in solution as the bisulfate (HSO_4^-) anion at pH less than 2.0 units.

Increase in pH above 2.0 units cause the majority of sulfate species to become fully deprotonated to divalent anionic SO_4^{2-} species. Figure 41 displays speciation of sulfuric acid along with the minimum and maximum effluent pH values recorded within the limestone only reactor (i.e. blue rectangular area) and biologic reactors (pink rectangular area). Throughout the entire experiment all reactors contained the fully deprotonated SO_4^{2-} as the dominant species and thus can be used as a proxy to described sulfur cycling.

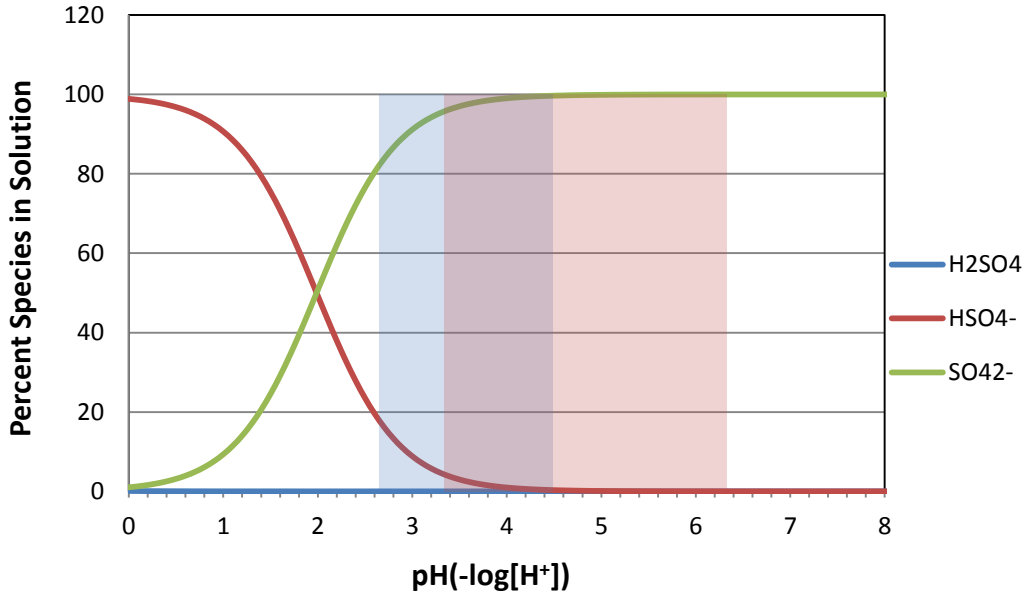

Figure 41: Plot displays the percent of sulfate species (i.e. H_2SO_4, HSO_4^- and SO_4^{2-}) as a function of pH. Free proton concentrations measured in the limestone only reactor (R1) and biologic reactors (R2-R6) are represented by the blue and pink rectangle, respectively.

It is expected that significant changes in dissolved iron would also influence sulfate concentrations as both ions exists as abundant constituents within the influent drainage. In fact Figure 42 displays that the percent iron removal and sulfate removal are positively correlated. By comparing removal percentages between the biologic reactors (R2-R6) and the limestone only reactor (R1), it can be stated that on average the bioreactors display higher sulfate removal as a function of iron removal. Geochemical modeling of effluent datasets of Reactor 1 (LS) describes the solution as being saturated (SI > 0) with respect to K-Jarosite ($KFe^{3+}{}_3(OH)_6(SO_4)_2$), nano-crystalline $Fe(OH)_3$, Cu/Zn-Ferrite ($Zn_{1-x}Cu_xFe_2O_4$) and Goethite ($FeO(OH)$). On average, a 0.22mg/L K^+ removal was documented in Reactor 1 through the

course of this experiment although it was sporadic and displayed many fluctuations including net potassium releases when compared to influent AMD. This suggests that K-Jarosite may very well be a sulfate mineral phase that is being formed within reactor 1 yet its stability may be compromised as it ages causing a structural rearrangement to a more stable iron oxide phase (Jolivet et al., 2004). Nano-crystalline ferrihydrite - $Fe(OH)_3$ is supersaturated with respect to Reactor 1 effluent and its formation involves the hydrolysis of ferric iron (Zhu et al., 2012). Ferrihydrite precipitation would explain the extremely low pH recorded at the upper most portion of the reactor, with the majority of values < 3, considering hydrolysis involves the net release of protons. Hydroxyl groups (-OH) of Nano crystalline ferrihydrite particles would provide tremendous surface area for hydrogen bonding to occur with negatively charged SO_4^{2-} species giving rise to sulfate removal via adsorption. However, ferrihydrite nano-particles may also exhibit meta-stability as growth of nucleation sites induces phase transformations and, thus, ferrihydrite may not account for the majority sulfate removal documented in the limestone only reactor (R1) (Zhu et al., 2012). Zinc and Copper ferrite may also account for iron oxide phases which form within reactor one as they exhibit super-saturation and have been removed at varying degrees throughout the experiment. Multiple oxo (Fe-O-Fe) bridges would be available on the surfaces of Zn/Cu-ferrite phases in which the four unbounded valence electrons of oxygen would attract protons in such low pH solutions giving the surface and overall net positive charge. In this case sulfate ions would also exhibit adsorption to these surfaces by electrostatic interactions. Lastly the effluent of reactor 1 was modeled as being saturated with respect to goethite (FeO(OH)) which is an extremely stable iron oxide phase that contains high surface area (Rietra et al., 1999). Having such high stability makes it likely that the metastable phases would have transformed via structural rearrangements or dissolution-recrystallization mechanisms resulting in the formation of goethite (Jolivet et al., 2004). Again the oxo (Fe-O-Fe) and hydroxyl (-OH) groups of this phase would offer sites for sulfate adsorption at the low pH measured in this reactor (Zhang and Sparks, 1990; Rietra et al., 1999).

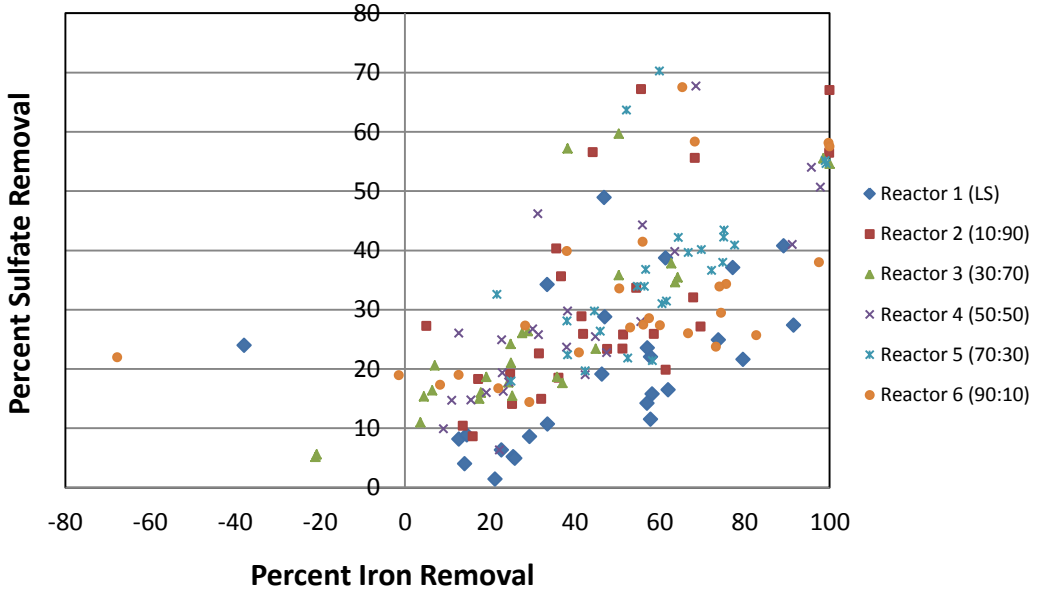

Figure 42: Plot of sulfate (y-axis) and iron (x-axis) removal percentages from influent AMD within each reactor (R1-R6).

Sulfide formation within bioreactors is often discernible by the appearance of black precipitates which can be readily separated from solution through vacuum filtration (Benner et al., 1999). Samples collected from biologic reactors were easily apparent in multiple causes as they contained dark black to grey solutions while the influent and limestone only reactor (R1) always contained clear to yellow-orange solutions (Figure 43). Dissolved sulfide concentrations measured during the experiment were associated with negative ORP measurements as depicted in Figure 44. In order to determine which sulfide minerals were liable to form during these experiments raw ORP values were converted to Eh units and pourbaix diagrams were created for multiple aqueous systems.

Figure 43: From left to right samples contain influent AMD, limestone only (R1) and bioreactor effluent (R2-R6).

Nordstrom et al. (2005) recognize that the standard half-cell potential of the Ag:AgCl electrode (i.e. HI769828-1) in 3.5M KCl reference solution as used in this experiment must be corrected for temperature induced fluctuations in reference potential. Therefore, to obtain Eh from ORP values which were measured in the field a linear equation was derived from variations in reference potential (E_{ref}) as a function of temperature (Figure 45). Next, the temperature dependent reference potential was corrected for each sample using measured field temperatures generating a reference potential (E_{ref}) for each data point. Electromotive force (*emf*) values determined in the field (i.e. ORP) were then added to their corresponding reference potential (E_{ref}) to determine the sample redox potential in Eh (Volts) units as outlined in the following equation (Nordstrom and Wilde, 2005):

$$Eh = emf + E_{ref}$$

Thus sulfide mineral formation could be further investigated by representing system parameters in pourbaix (i.e. Eh-pH) diagrams.

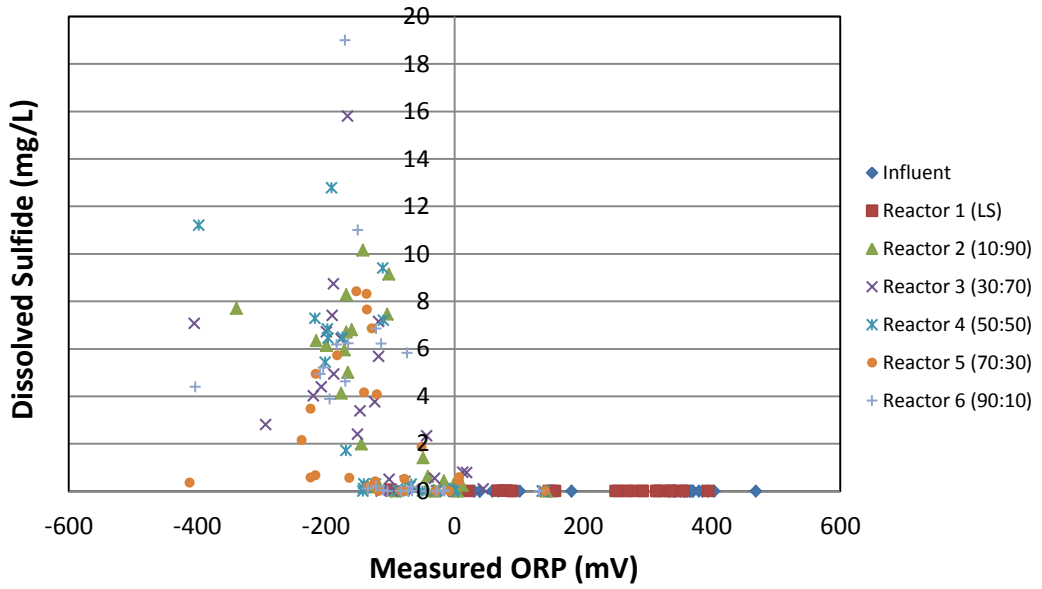

Figure 44 Measured sulfide concentrations (mg/L S^{2-}) and the corresponding ORP (mV) values recorded in the field.

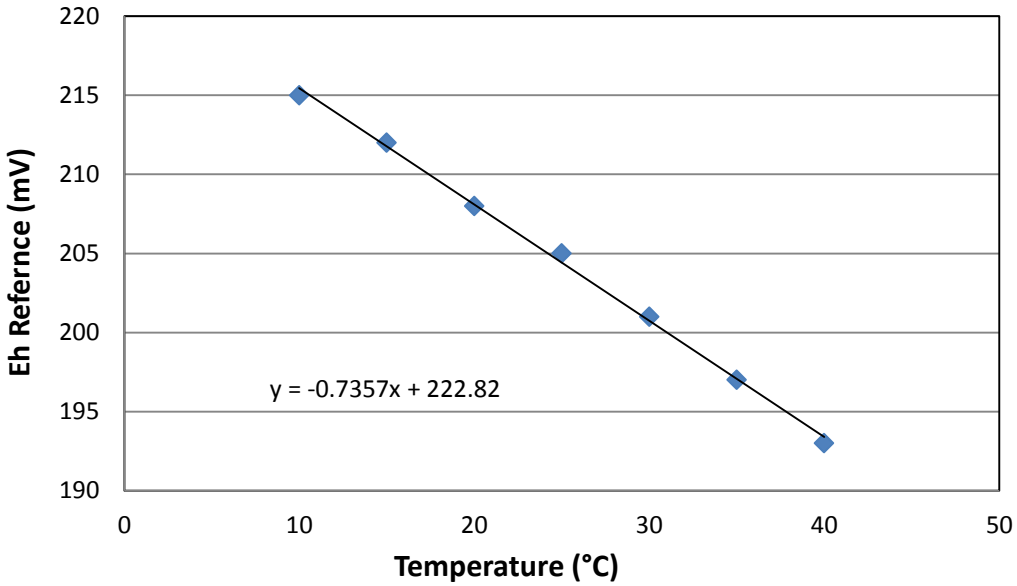

Figure 45 Linear regression of the temperature dependent Ag:AgCl reference values determined by Nordstrom and Wilde, 2005 were used to correct measured ORP values to field temperatures.

To define boundaries in each pourbaix diagram average species activities in AMD influent were used due to the relatively high ionic strength ($I_{average}$ = 0.0944) of these solutions. Two plots were formulated for each if these systems whereby one represented values taken

from the acid impoundment (AI) while the other characterizes effluent solutions collected from each reactor.

For the Fe-SO_4-H_2O system, reactor acid impoundments displayed a few values nearing pyrite formation but the bulk of the measurements suggested that dissolved ferrous and ferric iron were the dominant species (Figure 46). These results coincide with previous discussions on changes ion redox and pH within the acid impoundments of the bioreactors as they became more oxidizing and acidic with time. Additionally, over time the AI's on top of of each test reactor became dominated by members of *Acidimicrobiaceae*, *Alicyclobacillaceae* and *Acerobacteraceae* genera which all contain iron oxidizing microbes and, therefore, may have facilitated the oxidation of ferrous iron as documented by the increase in Eh (Pugh, 2013; Emerson et al., 2010).

In contrast Eh-pH measurements of the bioreactor (R2-R6) test cell effluent in a number of cases suggested pyrite formation was likely, whereas the limestone reactor (R1) remained effluent dominated by ferrous iron with a shift toward ferrihydrite formation over time (Figure 47). Nevertheless, pH increases in bioreactor test cell effluent suggest iron oxyhydroxide formation as an additional phase. These results imply that strong variations in pH and redox conditions within the bioreactors (R2-R6) which may have caused additional sulfate removal through both sulfide formation and iron oxide adsorption/co-precipitation as compared to the control (limestone reactor R-1 (LS)).

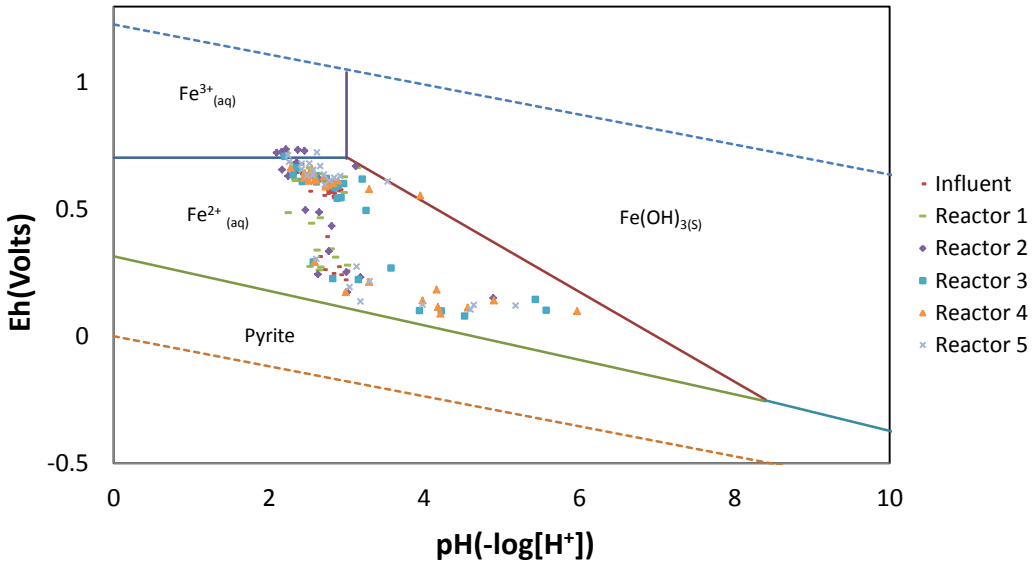

Figure 46: Plot of Eh-ph measurements made in the AMD influent and acid impoundments of each reactor (R1-R6) during the course of the experiment.

Dissolved manganese (Mn^{2+}) was a relatively stable species over a wide range of redox and pH values confirming it is a difficult element to remediation in mine drainage (Luan et al., 2012). High manganese solubility was suggested in our data-set as an average of only 0.14% and 0.58% was removed in the limestone (R1) and bioreactors (R2-R6), respectively. Eh-pH measurements of the test cell acid impoundments suggest that manganese mineralization would not be

expected (Figure 48). In contrast the test bioreactor cell measurements suggested that manganese precipitation as the mono-sulfide mineral alabandite was expected on a few occasions which may have accounted for the large amount of manganese removed during initial months of testing (Figure 51).

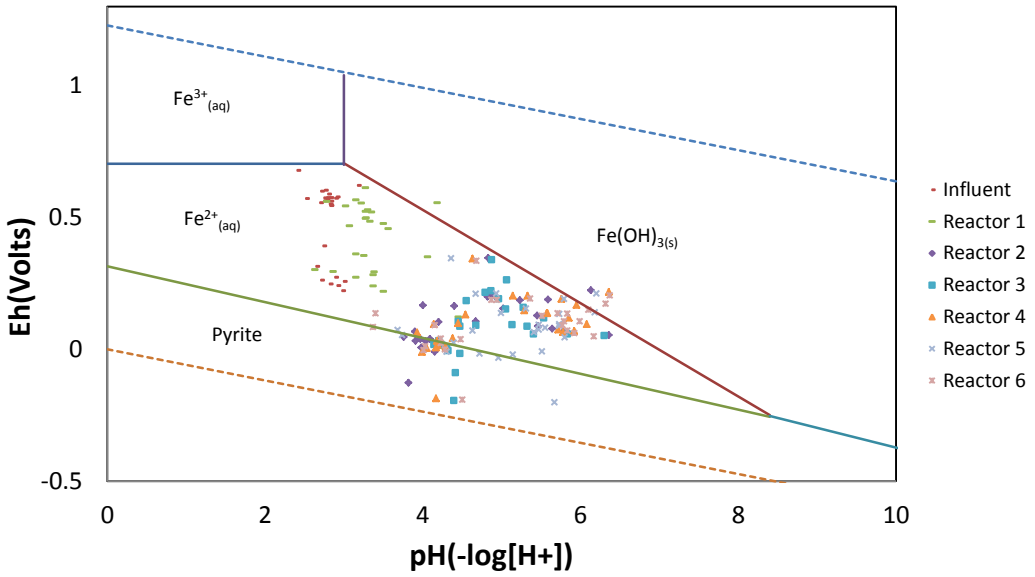

Figure 47 Plot of Eh-ph measurements made in the AMD influent and effluents of each reactor (R1-R6) during the course of the experiment.

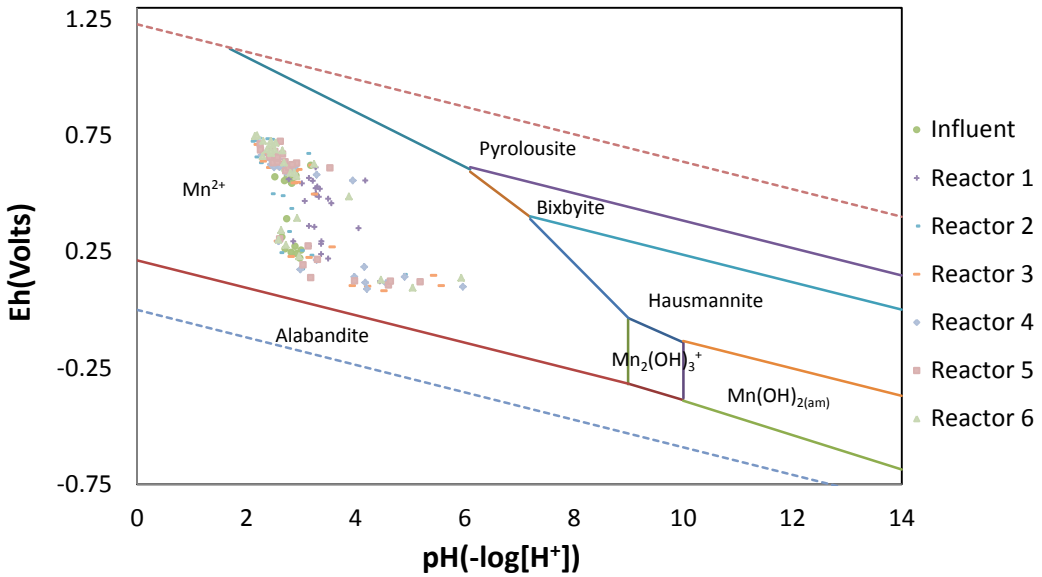

Figure 48: Plot of Eh(y-axis) versus pH(x-axis) for the AMD influent and acid impoundments of each reactor (R1-R6) collected during each sampling event.

More recent samples (last 6 months of testing) collected from bioreactor effluent showed a decrease in pH, but remained a reducing environment and, therefore, plotted near Mn^{2+}- Alabandite boundary (Figure 49). This late shift may have accounted for the 6% manganese removal documented in the herbaceous bioreactors (R5, R6) during this period. Overall the formation of manganese sulfides does not appear to play a significant role in the sulfate removal expressed by the biologic reactors (R2-R6).

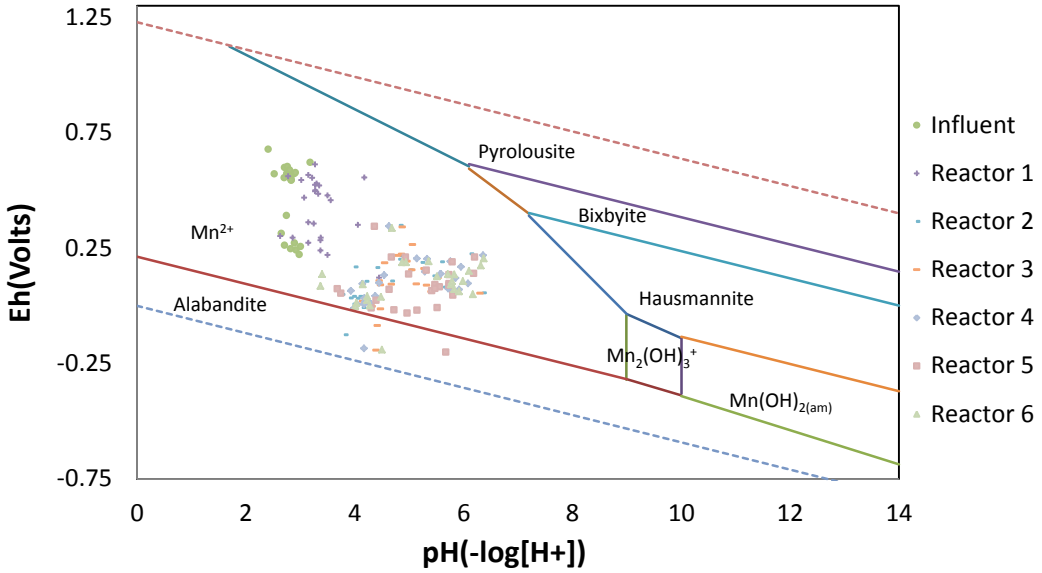

Figure 49: Plot of Eh (y-axis) versus pH (x-axis) for the AMD influent and reactor effluents (R1-R6) collected during each sampling event.

Zinc mobility in systems dominated by iron and sulfate can be extremely lowered at readily attainable pH and redox conditions. Iron oxide formation in the acid impoundments of each reactor had been shown to dominate as they evolved to highly oxidizing conditions. This condition however, does not increase the formation of Zn-rich ferrite as these phases are more likely to develop in solutions with pH > 3.12. Therefore, Figure 51 suggests that, zinc was not likely to be incorporated into iron oxide phases in the upper portions of the reactors. On the other hand increases in pH along with decreased redox conditions which were exhibited in the bioreactor (R2-R6) effluent favored formation of both Zn-Ferrite and sphalerite (ZnS; Figure 50).

These changes were expected as chemical data showed an average 86.7% Zn removal in Reactors 2-6 throughout the experiment. Supporting this finding, microbial communities collected from these test cells indicated the presence of SRB-species closely related to the family *Desulfobacteraceae* (Pugh, 2013), which have been shown to form sphalerite in communities cultured from biofilm's near Pb-Zn deposits (Labrenz, 2000).

A minimal shift from dissolved zinc to Zn-Ferrite was observed in the limestone only reactor (R1) and explains the low removal of 5.4% Zn^{2+} observed in water quality data during the course of the experiment. In summary, the formation of zinc sulfides could contribute to

decrease small portion of the sulfate removal in the bioreactor test cells but is not expected in the limestone-only reactor. The formation of Zn-Ferrite within the biologic reactors was observed and, therefore, may be an important mechanism for zinc sequestration within these systems.

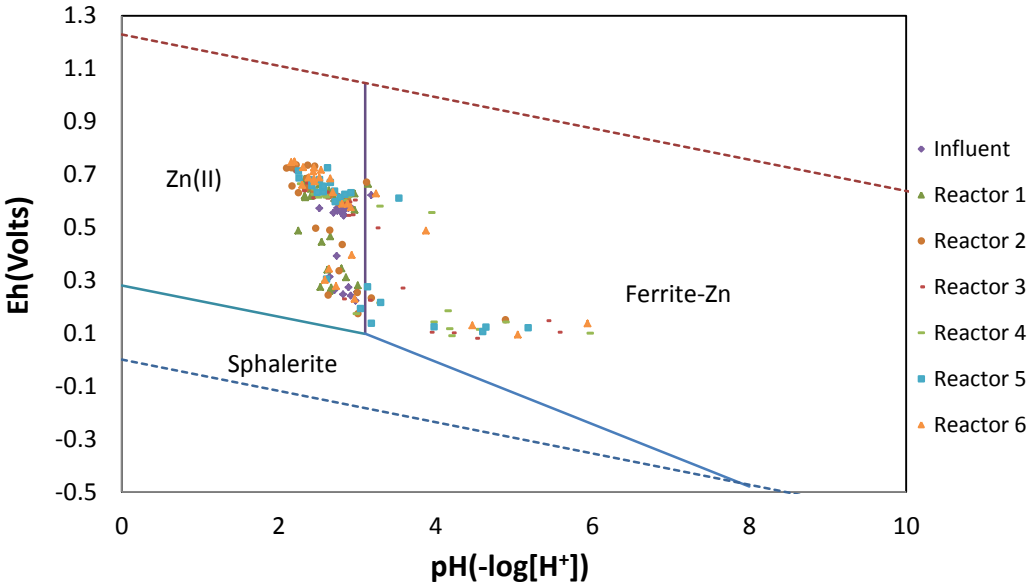

Figure 50: Plot of Eh (y-axis) and pH (x-axis) values measured in the AMD influent and acid impoundments of each reactor (R1-R6) throughout the course of this experiment.

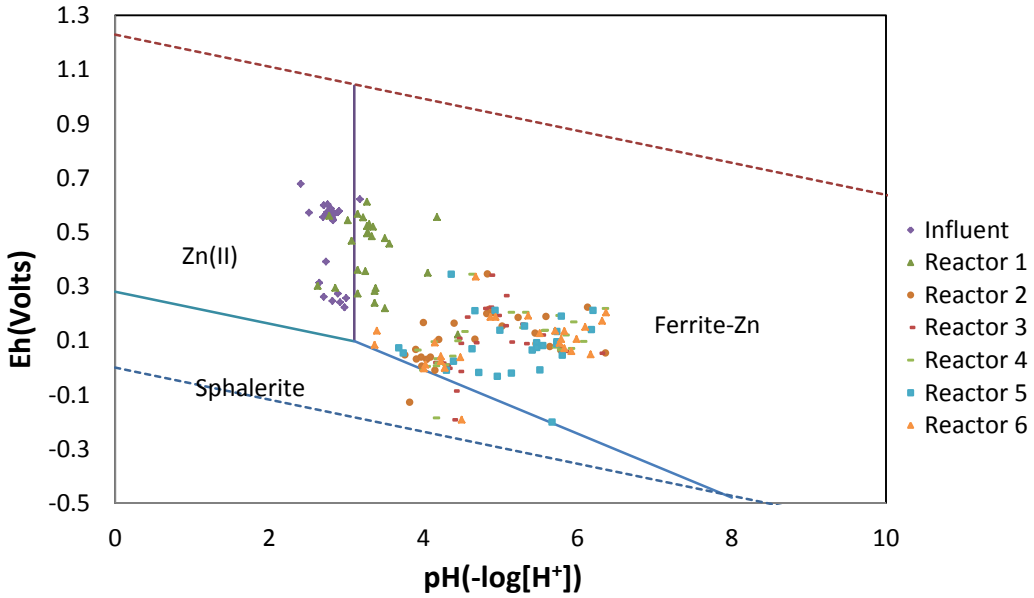

Figure 51: Plot of Eh (y-axis) and pH (x-axis) values measured in the AMD influent and effluents of each reactor (R1-R6) throughout the course of this experiment.

Within the Cu-Fe-SO_4-H_2O system copper can be removed via co-precipitation with iron oxides along with formation of various sulfide phases of which is most notably chalcopyrite ($CuFeS_2$).

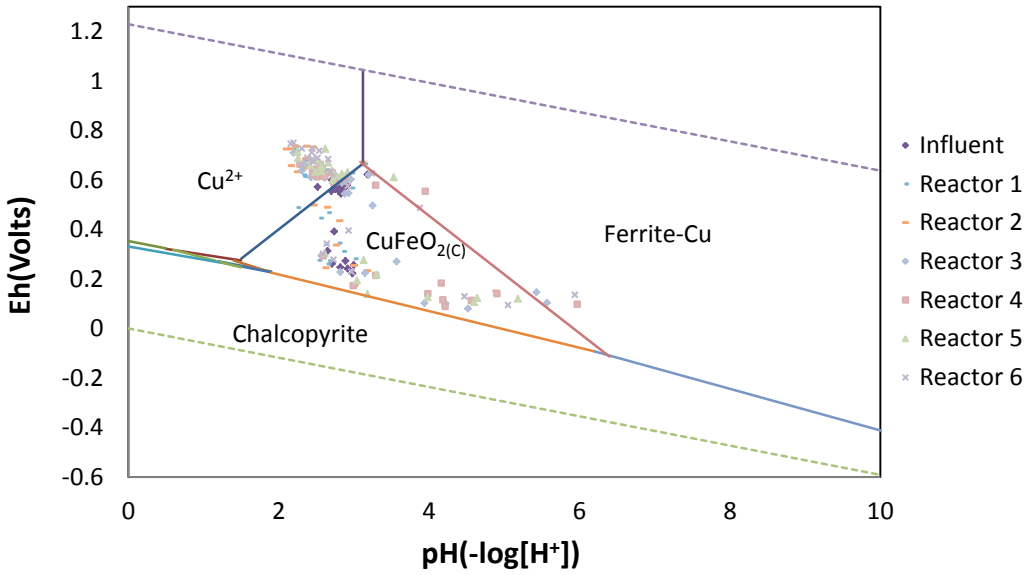

Figure 52 Plot of Eh-ph measurements made in the AMD influent and acid impoundments of each reactor (R1-R6) during the course of the experiment.

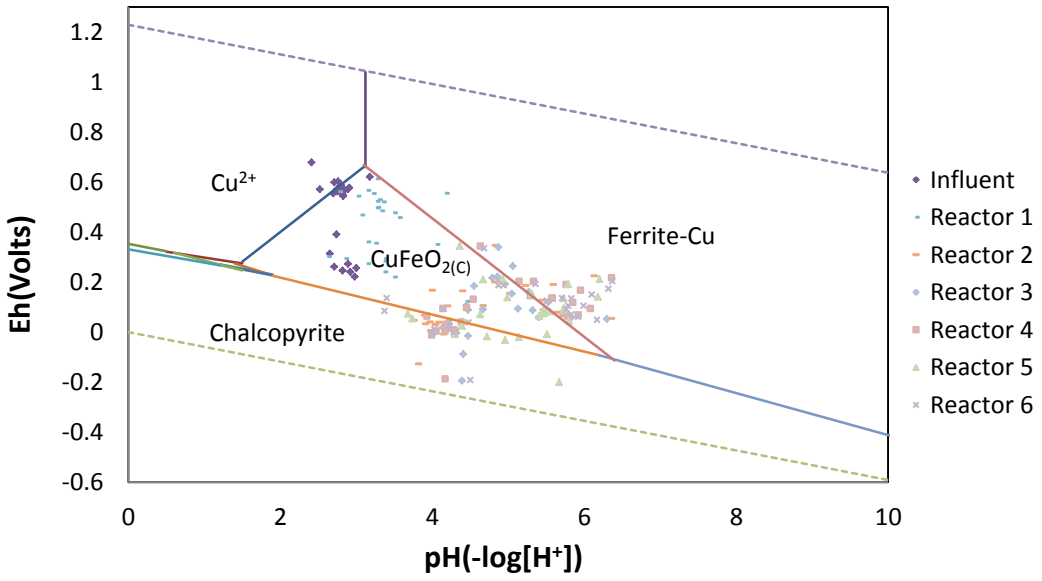

Figure 53 Plot of Eh-pH measurements made in the AMD influent and acid impoundments of each reactor (R1-R6) during the course of the experiment.

Under the Eh-pH conditions observed in a number of test cell acid impoundment samples, copper could have been precipitated as $CuFeO_2$ but also Cu-ferrite and even chalcopyrite (Figure 51). Recent AI measurements suggest that dissolved copper species were more favorable over mineral precipitate phases due to increases in both Eh potential and pH.

At depth, the test bioreactor cells had a more reducing environment and increased pH conditions which promoted the precipitation of all three Cu phases and lead to an average 81.4% copper removal documented by water quality measurements of the test bioreactors effluent (R2-R6; Figure 52 and 53). As for Reactor 1 (LS), the environmental conditions favored $CuFeO_2$ precipitation. On average Reactor 1 removed 53.8% copper from the AMD influent which would coincide with the shift toward the formation of copper co-precipitates with iron oxide. In summary, chalcopyrite was predicted within the bioreactor test cells (R2-R6) which could have accounted for a small portion of the increased in sulfate removal observed over the course of this experiment.

At pH values above 2.71 units nickel tends to become insoluble within the Ni-Fe-SO_4-H_2O system and can precipitate under all redox conditions within the stability limits of water. As previously noted the acidity of the acid impoundments of all reactors (R1-R6) increased over time and in many cases pH values dropped below that of the influent AMD (Figure 54). As a consequence the solubility of nickel within the test cell acid impoundments also would have increased with time and, therefore, most nickel removal would be expected deeper within the reactors. Eh-pH measurements of the limestone-only test cell (R1) effluent shift slightly toward $NiFeO_4$ stability indicating that any nickel removal occurring in R1 was likely to correspond to iron oxide formation (Figure 55).

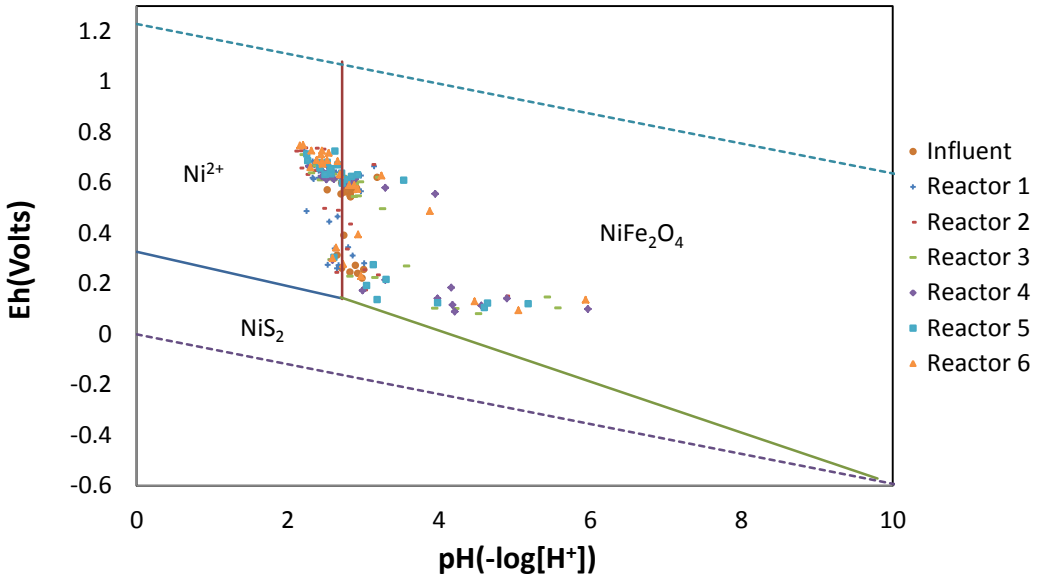

Figure 54 Measured Eh (y-axis) and Ph (x-axis) values in the AMD influent and acid impoundments of each reactor (R1-R6) throughout the course of this experiment.

Still, water quality test results show only minimal nickel removal from Reactor 1 along with a number of episodes with net nickel increases. In fact AMD influent nickel concentration data exhibited a high standard deviations which would be expected considering average

influent pH (median =2.80 units) which coincides with the Ni^{2+}- $NiFeO_4$ stability boundary (Figure 54).

Therefore, the overall nickel removal in Reactor 1 may be slightly underestimated due to the high degree of variability in influent nickel concentrations. Although results have indicated possible formation of nickel sulfide phases effluent measurements of the bioreactors (R2-R6) mainly suggest the environment was favorable for to $NiFeO_4$ precipitation. Still many samples fall along the border of both phases (NiS_2 & $NiFeO_4$) and, therefore, the formation of nickel sulfides should not be ruled out as a mineral phases that contribute to a small amount of the sulfate removal observed within the bioreactor test cells (R2-R6).

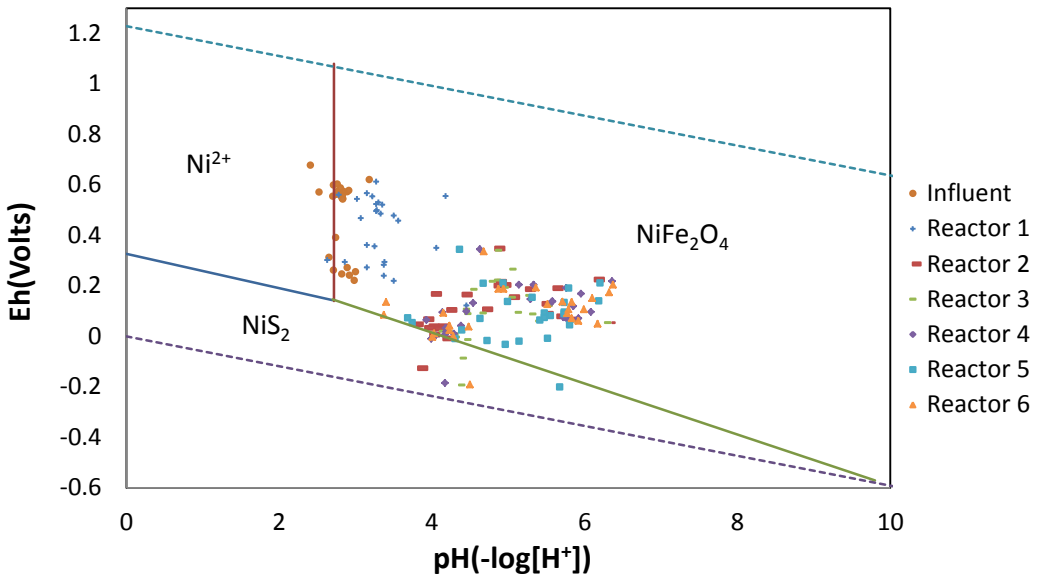

Figure 55 Measured Eh (y-axis) and pH (x-axis) values in the AMD influent and effluents of each reactor (R1-R6) throughout the course of this experiment.

As further evidence for the removal of trace metals through both iron oxide adsorption/co-precipitation and sulfide formation within the bioreactors (R2-R6) we plotted trace metal removal as a function of sulfide concentration. Figure 56 and 57 depicts both the nickel and zinc removal percentage against the sulfide concentration. In both charts high nickel and zinc removal was observed in bioreactor samples containing dissolved sulfide which ranged from 0-10mg/L S^{2-}. This suggests that these trace metals were removed by both mechanisms within the bioreactor test cells and accounted for the high removal percentages documented throughout the experiment.

In contrast, the limestone reactor (R1) did not 53yield sulfide levels of any significance and displayed low nickel and zinc removal indicating that by maintaining PH levels greater than average effluent values of R1 (i.e. PH > 3.34)within the bioreactor test cell media was important in removing zinc and nickel via iron oxyhydroxide adsorption/co-precipitation. Additionally, high zinc removal was expressed throughout a wide range of nickel removal percentages (i.e. 50-100%) although the pourbaix diagram for the Ni-Fe-SO_4-H_2O system describes nickel precipitation over a slightly broader range of pH-Eh conditions (Figure 58).

Hallberg et al. have shown that nickel laterites are extremely susceptible to reductive dissolution by subjecting them to reducing environments produced by cultures of *Acidithiobacillus ferrooxidans* (Hallberg et al., 2011). Therefore, nickel phases may be more susceptible to reductive-oxidative dissolution processes when subjected to the high variation in redox gradients observed within the bioreactors.

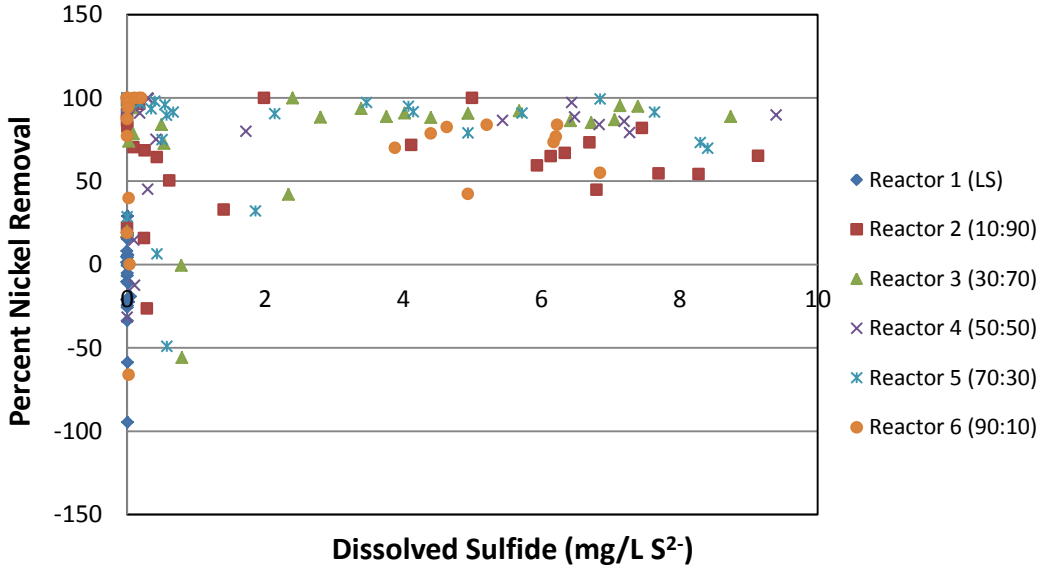

Figure 56 Plot displaying the percent nickel removal from influent AMD within all reactors (R1-R6) against dissolved sulfide concentrations (mg/L S^{2-}).

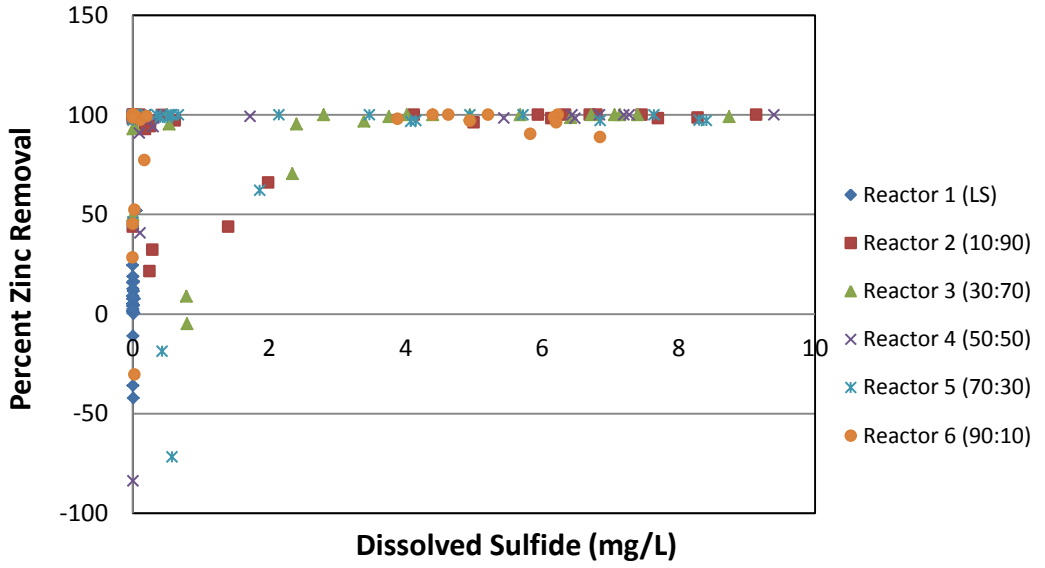

Figure 57 Plot displaying the percent zinc removal from influent AMD within all reactors (R1-R6) against dissolved sulfide concentrations (mg/L S^{2-}).

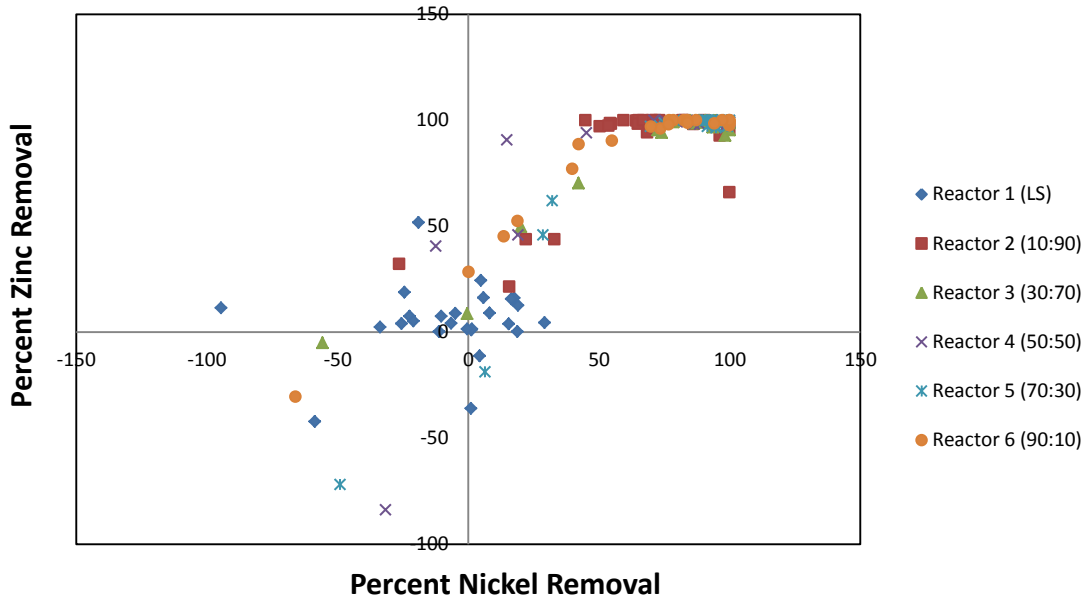

Figure 58 Plot displaying the percent zinc (y-axis) and nickel (x-axis) removal from the influent AMD to the effluent of each reactor (R1-R6) during the course of this experiment.

Reduction of sulfate and subsequent formation of sulfide phases within all bioreactor test cells (R2-R6) has been identified as a mechanism to achieve increased sulfate removal, a mechanism which was not observed in the limestone-only reactor (R1). Still, trace metal removal in the bioreactors (R2-R6) could have been increased by the co-precipitation with iron oxide and, therefore, the high sulfate removal observed in the water quality data may not be completely accounted for by sulfide precipitation. One additional mechanism for sulfide removal was by partitioning of aqueous hydrogen sulfide $H_2S_{(aq)}$ into the gaseous phase $H_2S_{(g)}$. Hydrogen sulfide is a weak acid (Pk_{a1} = 7.02) and, therefore, in an open system under acidic conditions (pH < 7) it has great potential to escape dissolution as a gaseous phase.

Although an anaerobic bioreactor column experiment conducted by Bernandez et al. (2012) displayed no evidence of H_2S volatilization and detected high concentrations of dissolved sulfide, the pH measured during this experiment was consistently reported above the pKa of H_2S (pH = 7.5). Therefore, a large amount of H_2S would have been in the monoprotic (HS^-) form. If this were the case then at the effluent pH values documented in the bioreactors (pH < 6.3) the release of hydrogen sulfide may account for a significant portion of the sulfate removal.

4.6 Fractionation of Sulfur Isotopes as Indication of Bacterial-Mediated Sulfate Reduction

The sulfur isotope values of dissolved sulfate precipitated from the effluent fluids of the bioreactors (R2-R6) during the warmer months were significantly enriched in ^{34}S compared to those of dissolved sulfate precipitated from the AMD influent. In contrast, small fractionations in sulfur isotopes were observed within the limestone-only reactor (R1) during the course of the experiment. This dismisses any abiotic contribution (e.g. adsorption/co-precipitation) as a major component influencing such large positive fractionations in the sulfur isotope

composition within effluent sulfate. Furthermore, in the biologic reactors (R2-R6) trends in sulfur isotope variations coincided with the trends measured for dissolved sulfide concentrations. Researchers have attributed microbial-mediated sulfate reduction to producing ^{34}S-depleted sulfide leaving the residual sulfate enriched in ^{34}S (Walters et al., 2013; Guo and Blowes, 2009; Burns et al., 2012). In the present study we find analogous responses in the isotopic composition of the effluent sulfate within bioreactor samples (R2-R6) during dates in which high sulfide concentrations were measured. However, during low-temperature months (T<10°) decreases in sulfur isotope enrichments as measured between AMD influent sulfate and bioreactor effluent (R2-R6) sulfate was documented. In addition, negative enrichment factors as those measured in Reactor 6 (90:10) in early February 2013 may be associated with the oxidative dissolution of previously formed ^{34}S-depleted sulfide mineral phases.

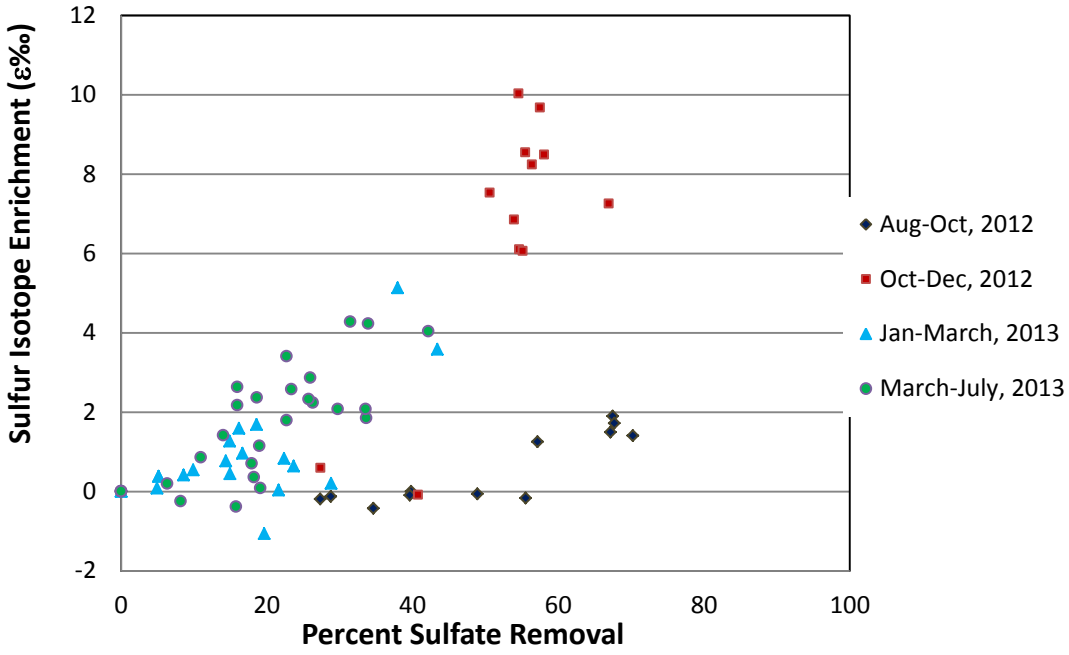

Figure 59 Measured sulfate removal percentages and the corresponding sulfur isotope composition of the dissolved sulfate precipitated from each sample through the course of this experiment. Data points are group by as Aug-Oct, 2012(Black Diamond); Oct-Dec, 2012(Red Square); Jan-March, 2013(Blue Triangle) and March-July, 2013(Green Circle) to show time dependent transitions.

Figure 59 reveals transitions in microbial-mediated sulfate reduction and their relation to the overall percent sulfate removal. Within the initial months (Aug-Oct, 2012) of operation ^{34}S-enrichment was low while sulfate removal percentages ranged from 27-70% removal. These results indicate that SRB communities were not yet fully established making abiotic mechanisms (i.e. adsorption/co-precipitation) the dominant pathway for sulfate removal. During the following months (Oct-Dec, 2012) percent sulfate removal within the biologic reactors (R2-R6) fell between 50-67% and a large ^{34}S-enrichment was measured in the effluent

sulfate. This implies that SRB communities had become well established and sulfate removal became dominated by reduction mechanisms. Subsequent months (Jan-March, 2013) corresponded to a low degree of biologic activity as the sulfur isotope composition of the effluent sulfate within the bioreactors dropped near that of the AMD influent. In the final months of which the sulfur isotope composition of the effluent sulfate was measured (March-July, 2013) increases in both sulfate removal and S^{34}-enrichment from influent AMD were recorded yet values were not as pronounced as was seen from Oct-Dec, 2012. Overall changes between the sulfur isotope compositions from the influent AMD to the effluent of all reactors (R1-R6) have shown time-dependent transitions in the biologically mediated sulfate reduction.

5. Conclusions

5.1 Bioreactor Performance based on Substrate Composition

To constrain whether substrate variations induced measureable differences in remediation efficacy, experimental results from all bioreactors (R2-R6) were group in the following three categories:

1) Dominantly Ligneous Reactors (R2, R3)
2) 50/50: Ligneous/Herbaceous Mixture (R4)
3) Dominantly Herbaceous Reactors (R5, R6)

Table 2 lists the calculated averages in pH values, percent removal of iron, sulfate, aluminum, manganese, nickel, zinc, copper and cadmium along with the alkalinity produced for each bioreactor category.

Table 2: Bioreactor Performance Based on Substrate Composition

Parameter	Ligneous (R2, R3)	50/50 Mix (R4)	Herbaceous (R5, R6)
PH	4.77	4.98	5.11
% Iron Removal	38.92	40.60	55.08
% Sulfate Removal	28.49	28.42	34.40
% Aluminum Removal	83.24	83.65	91.08
% Manganese Removal	0.24	-1.80	2.10
% Nickel Removal	69.55	73.81	73.81
% Zinc Removal	87.87	87.48	85.13
% Copper Removal	77.87	81.80	84.78
%Cadmium Removal	93.32	82.73	91.20
Alkalinity (meq as $CaCO_3$)	369.14	317.48	436.70
Overall Rank	2nd	3rd	1st

Parameters were then ranked as first (Blue Shading), second (Green Shading) and third (Red Shading) by comparing each bioreactor type against one another. Of the ten parameters the dominantly herbaceous reactors (R5, R6) ranked 1st in eight and thus were determined as top overall type in terms of remediation efficacy. As for the dominantly ligneous (R2, R3) and

50/50 mixture reactors, subtle variations in many parameters (i.e. sulfate, aluminum and zinc removal) made it difficult to distinguish a clear rank for both reactor types. Also, inter-comparison of these two reactor types depicts each type ranking higher than the other in 5 out of 10 parameters. Therefore, only due the fact that the dominantly ligneous reactors (R2, R3) ranked first in two categories while the 50/50 reactor only rank 1st in one category allowed the overall 2nd rank to be appropriated to the dominantly ligneous reactors (R2, R3).

6. Recommendations

Anaerobic sulfate reducing bioreactor (ASRB) field experiments have provided realistic physiochemical conditions that allow us to acknowledge different parameters that contribute to coal-derived AMD remediation. These conditions cannot be properly mimicked in a laboratory setting which cause significant discrepancies between lab-test and field scenarios. Most notably is the tremendous transition in redox environments from the upper to lower portions of the bioreactors (R2-R6). Previous lab experiments have not replicated this change as most experiments involved closed systems, static conditions and minimal exposure to light. Passive, anaerobic sulfate reducing bioreactors do not exists as closed systems, are exposed to the atmosphere and solar radiation on a day-to-day basis and must remain continuously flowing in order to maintain treat AMD discharges. Reactors used in these experiments had a relatively high total thickness 89 cm (35 in.) and developed redox transitions of up to 800 Mv but may not have provided enough redox "buffering" to prevent instability in redox sensitive phases through time. Therefore, to abate this issue it may be helpful to increase bioreactor depth and/or minimize the formation of acid impoundments on top of the bioreactor cell by lowering bioreactor pond levels to a thin layer over the compost interface.

Within the limestone-only reactor (R1), the increase in pH produced from the dissolution of limestone was ineffective for neutralization of AMD during short-term remediation modeled by our experiment. The coarse pebble- to cobble-sized limestone employed in the limestone-only test cell may not provide a large surface area for reactivity and, thus, the accumulation of precipitate coatings within this reactor may greatly inhibit abiotic alkalinity production. In contrast, biologic reactors have shown substantial increases in pH through time which could be attributed to: 1) additional compost surface area which created anoxic conditions and postponed the armoring of limestone surfaces, 2) degradation of organic material and subsequent formation of organic compounds containing functional groups of relatively weak acidity (i.e. R-COOH) and 3) depletion of free proton concentration by production of hydrogen sulfide. None the less it is apparent that addition of compost to limestone increases neutralization capacity and therefore it would be beneficial to add compost mixtures to limestone channel-ways that are used for AMD pre-treatment before entering bioreactor systems.

In this experiment, biologic sulfate reduction was shown to be effected by temperature (T), with SO_4^{2-} removal and sulfide concentrations exhibiting dramatic decreases at T < 10^{o}C. At these low temperatures, abiotic processes may become the dominant mechanism of sulfate sequestration. However, decrease in precipitate-induced sulfate absorption kinetics or precipitate phase transformation may result in the release of sequestered sulfate, iron, manganese, and other trace metals back into the solution during these low T periods.

Short-term results (9 months) indicate bioreactors dominated by woody substrate (R2 and R3) achieved the best sulfate removal percentages while displaying a high resistance to negative effects during low temperature months. However, recent results indicate the herbaceous reactors (R5 & R6) have maintained alkalinity and, thus, may be better suited to support sulfate-reducing bacterial communities in the future. Data collection of each reactor will continue in order to understand the effect of substrate composition on long-term reactor behavior to gain insight for designing optimal ASRB technology.

Acknowledgements
SIU graduate assistants, Evan R. Walters (Geology Department) and Charles Pugh (Microbiology Department) assisted with the construction of the field columns, field work, geological and microbial sample collections and analysis and data interpretation. Mr. Ron Kiser (ret.) of Illinois Dept. of Natural Resources, Office of Mines and Minerals and Mr. Paul Behum, OSMRE assisted in construction of the influent collection weir structure. We want to acknowledge the landowner support, Mr. and Mrs. Treg Brown of Carbondale, for granting access to the field site. The Illinois Department of Natural Resources (IDNR), and in particular Mr. Ron Kieser assisted our team with various tasks during the duration of this study. Lastly but not last, we want to acknowledge the Office of Surface Mining Reclamation and Enforcement, Mid-Continent Region, Alton, Illinois (OSMRE-MCR) for funding this research project. Mr. Paul Behum was the Technical Project Officer for this study.

REFERENCES

Affolter, B.R.H., Hatch, J. R. (2002) Characterization of the Quality of Coals from the Illinois Basin, Chapter E. *Resource Assessment of the Springfield, Herrin , Danville , and Baker Coals in the Illinois Basin*, (Hatch, J.R., Affolter, R.H., Eds., USGS Professional Paper 1625-D, E1-E222).

Amann, R., Fuchs, B. M. (2008) Single-cell identification in microbial communities by improved fluorescence in situ hybridization techniques. *Nature reviews. Microbiology*, *6*(5), 339–48.

American Public Health Association APHA., 2005. In: *Standard Methods for Examination of Water and Waste Water*. 21st edn. American Public Health Association, American Water Works Association and Water Pollution Control Federation, Washington, DC, 1268 pp.

Behum, P. T., Kiser, R., & Lewis, L. (2010) Investigation of the acid mine drainage at the Tab-Simco mine, Illinois: Observations and implications for remediation, Proceedings to the 27th Annual Meeting of the American Society of Mining and Reclamation, 12th Annual Pennsylvania Abandoned Mine Reclamation Conference and 4th Annual Appalachian Regional Reforestation Initiative Mined Land Reforestation Conference, 5–9.

Behum, P. T., Lefticariu, L., Bender, K. S., Segid, Y. T., Burns, A. S., & Pugh, C. W. (2011)

Remediation of coal-mine drainage by a sulfate-reducing bioreactor: A case study from the Illinois coal basin, USA. *Applied Geochemistry*, 26, S162–S166.

Behum, P. T., Lefticariu, L., Bender, K.S., Lewis, L., Segid, Y.T., Burns, A.S., Pugh, C.C., (2012) Passive treatment of coal-mine drainage by a sulfate-reducing bioreactor: A case study from the Illinois coal basin, USA. Proceedings of the 9th International Conference on Acid Rock Drainage, Ottawa, CAN.

Benner, S. G., Blowes, D. W., Gould, W. D., Herbert,, R. B., & Ptacek, C. J. (1999) Geochemistry of a permeable reactive barrier for metals and acid mine drainage. *Environmental Science & Technology*, *33*(16), 2793–2799.

Bernardez, L. a., de Andrade Lima, L. R. P., Ramos, C. L. S., & Almeida, P. F. (2012) A kinetic analysis of microbial sulfate reduction in an upflow packed-bed anaerobic bioreactor. *Mine Water and the Environment*, *31*(1), 62–68.

Bigham, J. M., & Nordstrom, D. K. (2000). Iron and aluminum hydroxysulfates from acid sulfate waters. *Reviews in Mineralogy and Geochemistry*, 40(1), 351–403.

Biomedicals, M. (2013) FastDNA ® SPIN Kit for Soil, 1–16.

Blowes, D. W., Spink, L. E., Wilkin, R. T., Jewett, D. G., & Weisener, C. J. (2009) Treatment of Arsenic , Heavy Metals , and Acidity Using a Mixed, *43*(6), 1970–1976.

Burns, A. S., Pugh, C. W., Segid, Y. T., Behum, P. T., Lefticariu, L., & Bender, K. S. (2012) Performance and microbial community dynamics of a sulfate-reducing bioreactor treating coal generated acid mine drainage. *Biodegradation*, 23(3), 415–429.

Christensen, B., Laake, M., & Lien, T. (1996) Treatment of acid mine water by sulfate-reducing bacteria; results from a bench scale experiment. *Water Research*, 30, 1617–1624.

Clyde, E. J., Champagne, P., & Jamieson, H. E. (2010) The use of passive treatment alternatives for the mitigation of acidic drainage at the Williams Brother mine, California: Bench-scale study. *Applied Geochemistry*, *25*(7), 958–971.

Cocos, I. a, Zagury, G. J., Clément, B., & Samson, R. (2002) Multiple factor design for reactive mixture selection for use in reactive walls in mine drainage treatment. *Water research*, *36*(1), 167–77.

Coggon, M., Becerra, C. A., Nüsslein, K., Miller, K., Yuretich, R., & Ergas, S. J. (2012) Bioavailability of jarosite for stimulating acid mine drainage attenuation. *Geochimica et Cosmochimica Acta*, *78*, 65–76.

Corperation, H.H.T. (2004) *Instruction Manual for Model Z-2000 Series Polarized Zeeman*

Atomic Absorption Spectrophotometer.

Daoud, J., Karamanev, D. (2006) Formation of jarosite during Fe^{2+} oxidation by Acidithiobacillus ferrooxidans. *Minerals Engineering*, *19*(9), 960–967.

DeNicol, D. M., & Stapleton, M. G. (2002) Impact of acid mine drainage on benthic communities in streams: the relative roles of substratum vs. aqueous effects. *Environmental pollution (Barking, Essex : 1987)*, *119*(3), 303–15.

Doulati Ardejani, F., Jodeiri Shokri, B., Bagheri, M., & Soleimani, E. (2010) Investigation of pyrite oxidation and acid mine drainage characterization associated with Razi active coal mine and coal washing waste dumps in the Azad shahr–Ramian region, northeast Iran. *Environmental Earth Sciences*, *61*(8), 1547–1560.

Edwards, K. J., Bond, P. L., Druschel, G. K., McGuire, M. M., Hamers, R. J., & Banfield, J. F. (2000) Geochemical and biological aspects of sulfide mineral dissolution: lessons from Iron Mountain, California. *Chemical Geology*, *169*(3-4), 383–397.

Emerson, D., Fleming, E. J., & McBeth, J. M. (2010) Iron-oxidizing bacteria: an environmental and genomic perspective. *Annual review of microbiology*, *64*, 561–83.

Freitas, A. P. P., Schneider, I. A. H., & Schwartzbold, A. (2011) Biosorption of heavy metals by algal communities in water streams affected by the acid mine drainage in the coal-mining region of Santa Catarina state, Brazil. *Minerals Engineering*, *24*(11), 1215–1218.

FWPCA. (2002). *Federal water pollution control act* (pp. 1–234).

Gammons, C. H., Duaime, T. E., Parker, S. R., Poulson, S. R., & Kennelly, P. (2010) Geochemistry and stable isotope investigation of acid mine drainage associated with abandoned coal mines in central Montana, USA. *Chemical Geology*, *269*(1-2), 100–112.

Garg, S., Jiang, C., Miller, C. J., Rose, A. L., & Waite, T. D. (2013) Iron redox transformations in continuously photolyzed acidic solutions containing natural organic matter: kinetic and mechanistic insights. *Environmental science & technology*, *47*(16), 9190–7.

Gibson, G. R. (1990) Physiology and ecology of the sulfate-reducing bacteria. *The Journal of Applied Bacteriology*, *69*(6), 769–97.

Gray, N. F. (1997). Environmental impact and remediation of acid mine drainage: a management problem, *Environmental Geology, 30,* 62-71.

Groat, C. G. (2004) National Field Manual for the Collection of Water-Quality Data. Chapter A3, Cleaning of Equipment for Water Sampling.

Guo, Q., & Blowes, D. W. (2009) Biogeochemistry of two types of permeable reactive barriers, organic carbon and iron-bearing organic carbon for mine drainage treatment: column experiments. *Journal of contaminant hydrology*, *107*(3-4), 128–39.

Hach Method 10244, H. M. (2011) Phenolphthalein and Total Alkalinity 10 to 4000 mg/L as $CaCO_3$, 1–8.

Hanajima, D., Fukumoto, Y., Yasuda, T., Suzuki, K., Maeda, K., & Morioka, R. (2011) Bacterial community dynamics in aerated cow manure slurry at different aeration intensities. *Journal of applied microbiology*, *111*(6), 1416–25.

Hanna. (2012) Instruction Manual HI 9828 (Multiparameter), www.hannainst.com

Harris, D. C. (2010) *Quantitative Chemical Analysis* (8th ed., p. AP10).

Hiroyoshi, N., Miki, H., Hirajimma, T., & Tsunekaw, M. (2001) Enhancement of Chalcopyrite leaching by ferrous ions in acidic ferric sulfate solutions. *Hydrometallurgy*, *60*(3), 185–187.

Hubbard, C. G., Black, S., & Coleman, M. L. (2009) Aqueous geochemistry and oxygen isotope compositions of acid mine drainage from the Río Tinto, SW Spain, highlight inconsistencies in current models. *Chemical Geology*, *265*(3-4), 321–334.

IDNR OSMRE. (2013). Illinois Abandoned Mine Land (AML) Reclamation Program. Retrieved from http://dnr.state.il.us/mines/aml/recpgm.htm

Johnson, D. B., & Hallberg, K. B. (2005). Acid mine drainage remediation options: a review. *The Science of the total environment*, *338*(1-2), 3–14.

Jolivet, J.-P., Chanéac, C., & Tronc, E. (2004) Iron oxide chemistry. From molecular clusters to extended solid networks. *Chemical communications (Cambridge, England)*, (5), 481–7.

Jong, T., & Parry, D. L. (2003) Removal of sulfate and heavy metals by sulfate reducing bacteria in short-term bench scale up flow anaerobic packed bed reactor runs. *Water research*, *37*(14), 3379–89.

Kadota, H., & Ishida, Y. (1972) Production of volatile sulfur compounds by microorganisms. *Annual review of microbiology*, (16), 127–138.

Kim, J., Nielsen, U. G., Grey, C. P. (2008) Local environments and Li adsorption on the lepidocrocite (gamma-FeOOH) and goethite (alpha-FeOOH): a ^{2}H and ^{7}Li solid-state NMR study. *Journal of the American Chemical Society*, *130*(4), 1285–95.

Korose, C. P., Elrick, S. D. (2010) Coal Geology of Illinois. *Keystone coal industry manual. Coal age, Jacksonville, Florida, Mining Media International*, 456–467.

Labrenz, M. (2000) Formation of sphalerite (ZnS) deposits in natural biofilms of sulfate-reducing bacteria. *Science*, *290*(5497), 1744–1747.

Lee, G., Bigham, J. M., & Faure, G. (2002) Removal of trace metals by coprecipitation with Fe, Al and Mn from natural waters contaminated with acid mine drainage in the Ducktown Mining District, Tennessee. *Applied Geochemistry*, *17*(5), 569–581.

Lee, S. H., Doherty, T. V, Linhardt, R. J., Dordick, J. S. (2009) Ionic liquid-mediated selective extraction of lignin from wood leading to enhanced enzymatic cellulose hydrolysis. *Biotechnology and bioengineering*, *102*(5), 1368–76.

Lefticariu, L., Pratt, L. M., Ripley, E. M. (2006) Mineralogic and sulfur isotopic effects accompanying oxidation of pyrite in millimolar solutions of hydrogen peroxide at temperatures from 4 to 150°C. *Geochimica et Cosmochimica Acta*, *70*(19), 4889–4905.

Lewis. L.L. (2008) Addressing acid mine drainage from complex conditions at the Tab Simco mine (Jackson County, Illinois), In: Proc. of the 30th annual National Association of Abandoned Mine Land Programs Conference, October 26-229, 2008, Durango, Colorado, 11 pp.

Lindsay, M. B. J., Blowes, D. W., Ptacek, C. J., & Condon, P. D. (2011) Transport and attenuation of metal(loid)s in mine tailings amended with organic carbon: Column experiments. *Journal of contaminant hydrology*, *125*(1-4), 26–38.

Luan, F., Santelli, C. M., Hansel, C. M., & Burgos, W. D. (2012) Defining manganese(II) removal processes in passive coal mine drainage treatment systems through laboratory incubation experiments. *Applied Geochemistry*, *27*(8), 1567–1578.

Manahan, S. E. (2010) Phase Interactions in Aquatic Chemistry. In *Evrironmental Chemistry, 9th ed.* (pp. 107–108).

McCauley, C., O'Sullivan, A.D., Milke, M.W., Weber, P., Trumm, D. (2009) Sulfate and metal removal in bioreactors treating acid mine drainage dominated with iron and aluminum. *Water research*, *43*(4), 961–970.

Muyzer, G., Stams, A.J.M. (2008) The ecology and biotechnology of sulphate-reducing bacteria. *Nature reviews. Microbiology*, *6*(6), 441–54.

Myers, M. D. (2006) *National Field Manual for the Collection of Water-Quality Data: Chaper A4, Collection of Water Samples*.

Ňancucheo, I., Hedrich, S., & Johnson, D. (2012) New microbiological strategies that enable the selective recovery and recycling of metals from acid mine drainage and mine process waters. *Mineralogical Magazine*, *76*(7), 2683–2692.

Neculita, C., Zagury, G. J., & Bussière, B. (2007) Passive treatment of acid mine drainage in bioreactors using sulfate-reducing bacteria: Critical review and research needs. *Journal of Environmental Quality, 36(1),* 1.

Neculita, C.-M., Zagury, G. J., & Bussière, B. (2008) Effectiveness of sulfate-reducing passive bioreactors for treating highly contaminated acid mine drainage: II. Metal removal mechanisms and potential mobility. *Applied Geochemistry*, *23*(12), 3545–3560.

Nieto, J. M., Sarmiento, A. M., Canovas, C. R., Olias, M., & Ayora, C. (2013) Acid mine drainage in the Iberian Pyrite Belt: 1. Hydrochemical characteristics and pollutant load of the Tinto and Odiel rivers. *Environmental Science and Pollution Research International*, 20, 7509-7519.
Nordstrom, D K, & Wilde, F. D. (2005) National Field Manual for the Collection of Water Quality Data (Vol. 2, pp. 1–22).

Nordstrom, Darrell Kirk, Alpers, C. N., Ptacek, C. J., & Blowes, D. W. (2000) Negative pH and extremely acidic mine waters from Iron Mountain, California. *Environmental Science & Technology*, *34*(2), 254–258.

Olías, M., Cánovas, C. R., Nieto, J. M., & Sarmiento, a. M. (2006) Evaluation of the dissolved contaminant load transported by the Tinto and Odiel rivers (South West Spain). *Applied Geochemistry*, *21*(10), 1733–1749.

Olías, M., Nieto, J. M., Sarmiento, a M., Cerón, J. C., & Cánovas, C. R. (2004) Seasonal water quality variations in a river affected by acid mine drainage: the Odiel River (South West Spain). *The Science of the Total Environment*, *333*(1-3), 267–281.

Oncel, M. S., Muhcu, a., Demirbas, E., & Kobya, M. (2013) A comparative study of chemical precipitation and electrocoagulation for treatment of coal acid drainage wastewater. *Journal of Environmental Chemical Engineering*, 1(4), 989–995.

Priha, O., Nyyssönen, M., Bomberg, M., Laitila, A., Simell, J., Kapanen, A., Juvonen, R. (2013) Application of denaturing high-performance liquid chromatography for monitoring sulfate-reducing bacteria in oil fields. *Applied and Environmental Microbiology*, *79*(17), 5186–5196.

Pugh, C. W. (2013) *Effect of Substrate Composition on Microbial Diversity and Efficiency of in situ Pilot-Scale Passive Sulfate Reducing Bioreactors Treating Acid Mine Drainage*. MS thesis. Southern Illinois University. http://opensiuc.lib.siu.edu/theses/1250/

Rietra, R., Hiemstra, T., & van Riemsdijk WH. (1999) Sulfate adsorption on goethite. *Journal of colloid and interface science*, *218*(2), 511–521.

Robinson-Lora, M. A., & Brennan, R. a. (2010) Chitin complex for the remediation of mine impacted water: Geochemistry of metal removal and comparison with other common substrates. *Applied Geochemistry*, *25*(3), 336–344.

Rose, S., Ghazi, M. (1997) Release of sulfate from iron oxyhydroxides precipitated from acid mine drainage associated with coal mining. *Environmental Science & Technology*, *31*(7), 2136–2140.

Rounds, R. S. A. (2012) *National field Manual for the Collection of Water Quality Data. Chapter 6.6, Alkalinity and Acid Neutralizing Capacity* (Vol. 9, pp. 1–45).

Scientific, T. F. (2012) Dionex AS-DV Autosampler Operator ' s Manual, (065259).

Shange, R. S., Ankumah, R. O., Ibekwe, A. M., Zabawa, R., & Dowd, S. E. (2012) Distinct soil bacterial communities revealed under a diversely managed agroecosystem. *PLoS ONE 7:e40338 10.1371/journal.pone.0040338.*

Smith, P. A. (2002) Characterization of and acid mine drainage sites in Southern Illinois. Proc. of the 2002 National meeting of the American Society of Mining and Reclamation, Lexington, Kentucky, June 9-13, 2002.

USEPA (2013) Sulfide Methylene Blue Method (Method 8131), 1–6.

USEPA (1978) Sulfate (Gravimetric) Method (Method 375.3), 1-8.

Vanholme, R., Demedts, B., Morreel, K., Ralph, J., & Boerjan, W. (2010) Lignin biosynthesis and structure. *Plant physiology*, *153*(3), 895–905.

Walters, E. R., Pugh, C. W., Bender, K. S., & Lefticariu, L. (2013) Use of sulfur isotopes to quantify biological and abiotic processes contributing to sulfur cycling in an AMD treatment system. *Mineralogical Magazine,* 77(5), 2443.

Wang, H., Gong, L., Cravotta, C. a, Yang, X., Tuovinen, O. H., Dong, H., & Fu, X. (2013) Inhibition of bacterial oxidation of ferrous iron by lead nitrate in sulfate-rich systems. *Journal of hazardous materials*, *244-245*, 718–25.

Zagury, G. J., Kulnieks, V. I., & Neculita, C. M. (2006). Characterization and reactivity assessment of organic substrates for sulphate-reducing bacteria in acid mine drainage treatment. Chemosphere, 64(6), 944-954.

Zagury, G. J., Neculita, C. M., & Bussiere, B. (2007). Passive Treatment of Acid Mine Drainage:Short Review, Applications, and Research Needs. Ottawa Geo(2007), 1439-1446.

Zhang, P.C., D.L. Sparks. (1990) Kinetics and mechanisms of sulfate adsorption/desorption on goethite using pressure-jump relaxation. *Soil Science Society of America Journal* 54.5, 1266-1273.

Zhu, M., Legg, B., Zhang, H., Gilbert, B., Ren, Y., Banfield, J. F., & Waychunas, G. (2012). Early stage formation of iron oxyhydroxides during neutralization of simulated acid mine drainage solutions. *Environmental science & technology*, *46*(15), 8140–7.